Measurement and Prediction of In-Cylinder Friction in Internal Combustion Engines

M.Gore

MEng DIS

A thesis submitted in partial fulfilment of the requirements for the

Degree of Doctor of Philosophy of Loughborough University

Wolfson School of Mechanical & Manufacturing Engineering

Loughborough University

Loughborough, UK

This dissertation is lovingly dedicated to my mother, Maria Gore. Her support, encouragement, and constant love have sustained me throughout my life.

Acknowledgments

I wish to whole-heartedly thank my supervisors, Prof. Homer Rahnejat and Mr Paul King for their guidance and support throughout this research.

The financial support from the Engineering and Physical Sciences Council (EPSRC) is acknowledged under the Encyclopaedic program grant.

Thanks are due to industrialists for their technical support and advice, in particular Prof. Brian Fitzsimons of Aston Martin, Dr. Sebastian Howell-Smith of Capricorn Automotive, Dr. Chris Warrens of BP-Castrol and in particular to Mr. Mike Theaker of Red Arch Engineering.

Thanks are also due to Dr. Miguel De la Cruz for technical aspects and help in running the slider rig and Dr. Ramin Rahmani for advice on numerical analysis.

I would also like to thank my friends and family especially Ashley Cairns for support and being tolerant during the hard times that a PhD brings.

Abstract

Currently, nearly 75% of worldwide transport is powered by internal combustion engines, with the worldwide transport sector accounting for 14% of the world's greenhouse gas emissions. With the current trend of downsizing and reducing vehicle cost, expensive solutions such as hybrids are often not viable. One solution is to reduce engine parasitic losses, thereby indirectly improving fuel efficiency, hence emissions. In terms of frictional losses, the piston-cylinder system accounts for 50% of all such losses, which altogether contribute to 20% of all engine losses.

The thesis describes an efficient analytical-numerical model in terms of computation times and CPU requirements. The model is a one dimensional analytical solution of Reynolds equation using Elrods cavitation algorithm. The model also includes determination of viscous friction as well as boundary/asperity friction based on the work of Greenwood and Tripp. Lubrication rheology is adjusted for generated hydrodynamic pressures and measured conjunctional temperature based on the cylinder liner. Model predictions are supported by a range of experimental work, from basic science measurements using an instrumented precision slider bearing rig for direct measurement of friction to the development and use of a floating liner on a motored and fired high speed, high performance internal combustion engine at the real situation practical level. The thesis highlights the development of the experimental rigs/engines as well application of state of the art instrumentation and data processing.

The combined numerical and experimental analysis show that a significant proportion of friction takes place at the top-dead-center reversal in the transition from the compression to the power stroke. Under motored conditions with low in-cylinder pressures this appears to follow Poiseuille friction, whereas under fired conditions with higher in-cylinder pressures causing increased compression ring sealing a mixed and/or boundary regime of lubrication is observed and predicted. Other than at the TDC reversal in both motored and fired conditions the frictional characteristics follow in direct proportion to the piston sliding velocity, therefore showing the dominance of viscous friction.

One outcome of the thesis is a validated analytical model which due to its computational efficiency can now be used in industry to provide timely predictions for the compression ring contact zone. Most significantly, the thesis has established an experimental procedure, infrastructure and data processing methods which enable the determination of the regime of lubrication and the underlying mechanisms of friction generation from basic science sliding surfaces to *in situ* direct measurements from a fired engine at high loads and sliding speeds.

Keywords: Internal Combustion Engine, Compression Ring, Transient Regime of Lubrication, Direct Measurement of In-Cylinder Friction, Floating Liner Principle.

Table of Contents

Dedication i

Acknowledgments ii

Abstract iii

Table of Contents iv

List of Tables and Figures viii

Nomenclature xii

Glossary of Terms xvii

Chapter 1: Introduction 1

1.1 Preamble 1

1.2 Background 8

1.3 Aims and Objectives 15

1.3.1 Specific Objectives 15

1.4- Structure of the Thesis 16

Chapter 2: Literature Review 18

2.1 Introduction 18

2.2 A Brief Historical Review of Tribology 19

2.3 Piston Ring Lubrication: Predictive Methods 27

2.3.1 Analytical Technique 28

2.3.2 Numerical Solutions 30

2.4 Experimental Investigations ..... …33

2.4.1 Test Rig Based Friction Measurement 33

2.4.2 Motored Engine Friction Measurement 35

2.4.3 Fired Engine Friction Measurement 38
2.4.3.1 The IMEP (Indicated Mean Effective Pressure) Technique 38
2.4.3.2 The Movable Bore Technique 39
2.5 Conclusion 46
Chapter 3: Experimental Set Up 47
3.1 Introduction 47
3.2 Parametric Measurement 48
3.3 The Sliding Test Rig 48
3.4 Test Engine Selection 54
3.5 Modified Components 58
3.6 Engine Test-Bed Set Up 60
3.7 Standard Instrumentation 66
3.7.1 Fuel Monitoring 66
3.7.2 Air 68
3.7.3 Water 69
3.7.4 Measurement of Air-Fuel-Ratio (ARF) 69
3.7.5 Measurement of Cylinder Pressure 70
3.7.6 Measurement of Engine (crank) Position 70
3.7.7 Throttle Position 71
3.7.8 Engine Speed Monitoring 71
3.7.9 Torque Measurement 71
3.7.10 System Repeatability 72

Chapter 4: Development of Floating Liner for Direct Measurement of Friction 74
4.1 Introduction 74
4.2 Measurement of Friction 74
4.2.1 Principles of Operation and Mechanical Design of the Floating Liner 75
4.2.2 Load Cells and Signal Processing System 81
4.3 The Calibration Procedure 82
4.4- Closure 85
Chapter 5: Determination of Surface Topography and Wear 86
5.1 Introduction 86
5.2 Brief Introduction to Statistical Topographical Measures 87
5.3 Wear Characteristics of Cross-Hatch Honed Liners 92
5.4 Closure 100
Chapter 6: Experimental Procedure and Results 102
6.1 Introduction 102
6.2 Controlled Parameters 103
6.3 Operational Performance of the Floating Liner 105
6.4 Monitoring of Piston Friction Under Motorised Running Condition 108
6.5 Monitoring of Piston Friction Under Engine Fired Conditions 114
Chapter 7: Numerical Modelling and Predictions 119
7.1 Introduction 119
7.2 One Dimensional Long Line Contact Solution 120
7.3 Long Line Contact Solution with Cavitation 124

7.3.1 Region of Full Film: $a \leq x \leq c$ 126

7.3.2 The Film Reformation Region $r \leq x \leq b$ 127

7.3.3 The Cavitation Region $c \leq x \leq r$ 129

7.4 Lubricant Rheology 131

7.5 Contact Load and Friction 132

7.5 Solution Method 135

7.6 Comparison of Predictions with Slider Rig Tests 137

7.7 Comparison with Engine Test Results Using the Floating Liner 155

7.8 Closure 161

Chapter 8: Conclusion and Suggested Further Work 162

8.1 Overall Conclusions 162

8.2 Achievement Of Specific Objectives 164

8.4 Suggested Further Work 168

References 170

List of Tables and Figures

Fig 1.1: Global transport CO2 emissions in 2000. WBCSD(2004) **King (2007)**…… 1
Fig 1.2: Proportion of energy and losses in an IC engine (Richardson, 2000)..... 4
Fig 1.3: A typical piston assembly…….. 8
Fig 1.4: A typical Stribeck diagram……..…11
Fig 2.1: Ring and liner tester, simulating real engine conditions (Akalin, 1998)…….. 33
Fig 2.2: Truhan's simple ring and liner test apparatus (**Truhan, 2005**)…… 35
Fig 2.3: Perfected floating liner equipment (**Livengood and Wallour,(1947**..... 43
Fig 2.4: Furuhama's perfected floating liner arrangement used by **Yoshida (1990)**……45
Fig 3.1: Slider rig with floating plate arrangement……...51
Fig 3.2: Fully developed slider rig…….....51
Fig 3.3: Detail view of "flat ring" in contact with "flat liner"……..... 52
Fig 3.5: Alicona measurements of flat piston ring (not-run)…… 52
Fig 3.6: Alicona measurements of flat cylinder liner (not-run)……..... 53
Fig 3.7: Cutaway of CRF450R engine (**Honda Motor Co. (2002)**)……..... 56
Fig 3.8: Honda CRF450R with cover removed……..... 57
Fig 3.9: Original Honda CRF450R OEM cylinder block……..... 58
Fig 3.10: New wet liner and liner carrier block……..... 59
Fig 3.11: New wet liner and liner carrier block……..... 59
Fig 3.12: Engine stand……..... 60
Fig 3.13: The engine test-bed……..…….....61
Fig 3.14: Original Honda sprocket attached to custom made flange……..... 61
Fig 3.15: Coupling arrangement to the dynamometer..... 62
Fig 3.16: Engine coolant circuit diagram.....63
Fig 3.17: Exhaust and extraction system.....64
Fig 3.18: The fuel system.....65
Fig 3.19: Palletised fuel system..... 67

Fig 3.20: Fuel temperature measurement.....68
Fig 3.21: Intake air temperature measurement location..... 69
Fig 3.22: Intake air temperature measurement location..... 69
Fig 3.23: Custom encoder mounted to the side of engine..... 70
Fig 3.24: Shenk throttle control system (Part of the Ricardo S3000 system).....71
Fig 3.25: Power curve repeatability.....73
Fig 4.1: A floating liner fitted into its block holder (housing) inserted into The engine block.....76
Fig 4.2: Cross-sectional view of the floating liner arrangement..... 76
Fig 4.3: The sealing arrangement at the top of the floating liner.....77
Fig 4.4: Kistler 9131B Force transducer specification **(Kistler AG)**.....79
Fig 4.5: Floating liner sensor arrangement..... 79
Fig 4.6: Modal analysis of floating liner.....80
Fig 4.7: Components used in the data acquisition system.....82
Fig 4.8: Calibration of floating liner and charge amplifier set-up.....83
Fig 4.9: Stage-two calibration..... 83
Fig 4.10: Radial calibration..... 84
Fig 4.11: Forward Vs Reverse calibration.....85
Fig 5.1: The principle of operation for contact measurement devices..... 89
Fig 5.2: Average surface roughness, R_a..... 89
Fig 5.3: Two distinct surfaces with same value of R_a..... 90
Fig 5.4: Determination of surface parameters R_k, R_{pk} and R_{vk}..... 91
Fig 5.5: Definition of plateau surface parameters..... 92
Fig 5.6: The engine testing procedure for liner wear study.....93
Fig 5.7: Regions of measurement of liner surface topography 96
Fig 5.8: PGI 1250 Aspheric mould measurement system with cylinder liner insert and the measuring stylus.....97
Fig 5.9: PGI 1250 Aspheric mould measurement system with cylinder liner insert and the measuring stylus..... 97
Fig 5.10: Changes in surface “peakiness” parameter R_{pk} during the

running-in wear phase..... 98
Fig 5.11: The unaffected R_{vk} parameter through severe accelerated wear in a fired engine..... 99
Fig 5.12: Gradual wear phase noted by the R_k value.....100
Fig 6.1: Floating liner with cylinder head off.....106
Fig 6.2: Measured friction with cylinder head removed.....107
Fig 6.3: Chamber pressure under motorised condition at 2500 rpm.....111
Fig 6.4: Measured friction under motored condition.....113
Fig 6.5: Measured friction under fired engine condition at 2500 rpm, torque of 30Nm..... 115
Fig 6.6: Measured friction under fired engine condition at 2500 rpm, torque of 72 Nm..... 116
Fig 6.7: Measured friction under fired engine condition at 4000 rpm, torque of 70 Nm..... 117
Fig 7.1: Lubricant film variation within the contact domain..... 125
Fig 7.2: Determining the real contact width, l_c 139
Fig 7.3: Variations of statistical function $F_{5/2}$ with Stribeck film ratio, λ..... 140
Fig 7.4: Variations of statistical function F_2 with Stribeck film ratio, λ..... 143
Fig 7.5: The measured sliding speed of the slider..... 147
Fig 7.6: Measured friction of the slider rig contact for the Ni-SiC coated plate..... 148
Fig 7.7: Measured coefficient of friction for the steel ring strip sliding against the floating plate coated with Ni-SiC..... 149
Fig 7.8: Minimum film thickness variation for uncoated and coated ring strip- plate contact during the prescribed sliding motion.....151
Fig 7.9: Regime of lubrication for the cases studied with the slider rig.....152
Fig 7.10: Predicted hydrodynamic reaction.....153
Fig 7.11: Load share of asperities (boundary interaction).....153
Fig 7.12: Coefficient of friction variation.....155
Fig 7.13: Cylinder chamber pressure for motored engine at 3000 rpm..... 157
Fig 7.14: Comparison of measured and predicted ring-liner friction..... 160

Table of Tables

Table 1.1: Projection of car ownership per 1000 people. Goldman Sachs "The BRICs and Global Markets; Crude, Cars and Capital, Goldman Sachs Global Economics Paper No. 118, 2004. **King (2008)**……....2

Table 1.2: New engine and transmission efficiency savings, and indicative production costs. **King (2007)**……..…….....3

Table 1.3: Sources of Savings with improved tribology **Jost (1966)**…… 6

Table 3.1: Slider Rig Parameters..... 53

Table 3.2 Engine characteristics of Honda CRF45 (**Honda Motor Co., 2002**)……..... 56

Table 4.1: Modal analysis tabulated results..... 81

Table 5.1: Engine test condition corresponding to figure 5.6..... 94

Table 6.1: Control parameters..... 103

Table 6.2: Test conditions: motorised and fired with different engine loading..... 110

Table 7.1: Input data for the two studied cases..... 145

Table 7.2: List of engine specification and analysis data.....158

Nomenclature

A	Piston ring / cylinder liner contact area
A_a	Total contact area at the tip of asperities of two opposing surfaces
a	Acceleration due to gravity
a, b	Front and rear coordinates of piston ring / cylinder liner contact
a_l	Acceleration of floating liner
a_p	Acceleration of the piston
b	Labyrinth seal width
$C_1, \dots C_4$	Integration constants
c	Cavitation (film rupture) point
d	Ring thickness
E	Modulus of elasticity
E'	Composite elasticity modulus
EI	Piston ring flexural rigidity
F	Total force applied on the ring liner contact
F_2, $F_{5/2}$	Roughness statistical functions
F_E	Elastic force on ring (slider rig)
F_G	Gas force on the back of the ring
F_T	Ring elastic tension force
f	Total friction
f_b	Boundary friction
f_v	Viscous friction
G	Ring end gap at free state

g	Switching parameter
h	Film thickness
h_c	Critical distance / gap
$h_{min},\ h_0$	Minimum film thickness
h_s	Ring face profile
k	Constant
ℓ	Connection rod length
l_c	Contact length
M	Floating liner mass
m	Mass
m_x	Mass flow through conjunction
m, n	Constants
N	Total number of computational segments
p	Pressure
P_{atm}	Atmospheric pressure
P_a	Inlet pressure
P_b	Outlet pressure
P_c	Cavitation vaporisation pressure
p_c	Perimeter of cylinder
P_G	In-cylinder gas pressure
P_s	Gas pressure at the upper rim of the floating liner
p_e	Elastic pressure
p_l	Perimeter of liner
P_r	Reformation point pressure
p_r	Pre-loaded (load cells)

q_x	Flow through conjunction
R	Radius of curvature for ring face
R_l	Load cell reading
r_{min}	Labyrinth seal mean radius
r	Film reformation point
r_0	Bore radius
r_{cr}	Crank radius
S_0, Z	Viscosity constants
s, s'	Intermediate integration variables
T	Temperature
T_0	Ambient temperature
t	Time
t_c	Time at which film rupture occurs
t_r	Time at which film reformation occurs
U	Piston velocity
v_l	Liner velocity (floating liner)
v_p	Piston velocity (floating liner)
W	Total load supported by contact
W_a	Load supported by asperities
W_h	Hydrodynamic load
x	Cartesian coordinate
x_c	Film rupture position (Swift-Stieber)
x_e	Film rupture position
y	Representative unwrapped ring dimension

Greek Symbols

α^*	Modified pressure/temperature-viscosity coefficient
β	Bulk modulus of elasticity
γ	Thermal expansion coefficient
ζ	Number of asperity peaks per unit area
η	Dynamic viscosity
η_e	Effective viscosity
η_0	Dynamic viscosity at atmospheric pressure
θ	Film ratio
κ	Average radius of curvature of asperity tips
λ	Stribeck oil film parameter
λ_c	Critical film ratio
μ_v	Coefficient of friction due to viscous shear
ρ	Density
ρ_0	Density at atmospheric conditions
σ	Composite root mean square roughness of the counterface surfaces
ς	Coefficient of asperity shear strength
τ	Viscous shear stress
τ_0	Eyring shear stress
φ	Crank angle
χ	Viscosity constant
ω	Engine speed

Subscripts

a, b	At the ring edges
c	At the cavitation (rupture) point
r	At the film reformation point
i	Grid index

Glossary of Terms

1D	= One Dimensional
2D	= Two Dimensional
AFM	= Atomic Force Microscope
AFR	= Air-Fuel-Ratio
BDC	= Bottom Dead Center
BP	= British Petroleum
CLA	= Center line Average
CNC	= Computer Numerical Controlled
CPU	= Central Processing Unit
EHL	= Elastohydrodynamic regime of Lubrication
FMEP	= Friction Mean Effective Pressure
IC	= Internal Combustion
IMEP	= Indicated Mean Effective Pressure
LCD	= Liquid Crystal Display
NEDC	= New European Emission Drive Cycle
NI	= National Instruments
Nikasil	= Ni-SiC Coating
OEM	= Original Equipment Manufacturer
PC	= Personal Computer
PTFE	= Polytetrafluoroethylene
RMS	= Root Mean Square
SAE	= Society of Automotive Engineers
TDC	= Top Dead Center

Chapter 1
Introduction

1.1- Preamble

Road transport underpins today's way of life. It is a necessity in the developed countries and an ever increasing trend for the developing nations. However, nearly all road transport is powered by fossil fuels which generate greenhouse gasses and are regarded as finite resources. Most scientists agree that global warming is affected by the excessive use of fossil fuels, hence, steps should to be taken to reduce, if not eliminate the greenhouse gas emissions. The worldwide transport sector accounts for 14% of the world greenhouse gas emissions, which is a very significant amount (5.88Gt CO_2 per year in 2000) **King (2007).** Within the transport sector, as shown in figure 1.1, the predominant form of propulsion is the internal combustion engine, whose design is very similar in freight trucks, buses, motorcycles, cars and vans. Therefore, the internal combustion engine is accountable for at least 75% of all global transport CO_2 emissions.

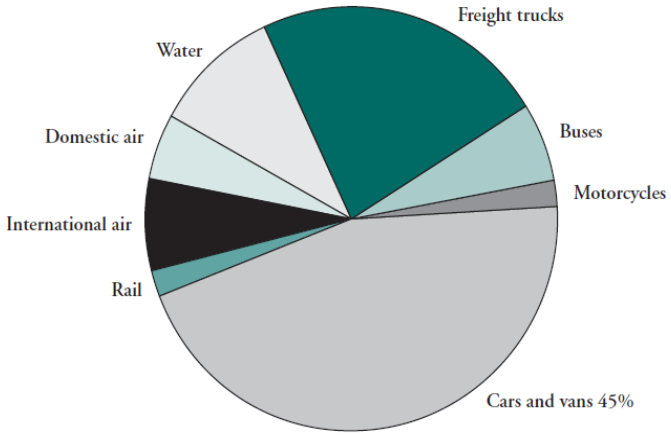

Figure 1.1: Global transport CO_2 emissions in 2000. WBCSD(2004) **King (2007)**

With the modernisation of developing nations and the introduction of very low cost motor vehicles such as the Tata Nano (which is currently for sale in India for approximately £1700), the use of internal combustion engine-driven personal transportation is being brought to new populations. As Table 1.1 shows, developing nations such as China and India will be the main driving forces for new vehicle development in terms of production volume. Although worldwide introduction of hybrid power trains and manufacture of electric vehicles has begun, the **King (2008)** report shows that the future trends (at least until 2030) point to the predominant use of internal combustion engine refinement and the addition of hybrid systems to its variants.

	India	China	Brazil	US
2000	5	7	137	480
2030	81	188	429	538
2050	382	363	645	555

Table 1.1: Projection of Car Ownership Per 1000 People. Goldman Sachs "The BRICs and Global Markets; Crude, Cars and Capital, Goldman Sachs Global Economics Paper No. 118, 2004. **King (2008)**

Electric vehicles, although gaining in popularity do not have the required range capabilities to compete with IC engines. Furthermore, their low production volumes and limited battery cycle life mean that the sale of most of these vehicles may be construed by some as an advertising ploy rather than a serious alternative to IC engines. Hydrogen powered vehicles, on the other hand, appear to have a better immediate commercial and technical viability in the mass transport sector as noted by **King (2007)**. However, the pertinent technology needs to be refined so that the associated costs may be decreased. Current costs of hydrogen powered vehicles are many times more than their IC counterparts and with a lack of refuelling infrastructure they will not play a large role in the short term (i.e. in the next 20 years **King, 2008**).

In order to decrease emissions in IC engines one should be able to increase vehicle economy and improve combustion. However, to achieve this successfully the cost of the required modifications should be small so that the end user is encouraged to bear the extra initial outlay set against the potential eventual benefits. When considering that the majority of vehicles sold in the short term will be at relatively low cost, many of the strategies that are being pursued in the developed countries may not be viable for the world's future predominant transportation market (e.g. China and India). Table 1.2 shows some of the technologies that can be implemented in IC engines to improve their efficiencies, compared with the costs of implementation.

Technology	Efficiency saving	Cost per vehicle (£)
Direct injection and lean burn	10 – 13 %	200 – 400
Variable valve actuation	5 – 7%	175 – 250
Downsizing engine capacity with turbocharging or supercharging	10 – 15%	150 – 300
Dual clutch transmission	4 – 5%	400 – 600
Stop–start	3 – 4% *	100 – 200
Stop–start with regenerative braking	7%*	350 – 450
Electric motor assist	7%*	1,000
Reduced mechanical friction components	3 – 5%	Negligible

** Figure quoted is for the whole drive cycle. Savings are much greater in urban driving conditions.*

Ranges derived from a number of sources, including the International Energy Agency (IEA), Institute of European Environmental Policy (IEEP), California Air Resources Board (CARB), Ricardo. Cost estimates derived using approximate conversion to Sterling.

Table 1.2: New engine and transmission efficiency savings, and indicative production costs. **King (2007)**.

It is clear that many of these technologies may be rendered as impractical or viewed as economically unviable for the new developing markets. However, what this highlights is that a reduction in friction could yield significant savings without exorbitant associated costs.

Significant work has been undertaken in recent years to improve thermodynamic efficiency of internal combustion engines and many large projects have been carried out to improve performance in this regard. New strategies have been implemented in

combustion management and significant improvements to efficiency have been made **(Balakrishnan, 2002)**. Although thermodynamic losses account for 80-90% of the losses at engine full load **(Winterbone**,**1981)** (with friction being the other major source of loss), friction significantly affects the engine output at idle contributing to approximately 20-30% of the losses in a typical urban driving cycle **(Uras**, **1983)**. **The Eddington Transport Study (2006)** concluded that almost 30% of travel time in major urban areas during peak periods is spent at speeds below 5 mph and over 50% at speeds less than 20 mph. This highlights that in a typical personal transportation vehicle friction contributes a large efficiency loss even when compared to thermodynamics, when used in urban areas. During cold-start and warm-up phases friction also contributes significantly to relatively high fuel consumption.

Literature suggests that the piston assembly is responsible for up to 60-75% of the mechanical losses within an internal combustion engine **McGeehan, (1978)**. The contribution of all losses is particularly highlighted by **Richardson (2000)** who presented power train losses based on the total engine fuel energy input (figure 1.2), This shows that although the mechanical friction is quite low at only 4-15% of the total output, the contribution of the pistons and rings makes up the majority of this loss.

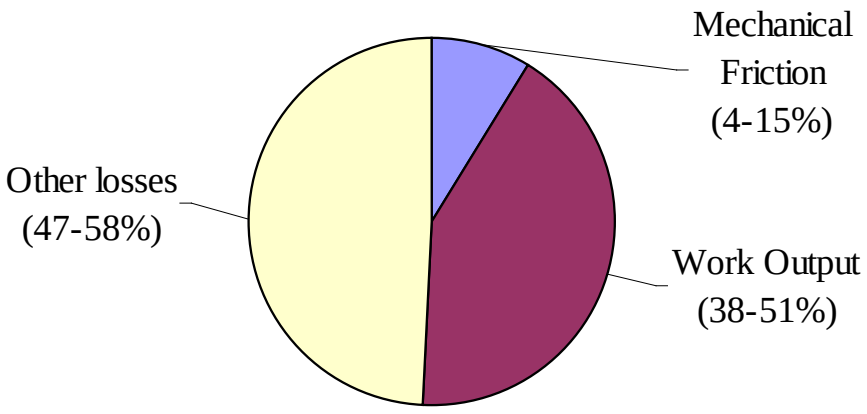

(a) Distribution of total energy in fired engine

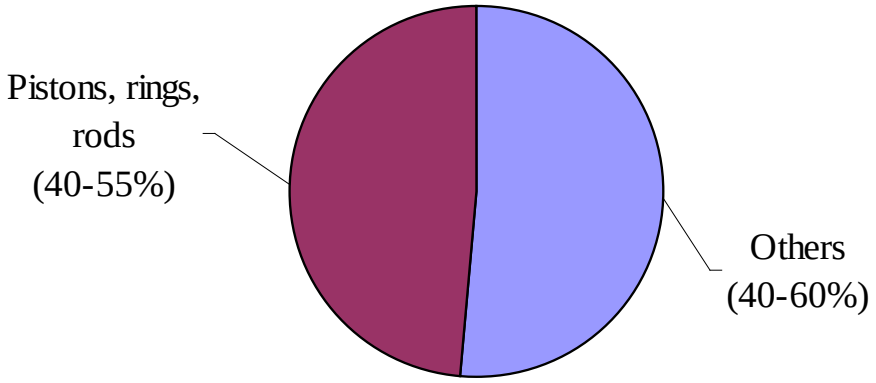

(b) Distribution of total engine mechanical friction

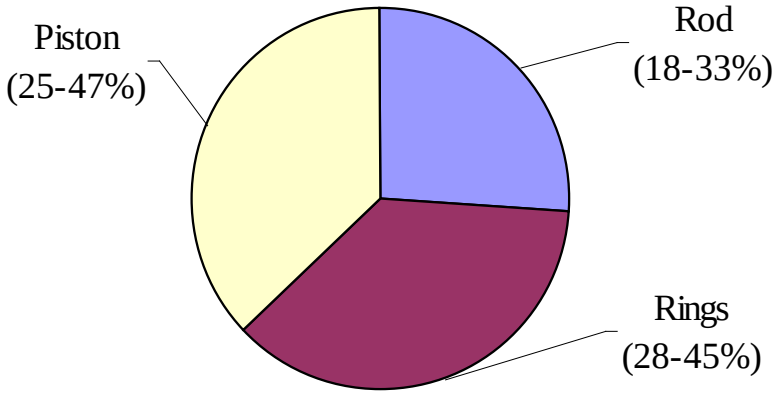

(c) Distribution of piston, rings and rod friction

Figure 1.2 Proportion of energy and losses in an IC engine (**Richardson, 2000**)

These interactions between frictional and mechanical losses have not received the fundamental attention that they deserve. With increasing demand on high performance, the piston is subjected to increasing loads and thus increasing losses, as development is driven by increased fuel efficiency and high power-to-weight ratios. These requirements lead to conflicting demands on the combustion system and tribological performance.

Extensive studies were carried out on reducing friction in the 1970's, which increased economy and decreased wear. The **Jost Report (1966)** showed that considerable savings could be made in industry if tribology was researched and improved upon, as shown in Table 1.3.

	£million pa
Reduction in energy consumption	28
Reduction in staffing	10
Savings in lubricant costs	10
Savings in maintenance/replacement costs	230
Savings in losses due to breakdown	115
Savings in investment due to higher utilisation	22
Savings in investment through longer machinery life	100
Total	**£515 m pa**

Table 1.3: Sources of Savings with improved tribology **Jost (1966)**

The research on mitigating friction is still onging today, also with regard to IC engine load bearing conjunctions however, in recent times, conjunction clearances have reduced and loads have significantly increased, therefore friction has also increases. The former is achieved in order to reduce noise and vibration, the latter as the result of a demand for higher performance (e.g. increased combustion forces). This is a trend that has been contrary to the claimed objective of reducing fuel consumption. Structural components have become more durable, but lighter in order to lower component inertias and increase power-to-weight ratios, whilst speeds have vastly increased. The role of surface topography and modifications have been studied since the Jost Report and have claimed to play a significant role in friction reduction **Balakrishnan (2002)**.

The current data, experimental techniques and models readily available in open literature do not encompass the increased speeds, loads and reduced clearances that are representative of more modern engines, particularly high performance variants. Oil manufacturers have put significant effort into producing lubricants that perform well in the harsh conditions representative of high performance engines.

However, these developments may be regarded largely as empirical and experiential. The effect of surface and geometrical features upon lubricant performance is still in its infancy, meaning that still more in-depth studies are required.

Due to thinning films, better descriptions of surface topography and improved lubricant rheology are needed for internal combustion engine tribology. In particular high performance engines need to be investigated as high operating speeds and loads are not enveloped by the existing knowledge. Much of the previous investigations have also been rather idealistic, not taking into account various aspects that lead to the transient nature of piston tribology, particularly mechanisms of heat generation and variations in combustion during seeminly repetitive steady state conditions. Modern sensor technology and vastly faster computing power will aid better measurements, monitoring and predictions.

The current investigation focuses on the ring-pack since it is generally considered to have the largest frictional loss in the internal combustion engine (60-75% of piston losses), with losses attributed to the piston accounting for nearly 45% of all the mechanical losses in a multi-cylinder IC engine. The top compression ring has the largest friction, mainly because of its better conformity to the cylinder bore/liner to guard against blow-by and reverse blow-by (its sealing function), as well as conducting the generated heat away from its conjunction as the thin lubricant film does not act as an effective convective medium.

1.2- Background

With the exception of a small number of engine variants such as Wankel rotary engines produced primarily by Mazda on limited models, the piston assembly of nearly all road vehicles and in fact all internal combustion engines is quite similar. Furthermore, nearly all road vehicles with the exception of some small motorcycles and scooters operate as four-stroke engines. Although piston-cylinder systems vary greatly in their size, materials, layout and design, it is quite easily possible to identify the major components discussed herein. A typical piston assembly is shown in figure 1.3.

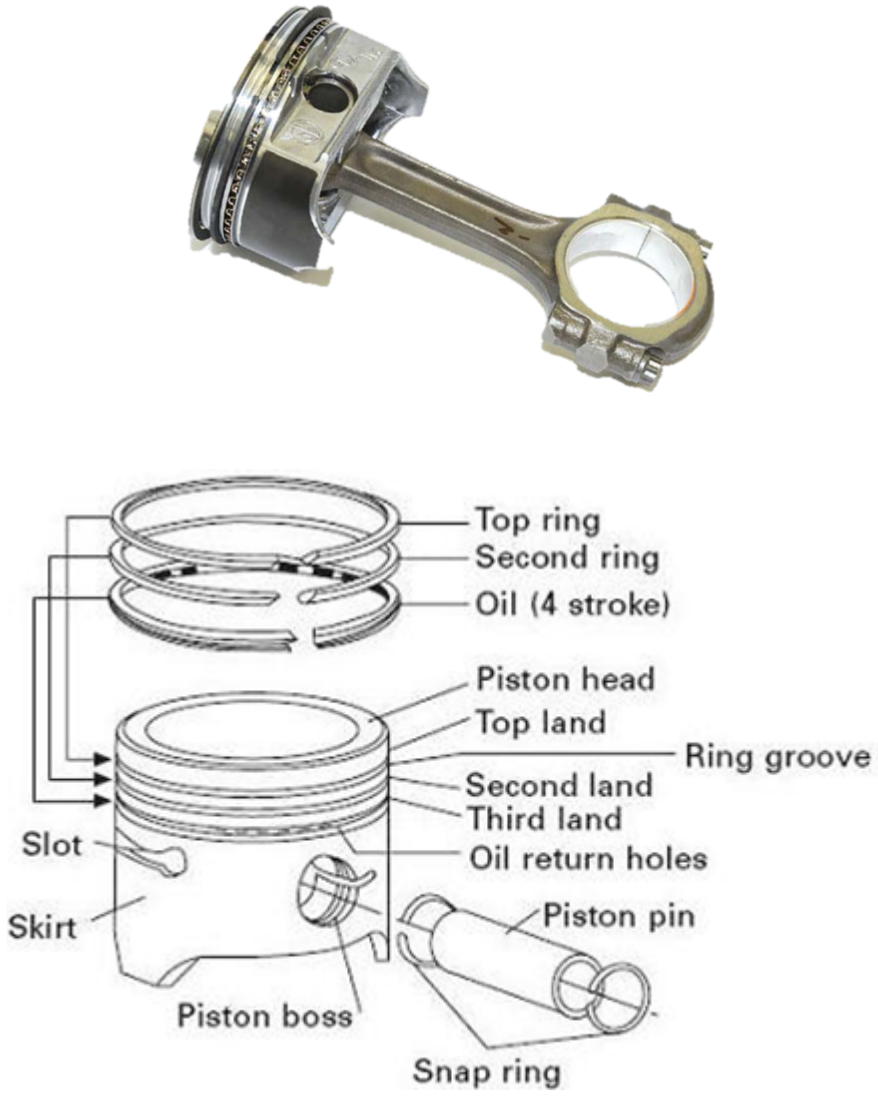

Figure 1.3: A typical piston assembly (**howautowork.com, 2012**)

As noted above the main frictional losses in an engine are from the ring pack. The ring pack is the collective term given to all of the rings fitted onto the piston. There are usually three rings per piston in a 4-stroke internal combustion engine. When oil consumption is not an issue such as in motorsport only two rings are used as this reduces the frictional losses.

Figure 1.3 shows a ring-pack arrangement on a piston, this is typical of all internal combustion engines.

The three rings all serve different purposes:

- The top ring is the compression ring. Its primary task is to seal the compression chamber, guarding against blow-by of gasses into the engine bottom-end and reverse blow-by of the lubricant into the combustion chamber. This means that the compression ring essentially acts as a pressure tight seal against the cylinder bore and the piston so that the combustion force is used to push the piston assembly downward with maximum efficiency. This ring is subjected to the highest temperature and is most prone to chemical attack as it borders the combustion chamber. The rings must act to transfer the heat from combustion to the cooled liner. Approximately 50-60% of the crown energy is transfered from the piston via the rings. The remaining heat-flow distribution is in the order of 20% through the ring lands, 20-30% through the skirt and 5% through gas and oil conductions **Heisler (1999)**. Nearly 70% of the heat transferred through the rings is carried away via the compression ring. The compression ring also scrapes the remaining oil film from the cylinder liner so that it does not reach the combustion chamber.
- The middle ring, also known as the secondary compression ring, or the wiper ring has the function of attempting to ensure a constant thickness of oil to the upper compression ring.
- The bottom ring is the oil control ring. This can take various forms. Modern engines use a 3-part oil ring which consists of two very thin scraper rings, separated by an expander. The purpose of the oil control ring is to control the

oil film thickness on the bore surface and return the excess oil to the sump via channels in the ring and the piston. Two stroke engines do not require an oil control ring.

The compression ring, therefore, has:

- the thinnest oil film thickness between it and the bore surface
- the highest operating temperature
- the largest deformation due to its fitment into the bore, piston secondary motions and application of combustion pressure
- the highest rate of heat conduction
- the lowest film thickness at piston reversals

These points amount to the worst tribological conditions, thus the motivation in the current research to investigate this particular conjunction.

Piston rings are an incomplete circle and sealing is due to their elasticity, deforming to ideally conform to the shape of the bore by exerting an outward force, striving to unwind (ring tension). The compression ring geometry within the piston is designed to allow a portion of combustion gas to pass over the top of the ring and exert pressure horizontally (in the radial plane of the ring) onto the back face (inner rim) of the ring. This pressure then directly adds to the pre-existing outward pressure – often by an order of magnitude **Howell-Smith (2010)**.

The tribology of compression ring–bore conjunction undergoes changes in regime of lubrication according to load, speed of entraining motion of the lubricant into the contact and its rheological changes due to contact pressures and particularly temperature. The regime of lubrication is also affected by geometrical variations in bore out-of-roundness, its thermoelastic distortion and that of ring modal behaviour, as well as its axial profile along its face-width in contact with the cylinder bore surface. Furthermore, surface topography of both the ring and bore play a key role as well as their contact mechanical properties; modulus of elasticity and Poisson's ratio, including those of any coatings.

In general, there are three regimes of lubrication that a piston ring can encounter throughout the engines cyclic strokes. These are broadly described by the Stribeck diagram (figure 1.4).

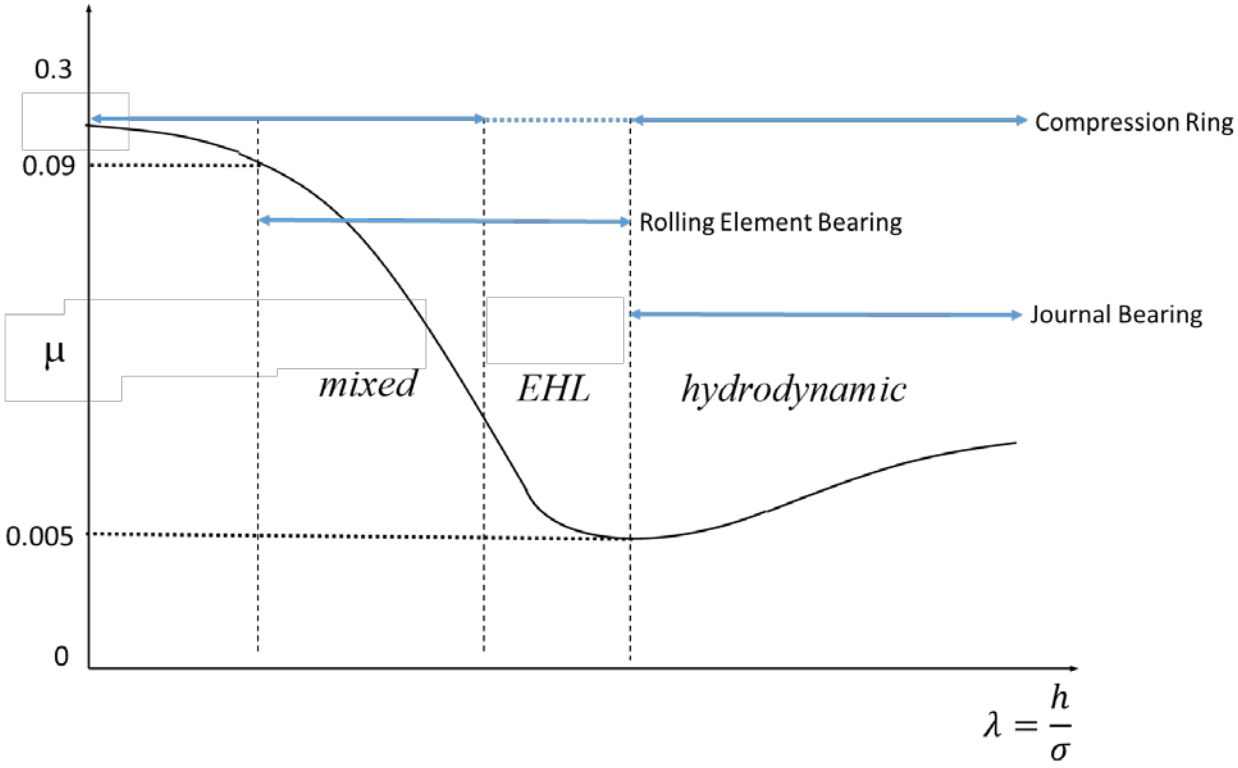

Figure 1.4: A typical Stribeck diagram

1.2.2 Boundary lubrication

Boundary lubrication is where direct frictional contact of clean surfaces occurs. No coherent film of lubrication is either formed or is of insufficient thickness compared with the root mean square (RMS) of contacting surfaces. In practice, when boundary lubrication occurs formed oxides or tribofilms often aided by active lubricant additives which adhere to rough surface topography reduce wear damage. Wear damage to the surfaces can take place through adhesion or deformation of their asperities. Boundary interactions are often noted at piston reversals at the top dead and bottom dead centres. The underlying cause of this is the momentary cessation of lubricant entrainment due to the reversal in motion of the piston. Therefore, to retain any film of lubricant one is reliant upon its entrapment in the contact domain by a combination

of squeeze film action and its retention within surface irregularities. Hence, smooth surfaces are likely to perform worse than suitably rough surfaces in this regard. This realisation has led to the introduction of surface features which retain pockets of lubricant by various means and thus improve frictional performance, such as honing of the cylinder liner.

1.2.3 Mixed or partial regime of lubrication

Mixed or partial regime of lubrication occurs when the composite RMS surface roughness of mating surfaces is less than or equal to the conjunctional film thickness. This condition is prevalent in the vicinity of the dead centres, prior and after reversals as the speed of entraining motion is insufficient to form a sufficiently thick film of lubricant not to be interrupted by counterfaces' surface topography. Mixed or partial lubrication causes the high points of the rough surfaces to rub off. This is clearly seen on a run-in cylinder liner as bands of polished regions near reversals. This regime still exhibits unacceptably high frictional losses. It is however, the most prevalent regime of lubrication, even in the natural world. In Nature surface protection is provided by various means. For example, in endo-articular mamalian joints, such as all human load bearing joints (hip, knee, etc) proteins lodged near rough articular cartilage guard against excessive friction when similar motion reversals occur, such as in the swing of the hip joint in the walking cycle. Modern lubricants are furnished with friction modifiers to emulate the same, one of the early examples of biomimetic approach. These friction modifiers form quite thin films of low shear strength that cling to the rough topography of surfaces. Although intiution points to smoother surfaces coated with hard wear resistant materials, rougher surfaces with addition of friction modifying additives that effectively adhere to surface topography makes for better scientific reasoning and observations as these provide reservoirs of lubricant and reduce surface to surface contact. Additionally, surface modification features, described above, encourage both bulk film formation as well as thin films of such additives.

1.2.4 Elastohydrodynamic and Hydrodynamic Lubrication

Beyond the region of dead centres due to sufficient speed of entraining motion a coherent film of lubricant is usually expected. This film is formed by hydrodynamic action. At quite high loads (high combustion pressures) and with materials (substrate, coatings or both) of lower elastic modulus contact deformation may also occur. If this action is accompanied by piezo-viscous behaviour of the lubricant an elastohydrodynamic regime of lubrication (EHL) would result. In fact, it is now well understood that EHL has been the Nature's choice for all mammalian highly loaded joints, meaning that the long process of evolution has arrived at this solution for almost all species. Natures choice of lubricant is synovial fluid with atmospheric dynamic viscosity similar to water (0.002Pas), with a few percent of hyaluronic acid, which dramatically changes its viscosity by orders of magnitude under hip joint loads of a few to several KN for an average human male (loads not dissimilar to those at maximum combustion in piston skirt and ring-pack conjunctions). The other constituents are glycoproteins which act as good boundary lubricants, even carrying phospholipids which act as active boundary layers which easily attach and detach from articular surfaces. Therefore, science has almost unknowingly stumbled onto the same solution that Nature has declared long ago (EHL was postulated by **Ertel and Grubin (1949)**, and Nature made its choice around 300 million years ago). Thus, implicitly biomimetics has been at the core of tribological research since at least the 1940s. However, understanding has evolved gradually and there is a long way to go to arrive at such magic lubricants or engineering surfaces as Nature has evolved.

Hydrodynamic and EHL film thicknesses are larger than the composite RMS surface roughness of contiguous bodies in contact. The surfaces are, therefore, expected not to be damaged, but in the case of EHL elastically deformed to provide an additional space (gap) for the lubricant to occupy under relatively high pressures. This is the optimum condition that one would hope to achieve in piston conjunctions. In fact with real engineering surfaces some "blunted" (worn) asperities may cause pressure perturbations themselves which further enhances the load carry capacity. This condition is referred to as micro-elastohydrodynamics, and was again discovered by

noting the manner in which rough cartilage surface smoothens by individual interaction of its asperity pairs. It is, therefore, not surprising that introduction of suitable surface features in all forms of conjunction, including in piston-bore interactions increase the so-called load bearing capacity (enhanced lubricant film thickness to carry higher loads).

Piston rings used to be composed of cast iron. This, to a certain extent, is self-lubricating due to its structural surface porosity, which can act as reservoirs for entrapping lubricant. Cast iron is sufficiently lightweight to be used in a piston assembly, tough enough to withstand the forces of combustion, whilst also sufficiently elastic to deform and conform to the bore as the piston moves, providing an adequate seal. It is also corrosion resistant and able to provide a long service life. Cast iron is not soluble in steel which is used for the manufacture of cylinder liners, thus the chance of adhesion in the event of direct surface contact is reduced. However, due to the ever increasing demands of modern high performance engines, steel is now used as it has a higher strength and toughness than cast iron so it can be made smaller and lighter, increasing the power-to-weight ratio and reducing the reciprocating inertia. Steel has a greater resistance to thermal distortion, which means less deformation and ring tension relaxation over time. It is, therefore, an excellent base material for a variety of surface treatments that reduce friction and prolong ring service life. However, clearly a ring made of steel is soluble in a steel-based liner which means that if the lubrication regime tends to boundary or even mixed, then localised cold welding of asperities can occur (adhesion). This would constitute unacceptable levels of friction, as well as damage to the engine, including premature failure. Use of dissimilar materials for counter-faces or use of coatings have therefore become commonplace.

In conclusion, the piston-cylinder system and in particular the compression ring conjunction is subjected to a very complex range of interactions. The understanding of these interactions in terms of friction, lubrication and wear is an essential prerequisite for any palliative action to improve engine efficiency.

1.3- Aims and Objectives

The overall aim of this research is to investigate the tribological behaviour of piston-bore conjunctions, with emphasis placed upon the compression ring–liner contact. In particular, determination of the lubrication regime in all parts of engine cycle is of interest, as well as prediction and measurement of friction and determination of wear characteristics.

1.3.1- Specific Objectives

The following are the specific objectives of this thesis:

- Develop means of accurate measurement of in-cylinder friction via development of a fully instrumented floating liner.
- Develop an appropriate engine test-bed for testing of high performance motocross engines.
- Recording all operating parameters such as engine speed with sufficient resolutions necessary to demonstrate exact in-cycle conditions.
- Create an analytical/numerical model to predict film thickness variation in the ring-bore conjunction.
- Integrate the above combined experimental-numerical study to determine the transient nature of the compression ring-bore conjunction.

1.4- Structure of the Thesis

Chapter 1 provides an introduction to the problem investigated and the motivation behind the reported research. It also sets out the overall aim and specific objectives.

Chapter 2 outlines a comprehensive review of literature on tribological conjunctions and a historical background. It also reports on literature specific to piston-cylinder systems of internal combustion engines with particular emphasis on the top compression ring. The literature includes the state of art and historical evolution of predictive methods as well as the reported means of measuring.

Chapter 3 describes the experimental setups used in this thesis for the investigation of frictional characteristics of sliding surfaces at basic science level as well as those in an internal combustion engine, particularly the piston-cylinder system. It also includes description of the developed infrastructure as well as instrumentation and methods of measurement.

Chapter 4 is devoted to the description of the floating liner and its principles of measurement. The entire chapter is devoted to the floating liner design, manufacture and use because it forms the central contribution of this thesis and is regarded as one of the main contributions to knowledge.

It is important to determine physical characteristics of the sliding mating components. Therefore, chapter 5 is devoted to all aspects of the investigation related to surface topography and wear characteristics of components.

Chapter 6 provides experimental procedure with the slider rig as well as the floating liner and other tests carried out carried out with the internal combustion engine. Detailed experimental procedure is described as well as results obtained for all engine running configurations; motored and fired as well as without cylinder head in place for testing the principals of operations of the floating liner.

Chapter 7 provides various analytical and numerical techniques developed in the current research for the prediction of tribological performance of the basic science simulation (slider rig) and IC engine under various operating conditions. Some comparative and combined studies with the experimental work are reported in this chapter.

Chapter 8 provides an overall conclusion of the research, achievement of aims, contributions made to knowledge as well as suggestions for future work.

Chapter 2: Literature Review

2.1- Introduction

This thesis concentrates on the tribological issues related to the top compression ring conjunction in IC engines. Therefore, the review of literature carried out in this chapter relates mostly, but not exclusively to this issue.

The review is largely divided into two sections. Section 2.2 is confined to the review of predictive methods, initially providing a brief historical overview of the field of tribology. This is followed by discussion of open literature on the application of fundamentals of tribology to IC engines with special reference to prediction of conditions in piston systems, and specifically to the ring-pack conjunctions.

Section 2.3 provides a review of experimental investigations of piston tribology, including results presented in open literature related to rig tests, motorised and fired engines.

Finally, section 2.4 provides an overall conclusion resulting from the review of all the literature, taking into account the conformance of numerical and experimental findings reported to date.

2.2- A Brief Historical Review of Tribology

Tribology is the science underlying lubrication, friction and wear. As such it embodies other key disciplines such as the study of surfaces, topography and their deformation behaviour (contact mechanics), as well rheology of fluids/lubricants.

The main aim in tribology is to guard against excessive friction and wear. It has long been realised that in order to achieve this key objective a film of a substance that shears readily without excessive friction should be maintained in the conjunction between opposing loaded solid surfaces in relative motion. There is plenty of evidence that this was instinctively understood even in the ancient times. **Gohar and Rahnejat (2008)** cite a bas-relief from ancient Egypt, showing one of the workers pouring liquid from a flask onto a track along which a wooden sled, carrying a monumental statue is being dragged. There are even earlier depicted examples of roller bearings in the form of tree trunks used under sleds as depicted in their own drawings in the tomb of Djehutihotep as moving massive stone blocks on sledges with runners lubricated with a liquid according to **Bard (1999)**.

There are plenty of examples of gearing systems from the ancient times, such as many potters' wheels, presumably running relatively smoothly, which means that some form of lubricant was used in their teeth pair conjunctions. The potter's wheel dates back to at least 3129BC, where a surviving one was found in the modern day Iraq, pointing to its original use in Ur, Mesopotamia as noted by **Moorey (1994).**

A sophisticated planetary gearing system was found in 1900 off the coast of Antikythera, Greece. It is kept in the Archaeological Museum in Athens, and is known as the Antikythera mechanism. It represents a sophisticated use of gears which were presumably lubricated. X-radiographs of the mechanism *in situ* within the solidified sedimentation appear to show intact teeth with no undue signs of wear, which would have been significant if no form of lubrication was used according to **Bromley (1990)**.

In the middle ages many forms of bearings, cams, pistons and gears were developed and used, all with the use of lubricants. Interesting and well-known designs were put forward such as wooden gears by Da Vinci, particularly in his proposed vehicle (**Codex Atlantikus, 1519**). Codex Atlantikus also includes helical gears, proposed by da Vinci as a part of his design for his now famous flying machine. **Gohar and Rahnejat (2008)** also briefly describe the design of a bobbin bearing by **Da Vinci (1495)**.

The history of pistons, the subject of this thesis, also goes back at least to the 3rd Century BC. The invention of the piston, as known today in water pumps dates back to the Roman times. The first detailed description of a piston is attributed to Ctesibius (Technology Museum of Thessaloniki) **Usher (1970)**. His other contemporaries Vitruv and Heron of Alexandia also wrote about piston pumps around 250 BC **Wikander (2000)**. Aristotle had already explained the principle of a suction pump a century earlier, which would only work for pumping water for a height of around 10m. He saw this limitation as horror vacui or in other words Nature abhors vacuum. Of course successive suction and compression strokes between a pair of cylinders is required to raise fluids. This proper explanation was actually provided by Evangelista Torricelli, one of Galileo's co-workers in the 17th Century as noted by **Barrow (2002)**. There is no evidence that tribological issues in the early water pumps were considered. After significant development the water piston evolved to become an engine piston and the explanation for the compression-suction cycle was used by Henri Papin in 1680 to develop the first model steam engine (**Inventors, 2002**). Thereupon, the piston assembly has become an integral part of all forms of crank-slider mechanisms, including the internal combustion engine.

John Ramsbottom in 1854 developed the split piston ring which quickly replaced hemp packing that was used in steam engines up to that time **(Weiss, 2008)**, It was clear that the expanding steam pressure should be maintained in the chamber in order to displace the piston, and that some pressure was lost due to poor sealing. Furthermore, it was necessary to reduce the friction of the sliding piston by regulating the supply of the lubricant to the piston-bore conjunction, whilst also taking

the heat away from the contact by means of conduction. Hence, a number of rings were fabricated onto the structure of the piston to achieve these goals. Chapter 1 describes the intended functions modern of piston rings.

Although the importance of lubrication and its use to reduce friction has been instinctive, there is little evidence in literature pointing to any scientific understanding of the mechanism of lubrication. Like many other fields in science, Newton's description of viscosity in 1673 represents the first step in the evolving understanding of the mechanism of lubrication; viscosity of a lubricant (in general any fluid) being its most important property in fluid film lubrication (**Newton, 1687**). Prior to Newton a property such as viscosity was only surmised as the resistance of a fluid to motion. Aristotle explained that motion of all objects is subject to resistive media, which was a correct and very profound observation for the 4th Century BC. He noted that an arrow meets with resistance when piercing through air. However, he also claimed that the air, pushed aside by the arrow, then gathers behind it to help it along its path!

Newton, assuming a slow laminar viscous flow of a fluid between a pair of parallel plates, envisaged the fluid to comprise spherical molecules, regimented in layers. The flow of these layers relative to each other and relative to the solid boundaries would take place against internal friction between them and in shear. Layers of fluid in relative motion in shear move with different velocities according to the geometry of the solid boundaries. **Newton (1687)** assumed a parallel flow with a uniform velocity distribution. So when one surface moves relative to the other, layers of fluid entrapped between them move with a straight line gradient. This type of flow, in general is known as the Couette flow (due to surface velocities), and after the French chemist who first proposed a mathematical form for this.

Newton's description of viscosity is, therefore, in the form of a constitutive equation rather similar to the Hooke's law for stress-strain relationship within the elastic limit, proposed by his contemporary Robert Hooke. According to Newton:

$$\eta = \frac{\tau}{\dot{\gamma}} \tag{2.1}$$

where η is now termed dynamic viscosity, τ is the viscous shear stress and γ is the thermal expansion coefficient.

It has been known historically as Newtonian viscosity. Unlike solids, the constitutive relationship for fluids is between stress and shear strain rate, where the latter at any layer of height *h* in a film of lubricant according to the Newton's model is:

$$\dot{\gamma} = \frac{u}{h} \tag{2.2}$$

Now if in a parallel conjunction of film thickness h, one surface is stationary and the other moves at a speed u, the velocity distribution will be triangular. Then, the flow of fluid/lubricant through the conjunction would become constant. Hence, if the flow through a conjunction q is considered to be in the *x* direction, then:

$$q_x = \frac{u}{2}h \tag{2.3}$$

which is the area of the triangle. If mass flow m_x is considered at a constant density, ρ then the mass flow is simply:

$$m_x = \rho q_x \tag{2.4}$$

The Couette flow is the rate of flow through the conjunction as:

$$\frac{\delta m_x}{\delta x} = \frac{u\rho}{2}\frac{\delta h}{\delta x} \tag{2.5}$$

However, lubricated conjunctions are often load bearing and are not parallel flat surfaces. The conjunction has a converging-diverging shape, such as in journal, ball or roller bearings to their raceway grooves. Thus, the flow through the conjunction is subjected to a pressure gradient, which alters the velocity distribution across the contact from a triangular flow pattern **Gohar and Rahnejat (2008)**. Pressure variation causes additional flow, known as pressure induced or Poiseuille flow (named after a French medic) which is similar to the flow of water in a river from its source to its estuary. The generated contact pressures also affect its density and

viscosity, particularly the latter (see section 7.4). The Poiseuille flow at any point x along the direction of flow is obtained as:

$$m_x = \frac{\rho h^3}{\eta}\frac{\delta p}{\delta x} \tag{2.6}$$

and the pressure-induced flow rate is, thus obtained as:

$$\frac{\delta m_x}{\delta x} = \frac{\delta}{\delta x}\left(\frac{\rho h^3}{\eta}\frac{\delta p}{\delta x}\right) \tag{2.7}$$

The flow in any contact conjunction may be viewed as two-dimensional, where the third dimension is the film thickness. Additionally, mutual approach or separation of surfaces, for example due to cyclic loading or vibration, can also affect the flow rate through the contact. Thus, the continuity of flow equation is of the form:

$$\frac{\delta m_x}{\delta x} + \frac{\delta m_y}{\delta y} + \frac{\delta \rho h}{\delta t} = 0 \tag{2.8}$$

replacing for the flow terms in the *x* direction from the above, with similar flow in the y direction with a velocity *v*, then one arrives at Reynolds' equation:

$$\frac{\delta}{\delta x}\left(\frac{\rho h^3}{\eta}\frac{\delta p}{\delta x}\right) + \frac{\delta}{\delta y}\left(\frac{\rho h^3}{\eta}\frac{\delta p}{\delta y}\right) = 6\left\{u\frac{\delta \rho h}{\delta x} + v\frac{\delta \rho h}{\delta y} + 2\frac{\delta \rho h}{\delta t}\right\} \tag{2.9}$$

Reynolds (1886) derived the above equation by simplification of Navier-Stoke's equations, ignoring inertial, body and surface forces, only retaining the viscous force of the lubricant. The much simpler derivation above is also based on viscous action only and is similar to that detailed by **Gohar and Rahnejat (2008)**.

Reynolds' equation can be used to obtain the pressure distribution in a conjunction, providing the other usual unknowns in the equation can be described. These are h, ρ and η. Early solutions, including by Reynolds himself were for line contact geometry, for example an assumed long roller of radius R near a flat surface. With olive oil as the lubricant of choice for Reynolds' studies and clearances of the order of hundreds

of micrometres, the generated pressures were correctly considered to be insufficient to affect viscosity. Furthermore, for the same reason density variation may also be ignored.

also, one may ignore any side-leakage, thus: v=0, as the film thickness is usually very thin. Under steady state conditions there is no squeeze film effect:

$$\frac{\delta h}{\delta t} = 0 \tag{2.10}$$

Reynolds could obtain the pressure distribution from equation (2.9) when he assumed an infinitely long bearing:

$$\frac{\delta p}{\delta y} \ll \frac{\delta p}{\delta x} \tag{2.11}$$

for the analytical solution Reynolds assumed a fully flooded inlet:

$$p \longrightarrow 0, \;\; x \longrightarrow -\infty \tag{2.12}$$

and its exit boundary condition as:

$$p = \frac{\delta p}{\delta x} = 0 \; at \; x = x_e \tag{2.13}$$

where x_e is the film rupture position.

The procedure is detailed in chapter 7. Integrating the pressure distribution, Reynolds' obtained the line contact lubricant reaction as **(Gohar and Rahnejat**, **2008)**:

$$\frac{W}{L} = \frac{4.9 u \eta_0 R}{h_0} \tag{2.14}$$

where h_0 is the minimum film thickness, W is the total load supported by the contact, L is the contact length, η_0 is the dynamic viscosity at atmospheric pressure and R is the radius of curvature of the ring face.

Now clearly as the contact load *W* increases the minimum film h_0 decreases proportionally. This meant that at certain loads the film thickness would have been less than the surface roughness of his roller. However, absence of any wear scars was particularly puzzling to Reynolds. There must have been another reason belying lack of wear.

Ironically, the reason was already known, even if indirectly and probably not noted due to the difficult methods of communication and dissemination at the time. **Hertz (1896)** had considered localised deformation of ellipsoidal solids of revolution under loads which were sufficient to cause small strain surface elastic deformations. The subject is known as contact mechanics and is now closely allied to tribology. Hertz's localised elastic deflection obeys the conditions; $\delta \ll a \ll R$, where δ is the deflection, *a* is the footprint radius in a circular point contact and *R* the radius of a ball in contact with a semi-infinite elastic solid. It is clear that this elastic deflection can create a small gap, which may be occupied by a film of lubricant, separating the contacting surfaces, a fact which was only realised half a century after Reynolds' 1896 paper by Grubin based on his work with Ertel (**Grubin (1949)**). In fact, Hertz had died at the age of 27, 2 years prior to the Reynolds' paper. The combined hydrodynamic action of the fluid film and the elastic deformation of the contiguous surfaces were termed elastohydrodynamic lubrication (EHL).

In the intervening period from 1896 to Grubin's EHL, most tribological research was concerned with hydrodynamics which is applicable to conjunctions with relatively thick films and pressures of a few tens of MPa at most. The main application area for the theory was, therefore, conforming contacts such as journal bearings. With high loads and absence of any wear on counterforming contacts such as some meshing gear teeth. Authors including **Peppler (1936, 1938)** and **Meldahl (1941)**, using Hertzian assumptions calculated elastic deflection of surfaces. However, this additional gap did not account for the film thickness surmised from experimental observations. Others such as **Gatcombe (1945)** had suggested that piezo-viscous action of the lubricant may be responsible for the increased load carrying capacity of

concentrated counterformal contacts. This effect was also found to be insufficient to explain the observations.

The lubricant viscosity variation with pressure, generated in a narrow conjunction was appreciated by **Barus (1893)** who assumed idealised isothermal conditions as:

$$\eta = \eta_0 e^{\alpha p} \tag{2.15}$$

This relationship is now widely referred to as the Barus law. It was used by **Gatcombe (1945)** and later by **Cameron (1952)** to take into account changes in viscosity in concentrated counterformal contact. α is the pressure-viscosiy coefficient with the unit of $\frac{m^2}{N} or\ Pa^{-1}$, which makes the product αp dimensionless. When this product is assumed to be zero, equation (2.15) renders an iso-viscous behaviour of the lubricant: $\eta = \eta_0$ which was the solution used by Reynolds for his long roller and later with different boundary conditions by **Sommerfeld (1904)** for his long bearing approximation. The physical interpretation for $\alpha p = 0$ is that generated pressures do not affect the lubricant viscosity. However, it is evident that in lubrication with thin films, even those of few tens of a micrometre in Reynolds' time, such an assumption is untenable. Ertel and **Grubin (1949)** proposed that at the leading edge of the Hertzian footprint; $x = -a$, the pressures rise to reach those of Hertzian, or $\alpha p = 1$. This means that there is an inlet trail of lubricant from $x \longrightarrow -\infty$ (for fully flooded conditions) to $x = -a$ where the trail merges to the ellipsoidal pressure distribution predicted by the classical Hertzian theory. Note that the viscosity of the lubricant then becomes $\eta = e\eta_0$ or in other words nearly triple its value under ambient condition. This behaviour is known as piezo-viscous action. **Grubin (1949)** assumes that the lubricant film is then parallel in shape, following the deflection predicted by the Hertzian theory as the generated pressures are those of Hertz. Therefore, a combined piezo-viscous action and localised contact deformation can explain the absence of wear at moderate to heavy loads, the phenomenon that Reynolds was searching for. Grubin called this phenomenon elastohydrodynamics. A subsequent analysis by **Petrusevich (1951)** confirmed the **Ertel and Grubin (1949)** supposition. However, there existed the concern that the classical Hertzian pressure distribution

does not conform to the continuity of flow condition. **Dowson and Higginson (1959)** numerical solution detected a pressure spike in the vicinity of contact exit, where a dip in the minimum film thickness was also observed. This means that the lubricant upon entering into the contact with rising pressures has a significantly increased viscosity. It becomes almost like an amorphous solid. It is pushed along by the relative motion of the surfaces and the pressure gradient in the direction of entrainment. As the pressures are reduced from the peak Hertzian value (often termed as primary pressure peak in elastohydrodynamic contacts) the lubricant viscosity also reduces dramatically. This means that locally the load carrying capacity is reduced, giving rise to a secondary pressure peak (or pressure spike or pip as this is often referred to) and a dip in the film thickness is noted (minimum exit film). The size of the secondary pressure peak and its positioning within the contact is related to the operating conditions; load and speed, the inlet meniscus (supply of lubricant), mechanical properties of contacting surfaces and bulk lubricant rheology, particularly viscosity **Evans and Snidle (1982)**.

2.3- Piston Ring Lubrication: Predictive Methods

The conditions described above pertain to concentrated counterformal contacts, where under moderate to high loads a film of lubricant film is formed under the elastohydrodynamic regime of lubrication. **Gohar and Rahnejat (2008)** note that, depending on kinematics of contact and applied load, as well as materials of contiguous solids in contact and lubricant rheology, the film thickness is quite thin, usually below a couple of micrometers, and in many cases several tenths of a micrometer. This is not the case for conforming contacts, with very good degree of conformance, such as journal bearings or partially conforming such as piston rings to cylinder bore. In the latter case, subject of this thesis, partially conforming contacts result. In the case of the piston ring-pack, the compression ring is subjected to higher loads and in many instances a thin film of similar size to those in counterforming contacts may be predicted. However, the generated pressures are always quite low, of the order of a few tens of MPa at most. This means that significant lubricant piezo-

viscous action (significant changes in lubricant viscosity due to generarted pressures) are not usually encountered, although some degree of contact deformation, beyond that due to ring fitment and applied combustion pressure may be present. This form of contact, with deformation, but without significant piezo-viscous lubricant behaviour is regarded as iso-viscous elastic and is prevalent in many conforming contacts, in nature (such as in hip joints) and in overlay bearings in crankshaft support bearings. These conditions are often referred to as soft EHL.

Predictive methods used for piston ring lubrication may be sub-divided into two distinct approaches. Firstly, a simplified analytical solution may be used. This approach is based on simplifying assumptions that render the problem as one-dimensional (section 2.3.1). The other more representative approach is a two-dimensional numerical method (section 2.3.2).

2.3.1- Analytical Technique

In this approach the contact between the ring face-width and the liner-bore surface is studied. An analytical solution becomes possible, if an almost infinite line of contact may be assumed, where the pressure gradient in the circumferential direction along the ring perimeter may be assumed to be negligible compared with the variation along the ring face-width (i.e.$\frac{\delta p}{\delta x} \gg \frac{\delta p}{\delta y} \approx 0$). This assumption means that the length of contact is much greater than the ring face-width, if the ring is visualised as unwrapped; $\pi D > 30b$ according to **Haddad and Tian (1995)** and **Perera *et al* (2007, 2010)**. The advantage of this assumption is that Reynolds' equation reduces to:

$$\frac{\delta}{\delta x}\left(h^3 \frac{\delta p}{\delta x}\right) = 6\eta_0 \left(u \frac{\delta h}{\delta x} + 2\frac{\delta h}{\delta t}\right) \qquad (2.16)$$

Again, assuming no side-leakage and iso-viscous conditions. Analytical solutions for this have been obtained by **Sasaki and Mori (1962)**, **Rahnejat (1984, 1985)** and for the specific case of a piston compression ring by **D'Agostino *et al* (2002)**.

All these one dimensional analytical solutions also implicitly assume that the ring face-width remains the same, which is a reasonable assumption. They further assume that the contact is not subject to any deformation, meaning that hydrodynamic regime of lubrication is prevalent. **Perera *et al* (2010)** extended the analytical solution to take into account changes in lubricant viscosity as the result of heat generated in the contact. They obtained an average temperature rise for the lubricant temperature in the contact using an analytical solution of energy equation. The approach was based on the assumptions made by **Gohar and Rahnejat (2008)**. The energy equation is given as:

$$\underbrace{v_e \Delta u \theta \left(\frac{\partial p}{\partial x}\right)}_{\substack{\text{compressive} \\ \text{heating}}} + \underbrace{\eta \left(\frac{\partial u}{\partial z}\right)^2}_{\substack{\text{viscous} \\ \text{heating}}} = \underbrace{\rho u C_p \left(\frac{\partial \theta}{\partial x}\right)}_{\substack{\text{convection} \\ \text{cooling}}} - \underbrace{k_c \left(\frac{\partial^2 \theta}{\partial z^2}\right)}_{\substack{\text{conduction} \\ \text{cooling}}} \tag{2.17}$$

where v_e is the coefficient of thermal expansion of the lubricant, C_p the specific heat capacity of the lubricant at constant pressure and k_c is the lubricant's thermal conductivity. Δu is the sliding velocity of the ring relative to the liner surface and *u* is the speed of entraining motion of the lubricant into the contact. Compressive heating can be assumed to be small compared with viscous shear in heating the lubricant. Thus, the first term on the left-hand side of the equation may be ignored. Measurements of ring-liner film thickness and various predictions have shown that the film thickness in the compression ring conjunction is quite thin (up to 2-3μm), reminiscent of EHL films in thickness, although often in the hydrodynamic or mixed regime of lubrication, rather than in EHL. Thus, of the cooling terms (on the right-hand side of the equation), the conduction terms plays by far the most significant role. In fact, one of the key functions of the compression ring (described in chapter 1) is to conduct the heat away to the piston and bore. Therefore, the energy equation can simplify to:

$$\underbrace{\eta\left(\frac{\partial u}{\partial z}\right)^2}_{\substack{\text{viscous}\\ \text{heating}}} = \underbrace{k_c\left(\frac{\partial^2\theta}{\partial z^2}\right)}_{\substack{\text{conduction}\\ \text{cooling}}} \tag{2.18}$$

an analytical solution to the above yields the average rise in lubricant temperature in the contact, $\Delta\theta$. Knowing the inlet temperature to the contact as: θ_i, then the average contact temperature may be stated as:

$$\theta_e = \theta_i + k\Delta\theta \tag{2.19}$$

where the constant *k* recognises that not all temperature rise is through viscous shear and not all the heat is taken away through conduction. For journal bearings a value $k \approx 0.6$ is proposed by **Cameron (1970)** when conduction cooling is ignored in favour of convection cooling (note: thick films in journal bearings). Therefore, to solve the energy equation in an analytical manner a number of assumptions have to be made. Finally, the effective average contact temperature is found and a corresponding value for lubricant viscosity may be obtained from Vogel's equation. This effective viscosity, η_e is now used instead of the dynamic viscosity at ambient pressures in isothermal conditions; η_0. This is the approach used by **Perera *et al* (2010)** when they also assumed: $k = 1$.

2.3.2- Numerical Solutions

In the analytical one dimensional solution, the elastic force due to fitment of the ring in the bore is obtained per unit length of an assumed contact length (along the ring periphery) and added to the pressure load on the ring, which arises as the result of the pressure differential above and below the ring, assumed to act behind it, pushing it against the cylinder wall. This combined load is resisted by the lubricant. The one-dimensional solution, therefore, does not take into account the actual *in situ* shape of the ring. For this to be taken into account, a 2-dimensional solution to ring lubrication is required. This calls for a numerical solution of Reynolds' equation, which with

ignoring side-leakage, and any significant changes in lubricant density and piezo-viscous action of the lubricant becomes:

$$\frac{\delta}{\delta x}\left(h^3\frac{\delta p}{\delta x}\right)+\frac{\delta}{\delta y}\left(h^3\frac{\delta p}{\delta y}\right)=6\eta_e\left\{u\frac{\delta \rho h}{\delta x}+2\frac{\delta \rho h}{\delta t}\right\} \qquad (2.20)$$

note that effective viscosity is used, implying that through use of energy and Vogel's equation thermal effects can also be included.

Isothermal numerical solutions for ring-bore contact have been presented by **Ruddy *et al* (1981)**, **Ma *et al* (1997)** , **Bolander *et al* (2005)**, **Akalin and Newaz (2001)** and more recently by **Mishra *et al* (2008, 2009)**.

In **Mishra *et al* (2008)** a series of quasi-static solutions are used through the reversal at the TDC to ascertain the regime of lubrication. It was found that squeeze film motion plays its most significant role in this zone, particularly in transition from the compression to power stroke. However, the predicted film was found to be quite thin, of the order of the composite RMS roughness of the contiguous surfaces. Thus, a mixed regime of lubrication was found to be prevalent. This is confirmed by observed scuff marks and wear at the TDC position.

In recent times, the importance of surface modification at the reversal points; TDC and BDC have become commonplace in order to palliate against occurrence of the mixed or boundary regimes of lubrication in these locations. **Etsion (2005)** describes formation of small dimples which create micro-hydrodynamic wedges between the contiguous surfaces and thus increases the load carrying capacity of the contact. In another paper **Etsion and Sher (2009)** claim that an effect of these dimples is a reduction in the frictional losses in the piston system; claimed to be in the region of 3-4%. The same level of reductions is reported by **Rahnejat *et al* (2006)** through engine tests, where instead of dimples, so-called negative features such as grooves

were introduced by laser etching of cross-hatched liners, and also where the produced sharp edges of the grooves were removed through honning.

Mishra *et al* (2009) attempted to provide an estimate of film thickness under transient conditions and including surface topography, using R_k value under isothermal mixed regime of lubrication analysis. When they applied their approach to the experimental work of **Furuhama and Sasaki (1983)**, good agreement was obtained for most of the engine cycle friction.

The above analasys assumes a rigid compression ring, dissregarding its modal behaviour (in-plane, out-of-plane, twisting and fluttering motions). This is the assumption also used in this thesis. However, the modal behaviour of the ring is extensivly researched by **Tian (2002)** and more recently by **Baker et al (2012)**.

2.4-Experimental Investigations

2.4.1 Test Rig Based Friction Measurement

There are two main strategies for the measurement of friction in engine components, either to create a test rig that uses test components from engines under simulated conditions to what the components would experience in an actual engine, or to measure the frictional loads of the components inside the engine itself. The first is significantly simpler and allows for more control over the apparatus and the conditions. However, the results are usually not directly comparable to that of real *in-situ* engine components. The second is significantly more complicated as engines are not designed to incorporate the measurement equipment which would be used and the engine would require major modification to install the equipment. Such modifications may affect the performance and workings of the engine. The results of actual *in-situ* components are, however, far more realistic and reliable to those of test rigs and the results from any modifications can be directly tested on unmodified engines to confirm any potential gains.

Akalin (1998) devised a testing system that simulated actual engine conditions in friction and wear tests on piston-ring and cylinder liner assemblies. The device is shown in figure 2.1.

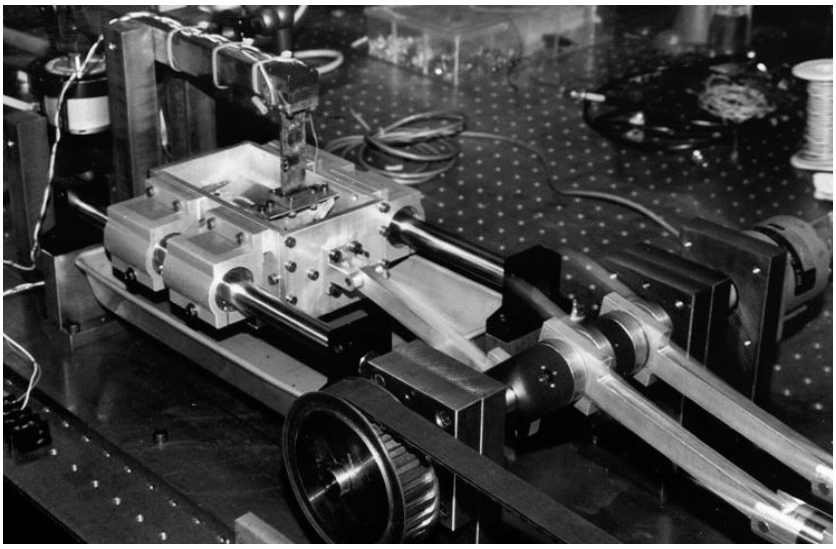

Figure 2.1: Ring and liner tester, simulating real engine conditions **(Akalin,1998)**

Liner segments were attached to a motored crankshaft arrangement which was supported by linear bearings, allowing it to reciprocate in the horizontal axial direction. Simulated ring-liner contact force was applied by a loading arm and an air cylinder. This force was precicely adjustable and friction was measured by a two-axis force sensor designed to measure applied normal force and friction force. Inertia forces were ballanced along the horizontal axis by a counter piston mechanism running opposite to the liner holder. The counter pistons were placed 180 degrees apart, so that harmonic inertia forces were also ballanced. Rotational inertia forces were ballanced using counterweights in the crankshaft arms. A large crankshaft pulley acted as an inertia disk and minimised angular speed variations. The assembly was mounted on an air table to isolate the apparatus from the laboratory floor. Encoders monitored movement and speed, oil flow was controlled with a syringe pump and the piston ring was free to rotate in the piston ring groove. Speeds of up to 700 rpm were used and all data supported mixed lubrication regimes of the stribeck diagram. This is the most complicated test rig that simulates real engine conditions in open literature. It gave accurate representations, but lacked the thermal, pressure and secondary motion forces that are present in a real engine. Many would argue that the amount of work required to build a rig like this is not worthwhile as its dynamics are vastly different from an engine.

Truhan (2005) used a simple apparatus which moved a loaded arm 10mm at 10Hz for an hour test (figure 2.2). The oil temperature, ring force and oil composition were then varied. This apparatus provided a very simple test rig that could predict friction coeficients and distinguish between different surface materials and oils in a very fast and cost effective manner without engine testing. Real piston liners and ring sections were used and the results obtained compared well with the lubrication effects at the end reversals. The liners in the rig showed significantly more wear than that noted in real engines.

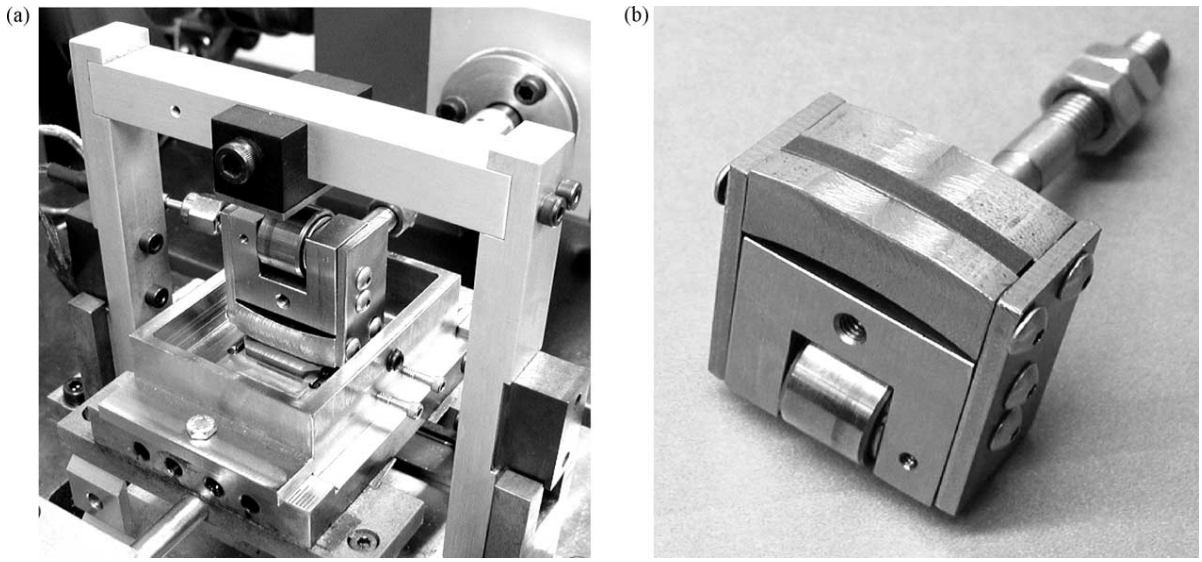

Figure 2.2: Truhan's simple ring and liner test apparatus **(Truhan, 2005)**

Much work has been reported in the area of simple test rigs and industry has moved away from the old pin-on-disk testers for complicated testing machines that accurately represent what actually occurs in an engine. These rigs, however, are only a guide as they simplify the system considerably. Real engine data can only be achieved from firing an engine. In recent times use of such rigs has been largely superseded by computer simulations that can run more reliably, faster and at a lower cost than the traditional test rigs.

2.4.2 Motored Engine Friction Measurement

The simplest form of friction measurement is to motor an engine via a dynamometer. This is refered to as a "direct motoring test" **Heywood (1988)**. However, this also includes pumping work, heat losses, windage losses and accessory loads. To reduce these losses the engine can be disassembled and measurements can be taken in various stages of disassembly. This process can attribute losses to particular component assemblies and would help to identify areas that can be improved. Although this is an excellent approach for some engine components such as an alternator or a camshaft which can be easilly removed, other components and assemblies such as the ring pack cannot be tested alone and must be lumped with

components such as the connecting rod bearings and big end journal bearings whose losses are not insignificant.

When direct motoring tests are conducted, it is important that operating conditions are as close to firing as possible and thus the oil and coolant must be heated to the engine operating conditions. An alternative method employed to achieve more accurate results is the “grab motoring test” **Heywood(1988)**, in which the engine is switched rapidly from the fired to motoring state. This ensures that the engine’s temperature distribution is as close to the fired condition as possible. However, this procedure is not possible with a partly dissasembled engine. As the engine is stripped down in successive steps, maintaining the fired operating conditions becomes increasingly difficult.

An approximate equivalent of the direct motoring test for a diesel engine is the “Willans line method” **Heywood (1988)**, in which a plot of fuel consumption versus brake output obtained from engine tests at a fixed speed is extrapolated back to zero fuel consumption. This produces data that correlates well with motored test results **Heywood (1988)**.

In order to measure the ring pack losses of a multi-cylinder engine the “Morse test” **Heywood (1988)** can be employed. This involves cutting out individual cylinders of a firing multi-cylinder engine and determining the reduction in brake torque while maintaining the same engine speed. The remaining cylinders drive the cylinder which has been deactivated. Care must be taken to determine the influence of cutting the cylinder out on fuel/mixture flow and exhaust flow on the other remaining active cylinders.

All of the above mentioned techniques involve measurements taken from a motored rather than fired engine, and this would not correspond to the true prevailing friction for a fired engine, rather its motoring requirements. The motoring losses are different from those of firing losses, due to:

1) Only compression pressure acts on the piston, rings and bearings. This is significantly lower than firing pressures and the loading cycles are completely different. These lower loads yield reduced friction.

2) Piston and cylinder bore temperatures are lower under motored operation. This results in higher lubricant viscosity and, therefore, increased viscous friction. In addition, piston-cylinder clearances are greater during motoring operation which tends to reduce friction. However, under firing condition, the lubrication of the top ring near the top of the stroke may be inadequate to maintain normal hydrodynamic lubrication with the higher gas pressures behind the ring. The resulting boundary friction in this region increases friction in a firing engine. Overall, the net effect of the lower piston and cylinder temperatures during motoring is rather unclear **Heywood (1988).**

3) In motored operation, the exhaust blowdown phase does not exist and the gases are discharged later in the exhaust stroke, having a higher density than under firing conditions. These effects can result in different pumping work.

4) When motoring, the net work done occurs during the compression and expansion stroke because of the heat loss from the gas to the solid boundaries, and because of gas loss through blowby. This work is not part of the true total friction work in a firing engine and should not be deducted from the indicated work of the firing engine to obtain the brake work. Heat losses and blowby are additional energy transfers to the indicated work, friction work and brake work.

Overall the motored techniques are excellent for determining friction of components that can easily be removed such as accessories, camshafts, tappets, valves etc with relative ease. However, for bearings and ring pack friction these tests are innacurate.

2.4.3 Fired Engine Friction Measurement

There are two techniques for true friction measurement in a fired engine; instrumenting the piston assembly or alternatively the liner assembly.

2.4.3.1 The IMEP (Indicated Mean Effective Pressure) Technique

The IMEP experimental technique developed by **Uras (1983)** involves very accurate measurements of cylinder pressure, connecting rod force, crank position and engine speed, which once known can be compared with a free body diagram and the forces in the axial direction can be calculated.

Uras and Patterson instrumented an engine (a Chevrolet 5 litre V8 modified for single cylinder operation) with highly accurate in-cylinder pressure transducers, accurate angular encoders (for speed and angular position) and a wheatstone bridge strain gauge arrangement on the connecting rod, coupled with extra strain gauges used to compensate for temperature and bending effects. In order to connect the strain gauges on the connecting rod to the stationary crankcase, a grasshopper linkage was also nescessary. This method required little engine modification however produced difficult to interpret results and speeds of up to only 2000 rpm. **Uras (1983)** was the first to attempt use this technique for high speed measurements.

However, some problems exist with this approach:

1) The process worked on the basis of taking a large force away from a large force to be left with a small answer.

2) Accurate calculation of inertial forces were required and even distributions have to be assumed especially for the connecting rod which can cause problems.

3) The addition of the grasshopper linkage changes the piston and connecting rod inertial properties and thus significantly changes the dynamics of the system.

4) The system was unsuitable for higher speeds due to the lag in recording the in-cylinder pressures, causing the data to be skewed at higher speeds (note higher speed sensor technology is now available, that was not in 1983).

5) The system was reliant on many different kinds of sensors and calculations. This increased the error margins of such measurements as friction was not the direct measurand.

6) The system was too slow to resolve what was happening at firing TDC due to the rapid load reversal, this being the most important issue for tribologists. Therefore, this technique had limited applications.

7) Although the system was relatively unobtrusive, it still required a grasshopper linkage which often requires a deeper oil sump, the relocation of engine bracing and a custom made connecting rod often leading to additional weight. The system also requires the addition of in-cylinder pressure transducers which can be fitted in spark plugs, but more often requires machining into the cylinder head. Therefore, this system, although relatively unobtrusive whilst in comparison with other techniques is difficult to implement and changes the inertias and dynamics of the components in question.

2.4.3.2 The Movable Bore Technique

The other form of friction measurement is achieved by not measuring what occurs directly in the piston system, but instead analysing the forces that are transmitted to the liner. This technique has many immediate advantages and disadvantages over the IMEP technique such as:

1) Measurements are conducted on a component that moves only very slightly, unlike the IMEP technique which measures the relatively large rigid body motions of the piston and connecting rod.

2) Analysing the inertial behaviour of a single piece solid liner is significantly simpler than analysing the multi-body dynamics behaviour of the connecting rod, small end bearing, piston and the ring pack, whose motion is not linear,

but dependent on the combustion pressure, lubrication and the slider crank geometry, as well as vibrations.

3) The IMEP method relies on the calculation of the power loss. As the combustion pressure accounts for the most significant influence on the system friction this must be deduced and is not as accurate as direct measurements such as in the movable bore technique.

4) A significant amount of modification is involved to instrument an engine with a moving bore, often only single cylinder engines can be used or multi-cylinder engines are used with disconnected/deactivated cylinders in the close proximity to the measured cylinder.

Taylor and Forbes (1943) made the first attempt to measure bore friction with an elastically mounted cylinder bore, which allowed small movements parallel to its axis. An optical system was then used to magnify these small bore displacements which were recorded with the use of motion-picture film. The engine could run in both motored and fired configurations with representative speeds of the engines of that era (1000-2500 rpm).

The movable bore that Forbes used was subject to many forms of excitations. These included the overall displacements, corresponding to the piston stroke; a very prominent excitation during the firing stroke and high frequency low amplitude noise whose origins were unknown. The prominent excitation in all recorded cases matched the calculated and measured natural frequency of the bore sleeve.

The movable bore was mounted elastically and surrounded by a water jacket. This caused the bore to vary in position depending on temperature and caused issues in calibration.

The conclusions from this work were that the technique showed “interesting possibilities”, but the results “must be regarded as of a preliminary nature”.

Leary and Jovellanos (1944) extended this work with the use of photomicrographs to make visual comparisons of the cylinder wall roughness and devices for measuring diametral ring tension. Two different film speeds were used to capture both high level of detail over short periods of time (such as Taylor and Forbes, running film at 25 inches per second) and the changes over time (such as the running-in stage), using a slow film speed of 0.295inches per second. TDC was marked on the film by having a set of breaker points on the camshaft which operated a lamp circuit and flashed every stroke, thus adding a vertical line on the film.

One disadvantage of this system is that the film had to be developed in order to see if the system was performing correctly. To overcome this shortcoming a device for providing continuous visual record of friction was added. This device consisted of an electromagnetic phonograph pickup, mounted rigidly onto the side of the cylinder. The phonograph needle was connected via a thin strip of steel to a blind plug, screwed into the spark plug hole. Oscillations of the cylinder sleeve imparted a motion to the phonograph needle and the output was fed through to an oscilloscope. A small amount of vibration was taken up by the unit and a disturbance was observed at the occurrence of a spark. However, this was easy to correlate. This eliminated the need for slow speed film testing from this point.

It was found that the calibration issues of the bore, not returning to the same place, was caused by air or steam bubbles building-up in the top diaphragm that held the movable bore. It was also found that drilling holes and connecting tubes at the top of the diaphragm to the coolant header tank removed this problem and made steady readings at constant temperatures.

The apparatus proved sensitive to ring scuffing and different ring materials and profiles. Work was also carried out to investigate the effects of running-in wear on evolution of friction, and how cleaning of components affected the friction.

Livengood and Wallour (1947) used the same apparatus as Taylor and Forbes and Leary and Jovellanos. However, they incorporated a crosshead arrangement, which allowed the engine to operate with only the piston rings in contact with the bore. In

order to increase the system sensitivity, the diaphragm springs were made much stiffer so that the natural frequency of the cylinder was increased. Due to the reduced sensitivity the measurement technique employed a more sensitive electromagnetic pickup. Tests were conducted to experiment with different piston ring and cylinder liner materials under different engine operating conditions. Calibration was performed by static weight loading as before. The tests were run for one hour and photographs of the oscilloscope were taken every 10 min. The equipment used is shown in figure 2.3.

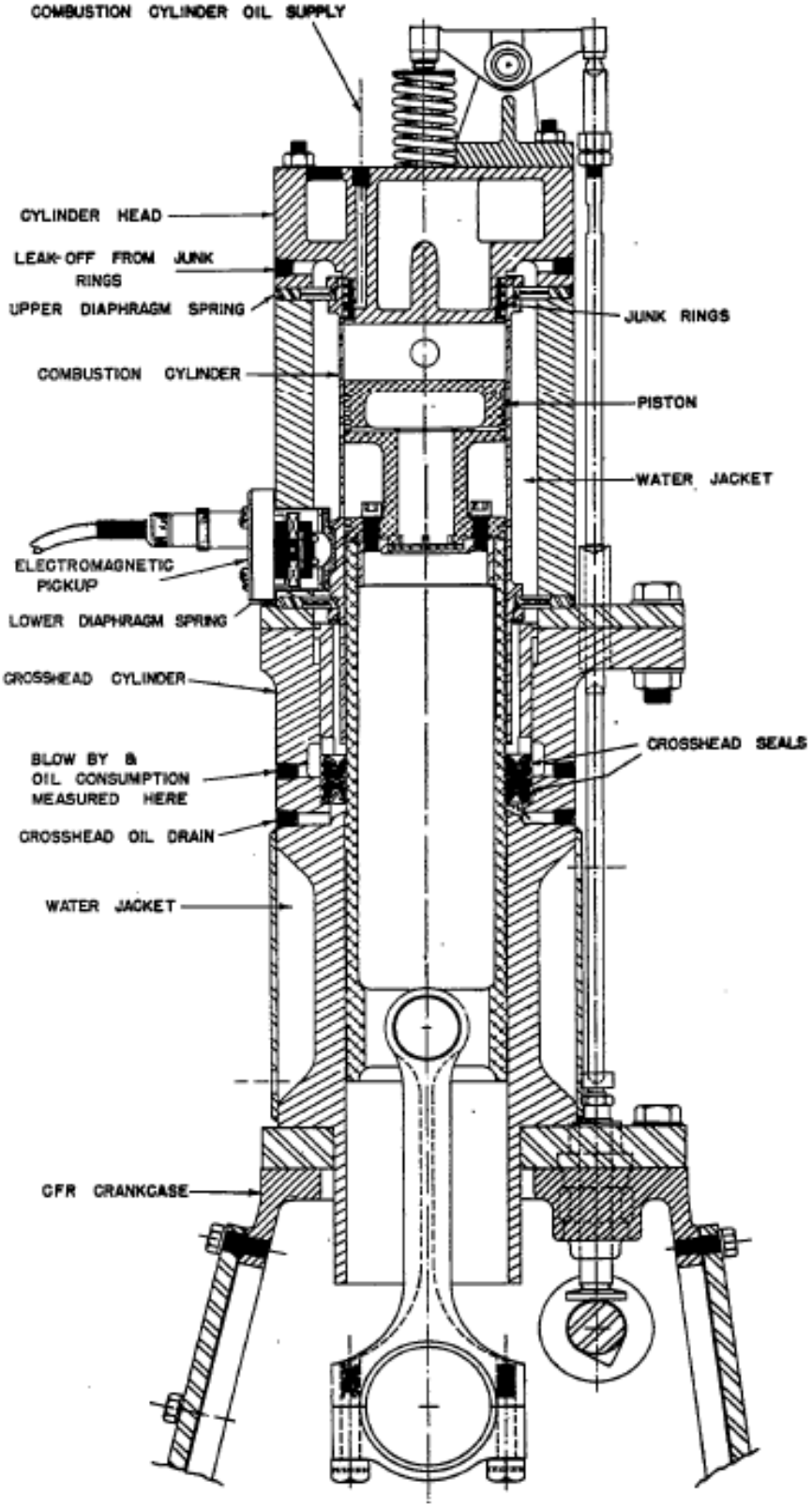

Figure 2.3: Perfected floating liner equipment (**Livengood and Wallour,1947**)

This work provided a basis for ring design and proved models and predictions. However, it exhausted all that could be achieved with the technology of the time. Recently with the development of piezo electric sensors and load cells more work has been carried out.

Furuhama (1980) was the first to build rigs that incorporated piezo electric transducers. This allowed the bores to move considerably less, whilst still providing high measurement resolution and accuracy. The first design moved just 1-2 microns, which made sealing the head considerably easier and more effective than the spring mounted rigs used in the 1940's. Significant sealing problems were still encountered and it took Furuhama several attempts to perfect his apparatus. Significant noise was also found to occur at high speeds and loads due to piston slap, even after a lateral stopper bar and elastomeric damper were fitted between the liner and the cylinder block to dampen these vibrations and an annular plate fitted to the bottom of the liner to provide resistance against axial motion. Testing was limited to 1400 rpm, where the generated forces were small and did not interfere significantly with the results. Some lateral motion was detected with the piezo transducers as the liner was mounted onto them, which were in turn mounted to the engine block.

Furuhama (1982) improved the equipment by significantly increasing the thickness of the cylinder block in order to increase its rigidity, adding lateral stoppers at the top and bottom of the liner so that the piezo transducers were only used to detect friction forces and the resulting displacements rather than as a device to support the liner. This was achieved by the addition of more piezo electric transducers so that frictional force was the sum of four equally spaced sensors. This equipment was used for a large number of experiments and large amounts of data were published, disclosing performance data for ring shapes, profiles, materials, finishes and oils. The only problem with this was that data was all from slow speed experimentation and from diesel engines.

Furuhama (1984) published a paper entitled “New device for the measurement of piston frictional forces in small engines”, which showed new devices that he and his colleagues had invented for the measurement of friction in both diesel and petrol engines. These devices built on their previous work and simply perfected the sealing of the head to the liner by reducing complexity and substituting the rubber O-ring seals for metal seals, which were designed and implemented in such a way that the gas forces balanced around them. These did not act to push the liner down. Results were obtained for tests of up to 30 hours continuous running and accurate measurements could be obtained to the extent of about half the maximum engine speed. Above this speed range the unbalanced forces of the engine introduced significant noise.

Yoshida (1990) used Furuhama’s equipment to study the effect of surface treatment on rings, with the apparatus shown in figure 2.4.

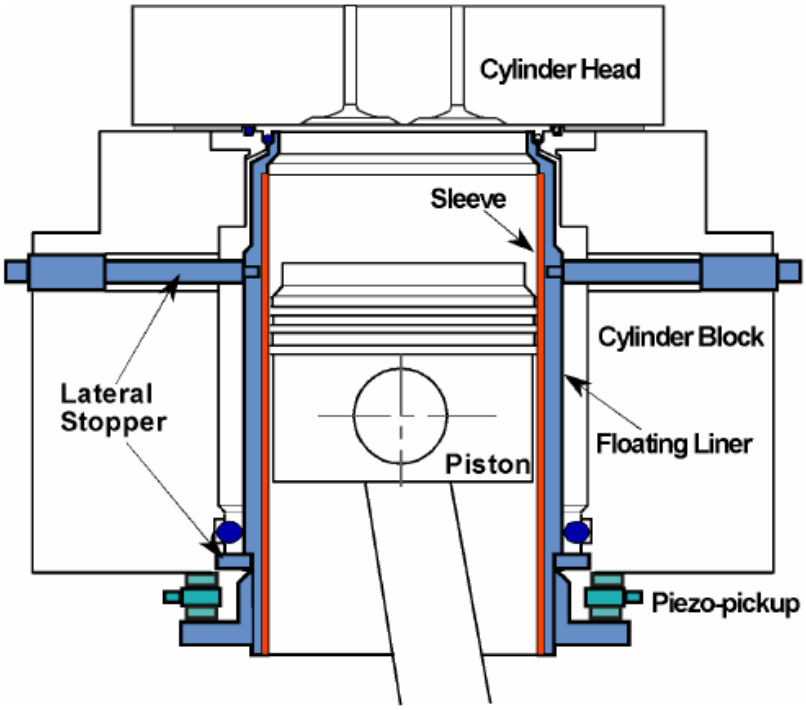

Figure 2.4: Furuhama’s perfected floating liner arrangement used by **Yoshida (1990)**

Howell-Smith (2010) further adapted the Furuhama's floating liner principle by clamping the liner in the centre rather than at the bottom. This design negated the need for the lateral stoppers. However, it meant that the piezo electric sensors were placed in a hotter location. Significant analysis had to be carried out in order to design the liner in a way that it would not vibrate, bellow or ring, whilst in service. However, once built the device would ensure that all of the frictional forces imparted by the piston and ring-pack could be measured by the piezo electric sensors.

To aid calibration the liner was envisaged to be mounted on 6 piezo electric transducers, 3 on the bottom and 3 at the top of a clover shaped plate mounted to the centre of the liner. This means that the sensor pairs mirrored the signal in correct operation and that signal processing as well as fault finding would be significantly simplified. This design is further refined and was manufactured as a part of this thesis.

2.5 Conclusion

Overall the regime of lubrication for piston mid-span is well understood, comprehensive numerical models exist and these are backed up by thorough documented experimentation. Slow speed reversal lubrication is also understood as this has been measured accurately and models support numerical evidence, such as scuffing.

High speed reversals, however, are not understood with a complete lack of experimental data in literature and little numerical work done, less than five papers cover high speed ring reversal lubrication and these are all from the last three years, as this is where the majority of the frictional losses occur this lends itself to further research especially experimentally.

Chapter 3
Experimental Set Up: Basic Science Rig and IC Engine

3.1 Introduction

This thesis presents a combined numerical and experimental investigation of the tribodynamics of the top compression ring-cylinder liner conjunction. A high performance motocross motorbike engine was chosen for the purpose of tribological investigation of piston-cylinder system, particularly the compression ring-cylinder liner conjunction. The chosen engine is Honda CRF450R engine. The underlying reasons for this choice are the engine's high speed (10,000 rpm), power (41kW) and torque (50Nm), (bore diameter of 96mm, stroke of 62.1mm). This choice is representative of the highest performing naturally aspirated engine technology (i.e. over 90kW/Ltr and 110Nm/Ltr), and its high speed and load characteristics envelope transient tribological conditions encountered in a very wide range of engines.

Significant effort was expended on the understanding of engine operation, particularly under controlled test-bed conditions to ensure good testing repeatability. A floating liner, described later was designed and manufactured with the engine modified to receive the same for direct measurement of *in situ* friction under various operating conditions. Operating the engine (in this case Honda CRF 450 single cylinder motocross engine) under the various aforementioned conditions enables fundamental understanding of mechanisms of friction generation. This is supplemented by numerical analysis, described in chapter 7.

3.2 Parametric Measurement

The problem fundamentally consists of two main issues; frictional power loss as well as wear of surfaces. Wear is caused when the lubrication film is inadequate and surface to surface contact occur, causing damage to one or both of the surfaces. Wear can be caused through a variety of modes including but not limited to ploughing, adhesion, abrasion and scuffing. The other problem is loss of power. Due to the nature of the piston cylinder system and the requirement of the sealing and constraining functions of the ring there will always be a power loss associated to the shearing of the viscous film, but through various means and keeping the lubrication in particular regimes this can be minimised.

There are also other important issues related to oil loss and degradation. The main purpose of experimentation was to understand and determine the frictional power loss and its cyclic characteristics. These are seen as prelude to any significant subsequent palliative work, which was another aim of an overall research project which included the work contained in this thesis as an integral part.

Therefore, the measurement of in-cylinder friction during various engine running conditions constitutes the main objective of this thesis.

3.3 The Sliding Test Rig

The ultimate goal of friction measurement is to employ an engine under realistic running conditions. However, there are many parametric interactions in a running fired engine. These interactions can lead to a plethora of effects that do not lend themselves to easy analysis of results. The principle of parsimony dictates reduction of parametric interactions in order to understand the fundamental underlying physics of a phenomenon, in this case mechanisms underlying generation of friction. Therefore, it was decided that a hierarchical approach would be developed for the combined numerical and experimental investigations of friction.

A pure sliding mechanism, free of other effects such as thermal distortion which is an inherent part of real fired engine would constitute a basic science experiment. In an engine, the bore is not an ideal right circular cylinder. It is out-of-round for variety of manufacturing and assembly reasons **Rahmani et al (2012)**. It may also be axially asymmetric. Thermal distortion of the piston and bore also exacerbate the geometrical complexity of the problem. The compression ring is subject to gas pressure loading in addition to the elastic restoring force (ring tensile force) which strives to adhere it to the bore/liner surface **Baker et al (2012)**. This combination of parameters makes the fired engine frictional losses quite complex to analyse, even when measured accurately.

To simplify the problem a simple slider rig was constructed. The final parameters required for the numerical analysis are provided in table 3.1. The rig is intended to simulate isothermally the operating conditions at TDC reversal for a fully conforming ring-bore contact under mixed and boundary regimes of lubrication. The load intensity (load per unit length) should represent that experienced at TDC reversal and ±10° crank angle from the compression stroke to the expansion stroke. This is achieved in this design (load intensity 400-850N/m). The sliding speed should be very slow (typically <±0.5m/s). Furthermore, the levelness of the floating plate should be in the range ±0.8μm. The final rig meets all of these requirements.

With a pure sliding mechanism, a flat plate can be made as an analogy to a floating liner. A strip with appropriate face-width geometry (ring) can be loaded and made to slide with respect to the floating low friction plate (liner) in the presence of a film of lubricant furnished on the surface. The motion of the loaded strip (ring) in close contact with the plate (liner) is resisted by friction, obeying Newton's second law of motion as:

$$\sum F = f = ma \tag{3.1}$$

where f is friction opposing the inertial motion of the floating plate assembly (i.e. the inertial force m mass and a acceleration), which can be accurately determined by

suitably calibrated piezo electric load cells. With reciprocating motion of the thin strip, friction is generated as a combination of hydrodynamic viscous shear of the lubricant as well as any direct surface interactions, particularly at strip reversal positions in the reciprocating cycle. Such a rig forms the basis for understanding the basics of friction generation of reciprocating sliding contacts. It also forms the basis for validation of the analytical technique which is subsequently used in the prediction of frictional behaviour of real engine piston systems.

It was decided that the slider test rig should be made so that the difference in materials and textures could be demonstrated simply and readily for other parts of the overall research Encyclopaedic programme, not covered by this thesis. In this manner, a flat section of material was used to replicate the ring and a flat plate used to replicate the liner. This approximation reduced the cost and time to manufacture many samples, enabling more tests to be conducted within a shorter time scale than would be required by an engine testing process.

The design and development of the slider test rig was part of the research embodied within this thesis (figure 3.1). Various methods of drive for this test rig were investigated including cam drive, a servo mechanism, hydraulic or pneumatic and a ball screw. The method selected was a low backlash ball screw as this was a simple and cost effective method of providing constant speed drive, whilst allowing a signal generator to impart a fluctuating signal superimposed upon the drive current so that the flat strip (ring) may even be made to flutter, as is often the case in an engine where the sliding velocity of the piston is subject to engine order vibration. This feature was not used within this thesis. It also allowed a large speed range and with the use of anti-backlash fixtures allowed for smooth and precise operation.

A weight applied to the top of the ring section allowed for an axial force to be imparted to the ring, thus the contact load between the flat ring and the floating plate.

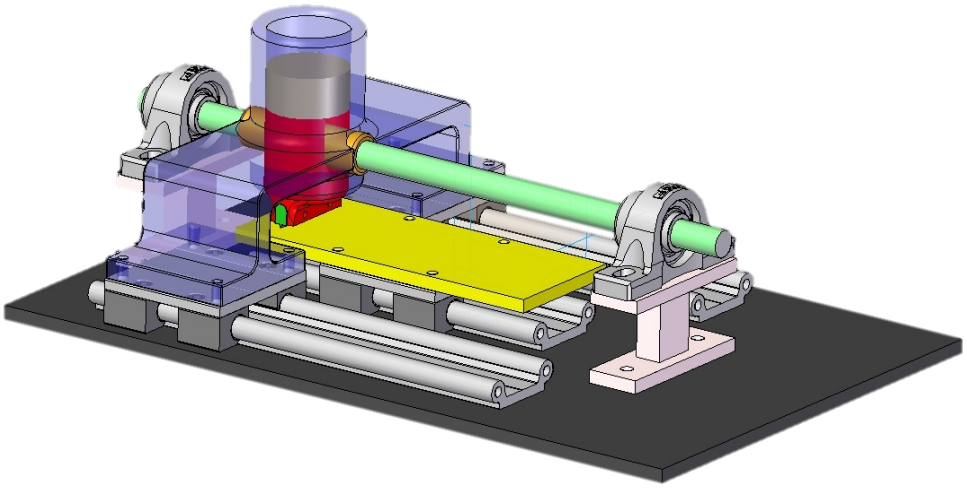

Figure 3.1: Slider rig with floating plate arrangement

The ring is allowed to slightly sway, thus it is constrained only from rotation. This eliminates problems associated with long wave waviness of the plate form. Figures 3.2 and 3.3 show the overall developed rig.

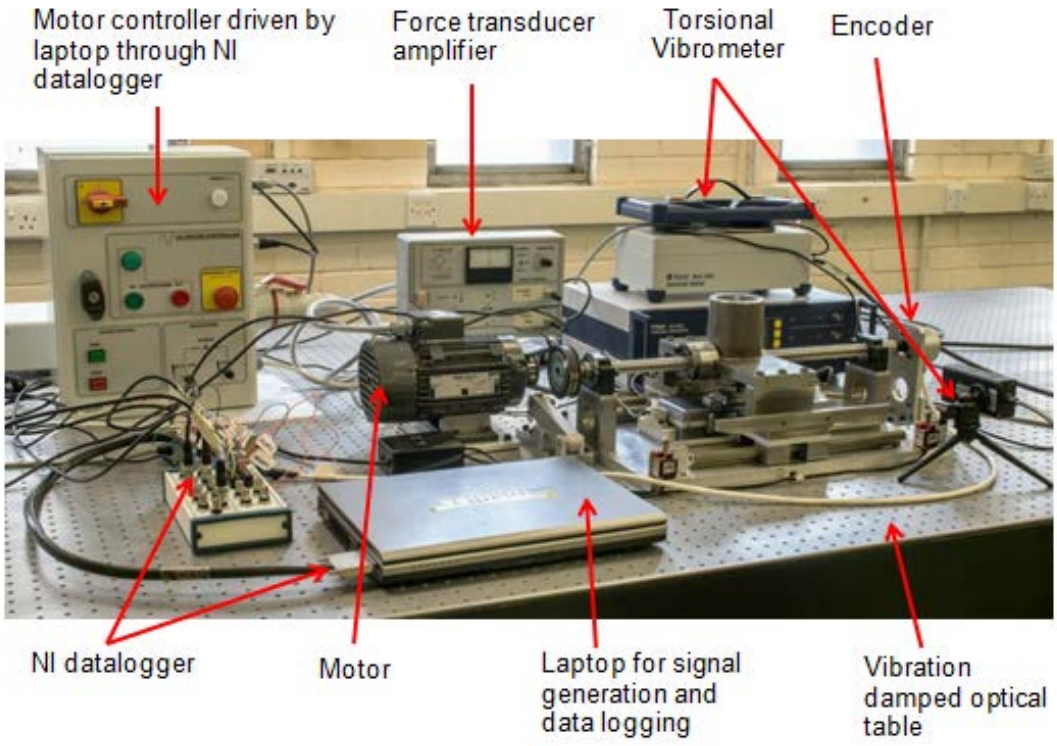

Figure 3.2: Fully developed slider rig

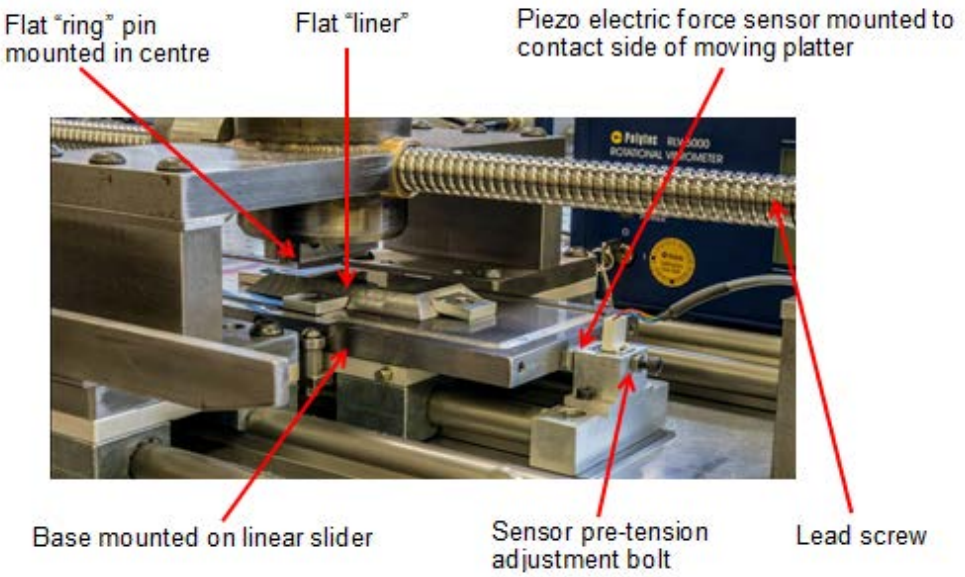

Figure 3.3: Detail view of “flat ring” in contact with “flat liner”

The ring and the plate were both lapped and their surface topography measured using an Alicona white light interferometer. Figures 3.5 and 3.6 show measurements taken from the flat ring and flat liner samples.

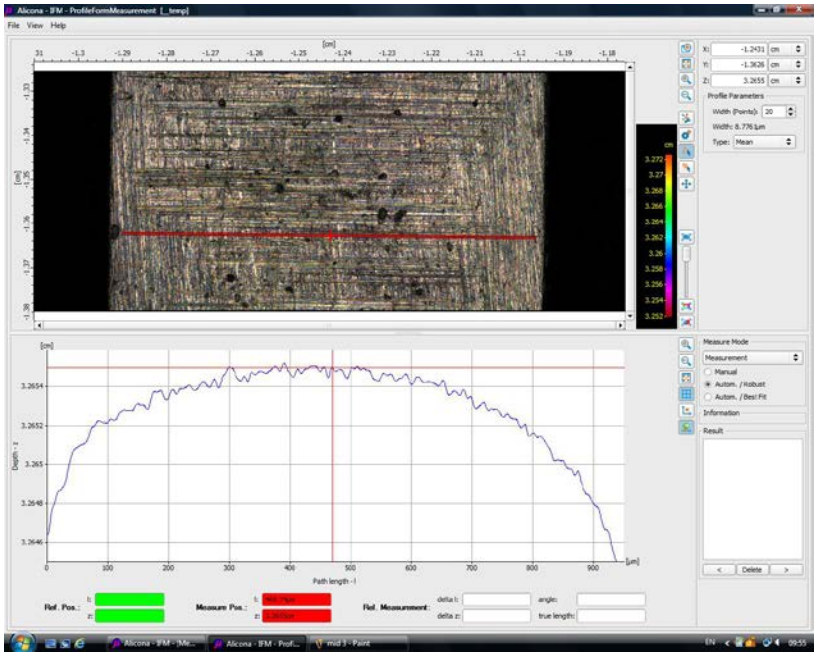

Figure 3.5: Alicona measurements of flat piston ring (not-run)

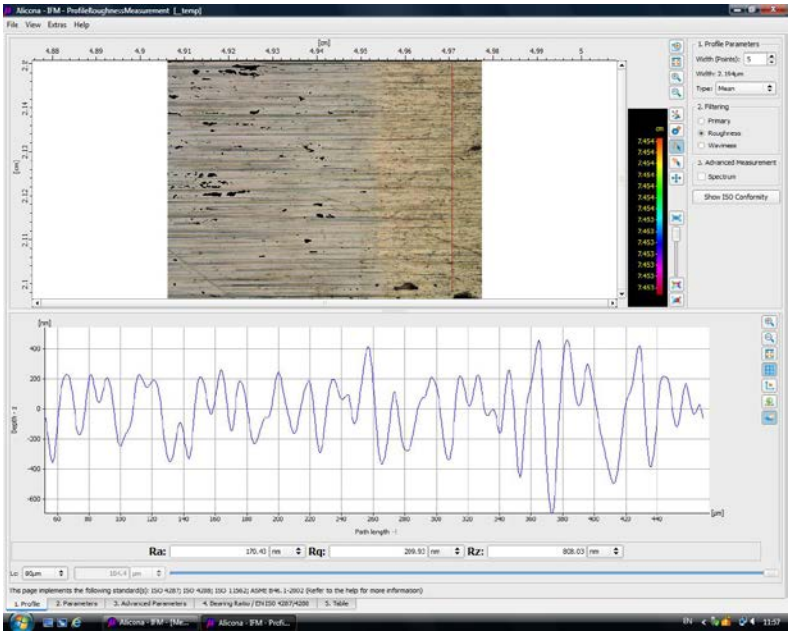

Figure 3.6: Alicona measurements of flat cylinder liner (not-run)

Ring Material	440C stainless steel, Hardened to 54 Rockwell C
Liner Material	Plate EN14
Ring Rq Surface Roughness	0.33 micrometers
Liner Rq surface Roughness	0.18 micrometers
Ring Width	1 mm
Ring Length	30 mm
Load	11 N
Lubricant	Castrol A3/B4 base engine oil
Lubricant Viscosity at 20°C	155-170 mPas
Lubricant Density	833 kg/m3
Greenwood and Tripp combined parameter (sigma*beta*zeta)	0.028
Greenwood and Tripp (sigma/beta)	0.0011
Coefficient of boundary friction	0.22
Ring Parabolic Profile Radius	31mm
Ring Profile Equation	$h_s(x) = -6.493x^6 - 49.845x^5 + 143.22x^4 - 98.541x^3 + 27.351x^2 - 17.338x + 7.4986$

Table 3.1: Slider Rig Parameters

3.4 Test Engine Selection

The area of interest in this study is restricted to the in-cylinder region of the engine. Due to the high cost of necessary instrumentation a single cylinder engine configuration was chosen, this being another reason for the choice of Honda CRF450R engine, although the main scientific reasons are noted in section 4.1. The key technical reasons for the choice of the engine were:

- Representative base parameters – bore, stroke, connecting rod length and fuel type representative of current and predicted future market OEM and motorsport technology.
- High speed and load capabilities – as this was a scientific study the data obtained should envelope all commercially available engines in speed and load characteristics (see section 3.1).
- Relatively low complexity – with fewer components comes less friction and less possibility for failure, although a high performance engine was required a minimum component count enables faster disassembly and assembly as well as the need for simplified analytical model (chapter 7).
- Replaceable barrels (as opposed to incorporated within the crankcase) - to allow for instrumented and modified barrels to be tested, preferably easily replaceable with a wet liner system as typical in motorsport applications.
- Water cooled – as some instrumentation was temperature sensitive and also this is typical in industry.
- Rolling element bearing as the connecting rod bearing - In a normal engine configuration, the big end bearing is an elliptic bore journal bearing. These bearings and other crankshaft journal bearing supports constitute 20-30% of all the frictional losses, whilst the piston system usually accounts for 40-50% of these parasitic losses (see chapter 2). Therefore, with a typical single cylinder engine having journal bearings, determination of losses using IMEP and isolating those attributed to the piston system is not an accurate approach. Rolling element bearings operate under Elastohydrodynamic regime of lubrication where friction is at its minimum as shown in the Stribeck diagram

(fig1.4). A reason for choice of the Honda CRF 450R single cylinder engine is its use of rolling element and ball bearing systems instead of the usual journal bearings. This reduces the share of frictional parasitic losses from bearings, thus improving the sensitivity of friction measurement by indirect means (i.e. IMEP) from the piston system.

Engines of the type described in the above requirements are commercially available and commonly used in the motorbike sector. Off road motorcycles match these requirements exceptionally well as they all use rolling element bearings (no journal bearings) (except for the small end of the connecting rod, where the wrist-pin bearing acts like a journal bearing, but at high load under these conditions a mixed regime of lubrication is most likely). The motocross motorbike engines are high speed and load machines and their simplicity lends them well to the application in mind. The largest market share of these single cylinder roller element based engines is Honda and Yamaha. Yamaha uses a novel 5-valve per cylinder arrangement which is not typical of most OEM vehicles and motorsport so this option was discounted, leaving Honda which employ a typical 4-valve per cylinder system.

After researching Honda engines it was decided that the most suitable engine would be the Honda CRF450R. R denoting the race application of this architecture, meaning that the wiring loom contains no provisions for lights, immobiliser, dashboard etc. and the engine system is as simple and lightweight as possible. The fuel system is carburettor-based, which is undesirable for this sort of experimentation but could be changed if required for an off the shelf single injector unit.

Table 3.2 lists the specifications for the engine. Figure 3.7 shows the engine architecture. It can be seen that the operating speed is quite high with maximum power at 9000 rpm (speeds of up to 12000 rpm possible). This would be the equivalent of a naturally aspirated 2L engine producing 183kW and 222Nm which is very close to the limit in both OEM and in the motorsport arena.

Engine type	Water cooled 4-stroke, 4-valve single cylinder
Engine displacement	449cm^3
Bore & Stroke	96mm x 62.1mm
Compression ratio	11.5:1
Max quoted power [specific power]	41kW@9,000 min^{-1} [91.31kW/dm^3]
Max quoted torque [specific torque]	49.8Nm@7,000 min^{-1} [99.80Nm/dm^3]

Table 3.2 Engine characteristics of Honda CRF450R (**Honda Motor Co. (2002**))

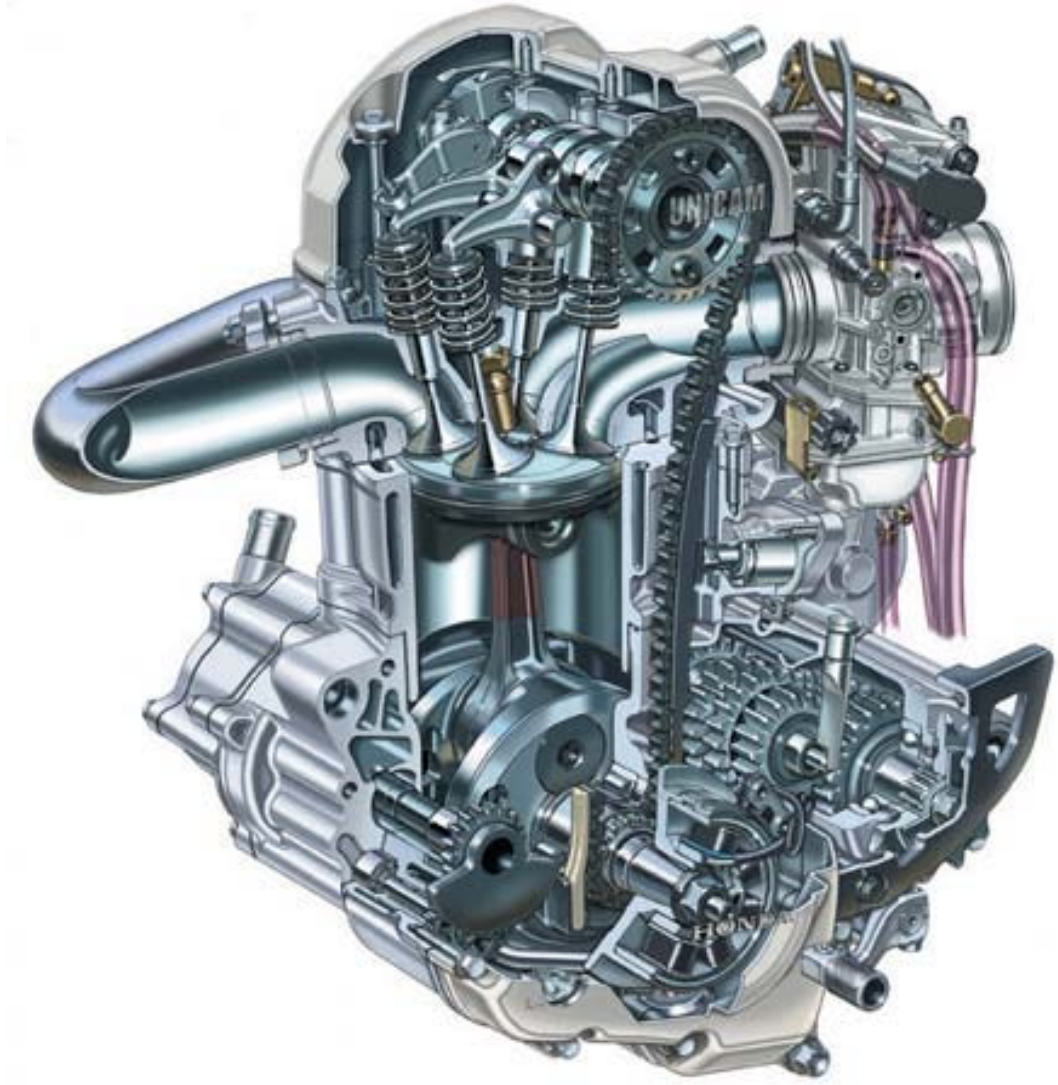

Figure 3.7: Cutaway of CRF450R engine (**Honda Motor Co. (2002)**)

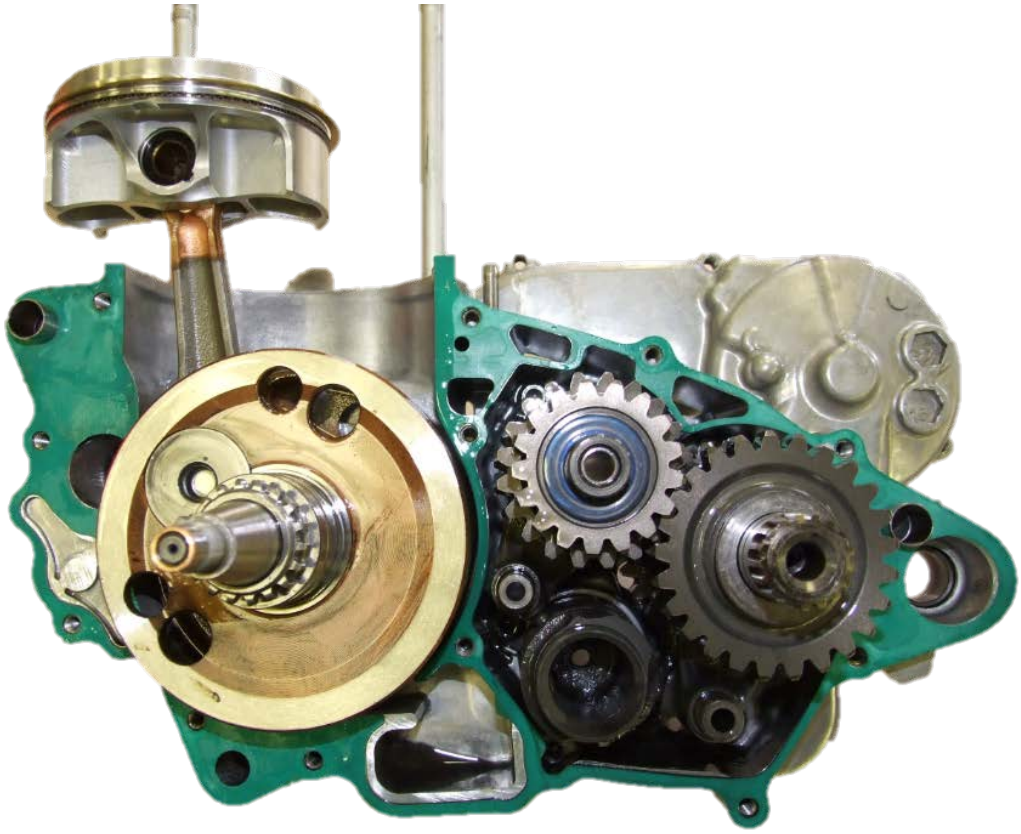

Figure 3.8: Honda CRF450R with cover removed

Although the Honda CRF450R looks like an ideal candidate there are problems with its architecture that require some modification:

- The cylinder block is a single unit incorporating the cylinder liner, oil channels, water cooling and chain tensioning system. This makes the modification process difficult and increases the costs of manufactured parts due to their complexity.
- The crankcase volume is extremely small meaning that fitment of a grasshopper linkage to the bottom of the connecting rod in order to route wires from the piston to the outside is almost impossible.
- There are a number of gears meshing in the gearbox, which although representing only a small amount of friction do add to the complexity of the system and introduce noise and vibration.

- The thin walled nature of the engine does not lend itself to constant assembly and disassembly. This, coupled with the aluminium and magnesium non-inserted threaded parts, means that there will be a finite life for each test component and this adds significantly to testing costs.

3.5 Modified Components

The standard Honda incorporates a cast cylinder block which houses the cylinder liner (mono-block arrangement, figure 3.9), oil and water channels and chain enclosure with tensioning system. This configuration had to be changed as it is extremely uneconomical to re-manufacture this part for every liner that requires testing. The original block was constructed from a nominally eutectic aluminium-silicon alloy (LM25/A356) with a bore surface furnished with a nickel-silicon-carbide electrolytic coating nominally 6-8% ceramic content, this surface treatment increases hardness, ensures that welding to the piston is not possible and increases wear resistance significantly.

Figure 3.9: Original Honda CRF450R OEM cylinder block

Motorsport wet liner conversions were investigated and it was decided to manufacture the cylinder block from two separate components; a holder and a

cylinder liner (figures 3.10 and 3.11). This arrangement simplifies the geometry of the test part, reduces cost and also makes modelling easier as the liner is pinned in known positions.

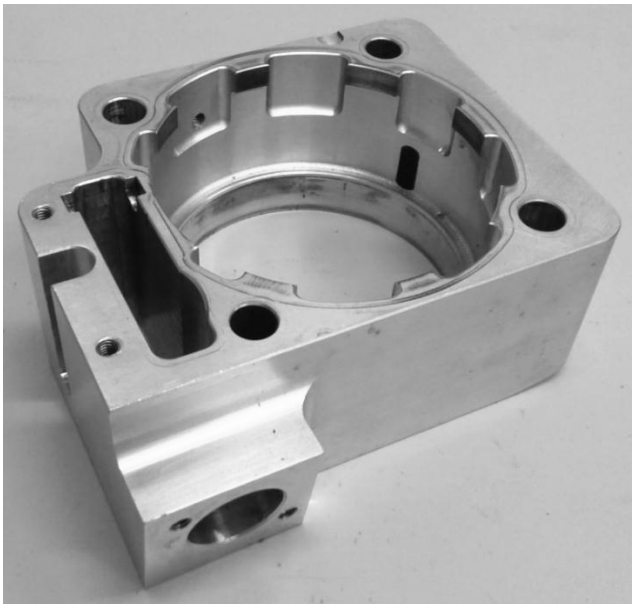

Figure 3.10 and 3.11: New wet liner and liner carrier block

The new arrangement has an identical oil and water system, pickup points and chain tensioning system. It incorporates a nitrile O-ring seal to prevent ingression of coolant into the crankcase. Both top and bottom OEM specification gaskets are used in the assembly. A thick-walled geometry of cylinder liner was used to minimise thermal and structural (bolted) distortion with the new liner allowed to distort less than the OEM specification.

The liner holder was machined from wrought (not cast) alloy AA6082 (HE30-TF). Liners were machined from various materials including AA4988 which is very similar to the OEM barrel material, AA2618 which is a commonly used automotive and motorsport non-ferrous liners and AA4988 which has a reduced thermal expansion and is commonly used in high performance road cars. All liners were coated with a nickel based electrolytic cylinder bore coating manufactured by Capricorn Automotive Ltd. containing co-deposited silicon carbide (Ni-SiC) the coating was

very similar in all properties to the Ni-SiC bore coating developed by Mahle Gmbh under the trade name of Nikasil that was used on the OEM liner. All tests for the work shown here were conducted with bores plateau honed to Honda OEM specifications.

3.6 Engine Test-Bed Set Up

The Honda CRF450R is mounted onto a custom CNC machined aluminium stand (Fig 3.12), which replicates the original mounting locations that are used in the recipient motorbike. This is critical so that the engine is not stressed, thus causing unknown distortions. This stand is attached to a very stiff structure via 4 anti-vibration solid rubber couplings to dampen all vibrations. The engine can be easily removed from the cell by the removal of the 4 bolts holding the anti-vibration mounts, as the base structure is aligned and shimmed to the required height for connection via a suitable propeller shaft to a transient dynamometer. This allows removal and installation without any alignment issues. The engine can then be easily removed from the stand by removal of the 3 custom made bolts.

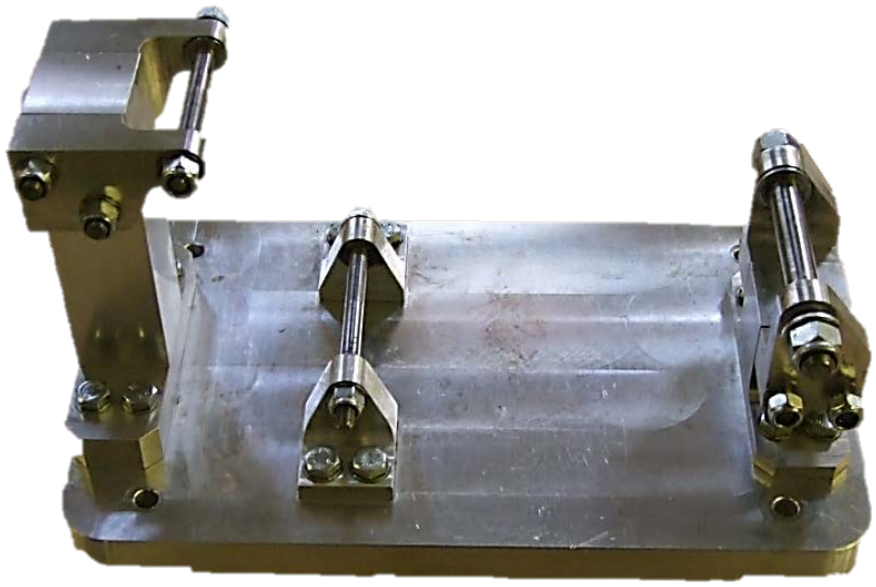

Figure 3.12: Engine stand

The engine stand is bolted to a very stiff welded box section structure, which is in turn bolted to I-beams which runs along the floor of the test cell. These I-beams are also used for the permanent connection of the dynamometer as seen in figure 3.13.

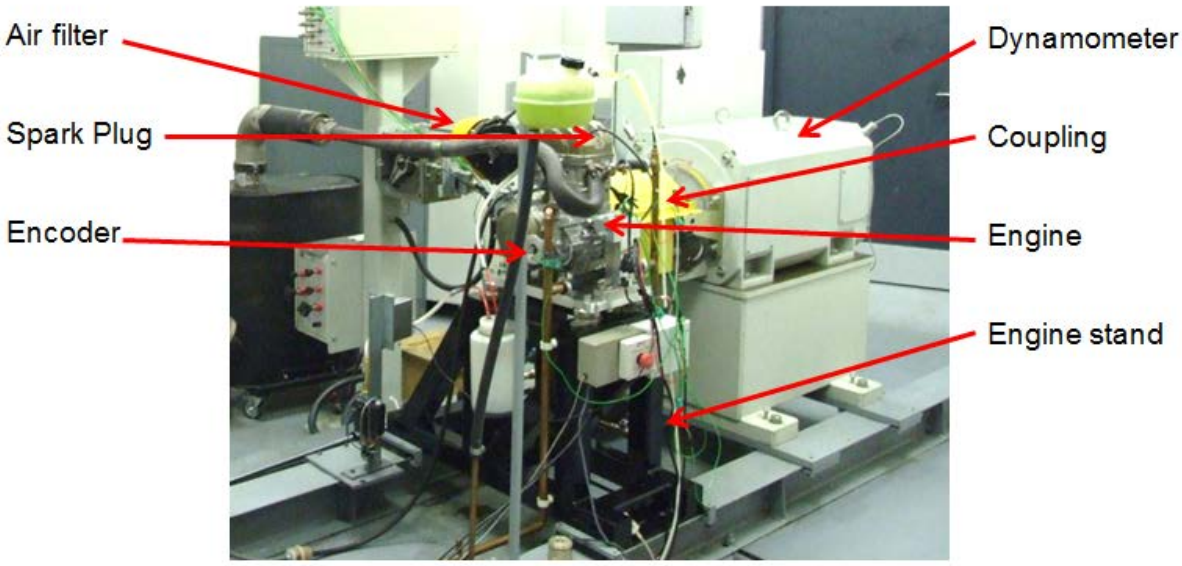

Figure 3.13: The engine test-bed

The engine drive is transmitted through the original sprocket which is attached to a custom made flange as shown in fig 3.14. This flange links the dynamometer drive to the engine and incorporates two flexible spider couplings for the propeller shaft connection to the dynamometer as shown in Fig 3.15.

Figure 3.14: Original Honda sprocket attached to custom made flange

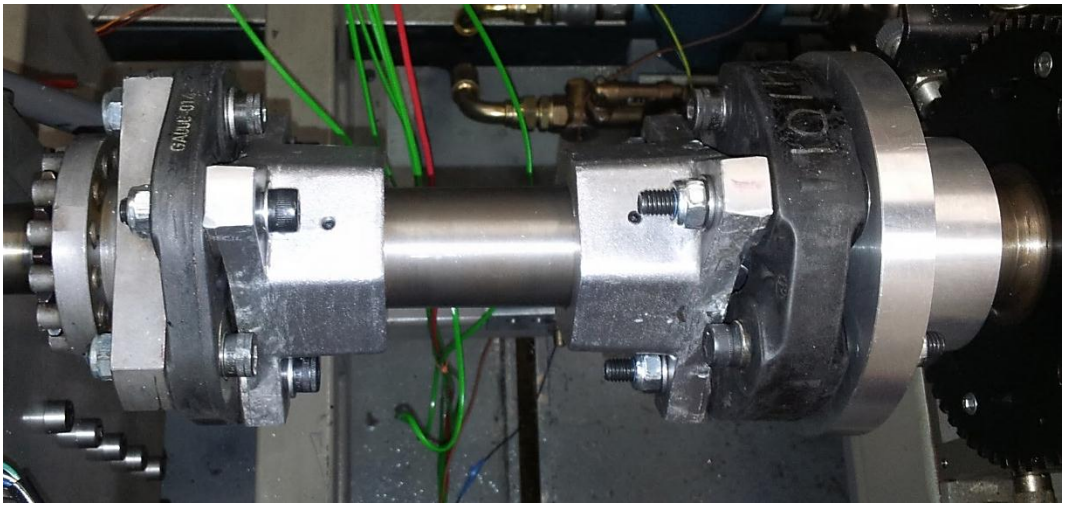

Figure 3.15: Coupling arrangement to the dynamometer

The dynamometer used is mounted in cell #8 of Loughborough University's transient test cell facility. This is a Ricardo S3000/3345 system which incorporates an Oswald 250kW dynamometer. The test cell provides built-in provisions for cooling via a chilled high volume recirculation circuit with thermostatically controlled coolers, mounted outside the building, an air supply which controls the pressure in the test cell and ensures that a slight negative pressure is maintained (so that all exhaust fumes are expelled and not leaked into the control room). A ceiling mounted exhaust extraction facility and a controlled fuel supply from externally mounted underground tanks are also provided. These existing services were all used apart from the fuel system.

Engine cooling is accomplished by an internal cell cooling circuit as shown in fig 3.16. The engines mechanical pump is kept, this pump is gear driven therefore flow is engine speed dependant.

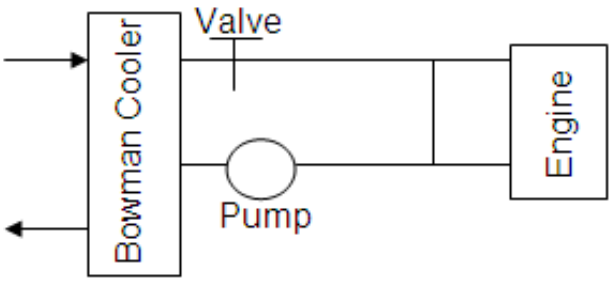

Figure 3.16: Engine coolant circuit diagram

The engine water temperature is monitored by thermocouples and the pump is activated when a set temperature is reached and then turns off when the temperature falls past a pre-determined point. Initial setup is achieved by adjusting the valve to ensure that accurate control is met by not letting large volume of cold water into the engine as this could cause damage through thermal shock. Adjustment of the valve is required for every differing test and or test speed as the engines internal mechanical pump is speed dependant. Although a manual process this is a simple solution which gives very accurate and repeatable results.

There is no active cell temperature, humidity or pressure control but all parameters are logged and correction factors are used so that the data from different and in some cases repetitive tests can be directly compared. Correction factors have to be used to adjust power and torque measurements to standard atmospheric conditions to provide a more accurate comparison between engines as they are affected by the pressure, humidity and temperature of ambient air **Haywood (1989)**. The correction factor chosen for this research is the SAE certified power correction **SAE J2723 (2005)** this is the industry standard correction and is used by the sponsors of this project. It is also used widely in publications as is the most documented correction standard therefore lending itself to research and publication.

All comparative tests are conducted on a back to back basis in a single day and an A-B-A test regime was always adopted.

Initial testing was conducted with the OEM Honda exhaust, but this did not meet the required sound limits imposed by the faculty. Therefore, a custom exhaust system was manufactured by Janspeed, UK. This exhaust has an 80 litre internal capacity and uses parts common to truck exhaust systems. An increase in the back pressure was observed, although the required sound pressure reduction of 120+db to 105db was achieved. Maximum power and maximum torque are now approximately 1500 rpm lower, but overall only a 1.5kW power decrease was observed. This brings the maximum power and torque to more representative speeds, but still envelope all the current technology for naturally aspirated engines.

The exhaust is connected to the engine via a standard aftermarket titanium exhaust manufactured by Micron and then connected to the ceiling mounted extraction via standard large bore extraction tube as shown in fig 3.17.

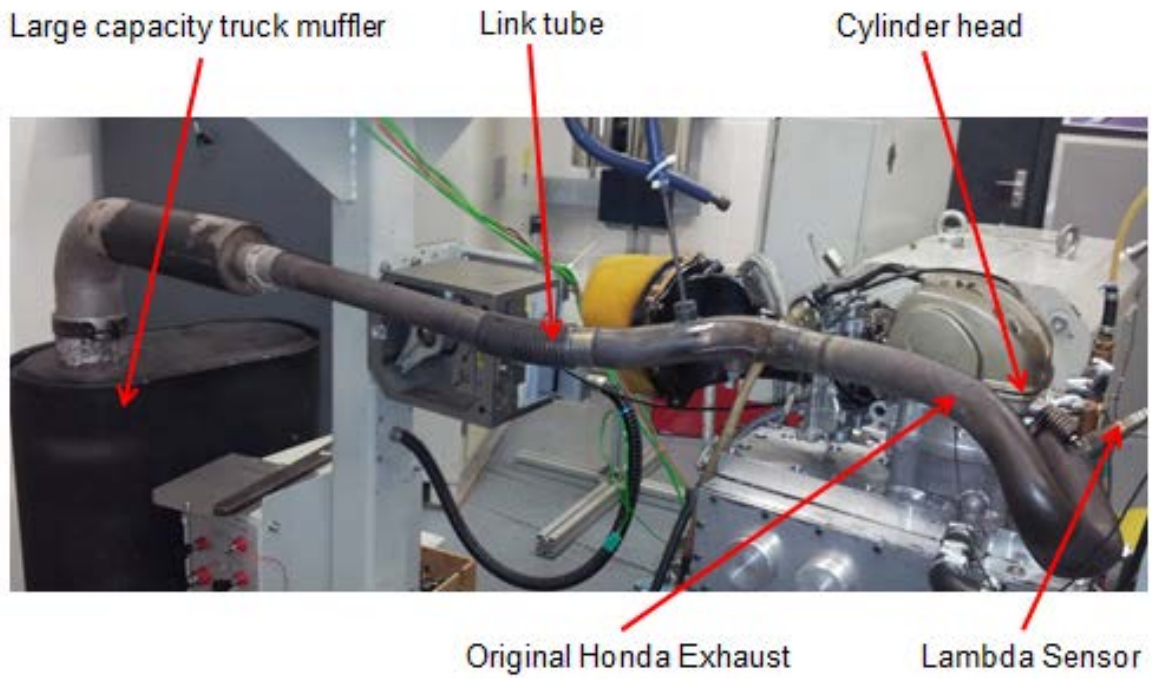

Figure 3.17: Exhaust and extraction system

The throttle is controlled by a standard Shenk remote throttle linked to the Ricardo S3000/3345 system and connected to the carburettor via a standard throttle cable as found on the OEM donor motorbike.

The fuel system used is the same as that found on the OEM motorbike (figure 3.18). In this case the standard fuel tank is mounted above the engine (to one side) and the fuel is run to the engine via standard Honda fuel hoses, an additional fuel filter has been implemented to reduce the probability of solid particle contamination in the fuel reaching the engine. The carburettor was disassembled, set to manufacturers specifications on all adjustments and then all threads and adjustments were locked with the use of a thread-lock. Although a carburettor is not ideal for this type of testing it has been standardised as far as possible to ensure long term consistent operation.

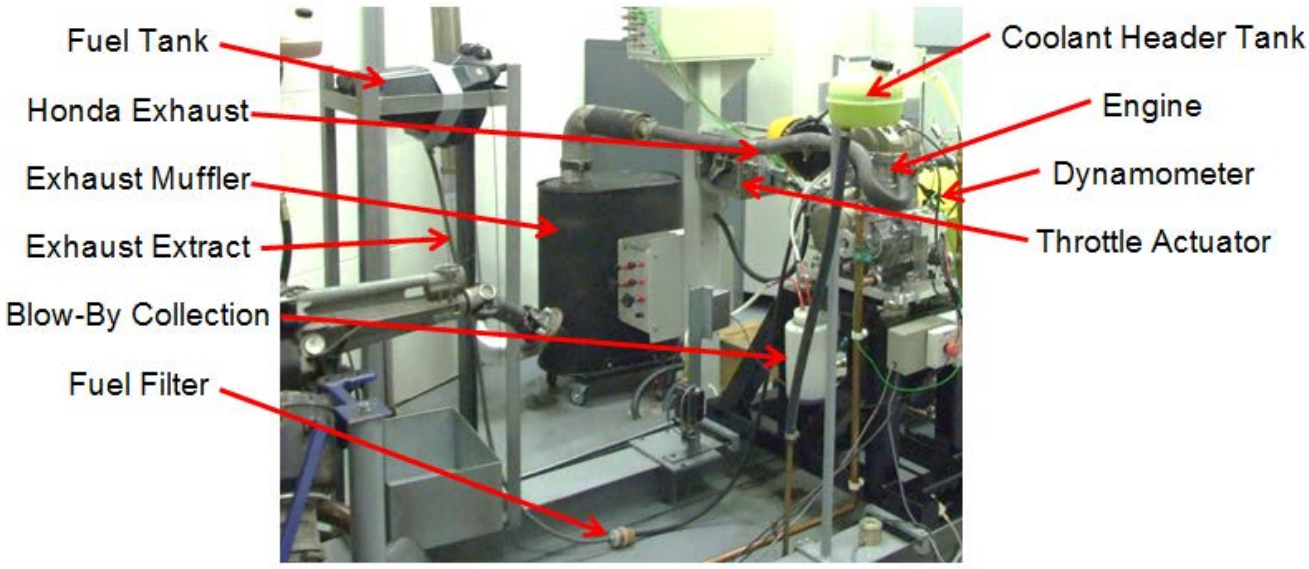

Figure 3.18: The fuel system

The air intake system is completely standard with the OEM bike sponge air filter fitted to the engine and drawing air from the test cell.

The engine is started using the dynamometer, thus the kick-start pedal is removed. The engine is locked in second gear. This gives a cumulative gear ratio of 4.02633. The engine is built to OEM specifications for all tests. Apart from oil tests, it is always run on Castrol 10W40 A3/B3 lubricant in both the engine and gearbox both filled to 80.0% of the maximum permissible level. The rheology of the lubricant is provided in chapter 7, where analytical predictions are carried out.

An emergency stop system was implemented, whereby a solenoid is used to connect the engines magneto to the ignition coil so that in the event of a driveline or dynamometer control failure the ignition can be cut.

3.7 Standard Instrumentation

The instrumentation is classified into two groups in this thesis; the standard instrumentation and the customised instrumentation. The standard instrumentation is concerned with bought-in standard equipment which is used to ensure that the engine is functioning correctly. The customised instrumentation was designed and built for the purpose of this research.

3.7.1 Fuel Monitoring

The fuel system can either be run as a simple motorbike-like system with cell temperature fuel or can go through a palletised fuel unit that is in the test cell, figure 3.19.

Figure 3.19: Palletised fuel system

This is a gravimetric fuel measurement system which incorporates a heater and cooler so that the temperature can be accurately controlled. For the purpose of the testing covered in this thesis the fuel conditioner has not been used as there is no control over the air temperature entering the engine and it is easier to correct for temperature variations when both the air and the fuel are at the same temperature **SAE J1349 (2005).** Fuel consumption is monitored throughout the test on both a flow rate basis with the gravimetric system and also by a mass weighing system of weighing the fuel tank before and after running after the fuel system has been bled and the carburettor filled. This provides a confirmation that the gravimetric system is correctly calibrated.

Fuel temperature is monitored by a k-type thermocouple mounted in a customised fitting that is spliced into the fuel hose, 0.5m away from the carburettor, fig 3.20.

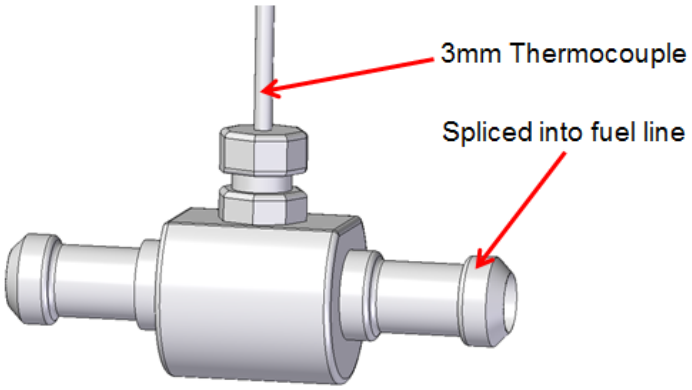

Figure 3.20: Fuel temperature measurement

3.7.2 Air

The air entering the test cell is dried to reduce excessive moisture. The fans removing the air from the test cell are set to a higher volumetric flow rate than the fans blowing air inwards, so that the test cell is always negatively pressurised in order to ensure that exhaust gasses do not leak into to the control room. Apart from this provision, there are no controls over temperature, pressure and humidity. These are all monitored by appropriate sensors and logged throughout all tests so that a rolling correction factor (**SAE J1349, 2005**) can be used.

The air temperature is monitored by a k-type thermocouple mounted on top of the sensor unit in the test cell. This is sufficiently far away from the engine not be affected by its localised heat and is not in the air stream of the cell fans.

The air intake temperature is monitored by a k-type thermocouple inserted onto the centre of the air intake 40 mm away from the mouth of the carburettor as shown in figures 3.21 and 3.22.


Figures. 3.21 and 3.22: Intake air temperature measurement location

Humidity and cell air pressure are measured by the Ricardo S3000/3345 systems internal sensors and allow for live correction of data. Due to the inability to calibrate these sensors a generic weather station is mounted inside the test cell on the window and this is used to ensure that the Ricardo systems is always within specification.

3.7.3 Water

Water temperature is measured with a standard K-type thermocouple at the top hose point, where the coolant exists the engine to the cooling circuit, and at the bottom hose point where the coolant enters the engine from the cooling circuit, as well as in the centre of the liner as close as possible to the liner wall to ensure there is no localised nucleic boiling by ensuring that temperatures are not excessive. The thermocouple is positioned at the sidestroke maximum piston speed position as this should be the hottest part of the liner.

3.7.4 Measurement of Air-Fuel-Ratio (ARF)

Air-fuel-ratio is monitored with the use of an off the shelf Dynojet Wideband 2 logger with LCD display which incorporates a Bosch LSU 4.2 wideband lambda oxygen sensor. This is connected to the Ricardo system so that the ARF is logged throughout the test, but it can be viewed on the PC interface or the Wideband 2 display when the engine is running. The lambda sensor is heated and is installed as

per Bosch and Dynojet instructions into the centre of the gas stream, 100 mm from the cylinder head.

3.7.5 Measurement of Cylinder Pressure

A Kistler 6081A40 Probe with a 3 mm Sensor head, rated to 250bar is installed in the cylinder head in a custom-made stainless steel sleeve. The tip of the sensor is mounted flush with the cylinder head and the sleeve penetrates through the cylinder head's cooling jacket. This means that a water-cooled sensor is not required. This sensor is connected to a Kistler charge amplifier which is in turn connected to a National Instruments data acquisition system.

3.7.6 Measurement of Engine (crank) Position

Engine position is monitored through a custom-made encoder that is mounted to the engines balance shaft (coupled via a gear directly onto the crankshaft), figure 3.23. It comprises a 360 tooth encoder wheel and an optical reader that detects both 360 pulses and a single TDC pulse.

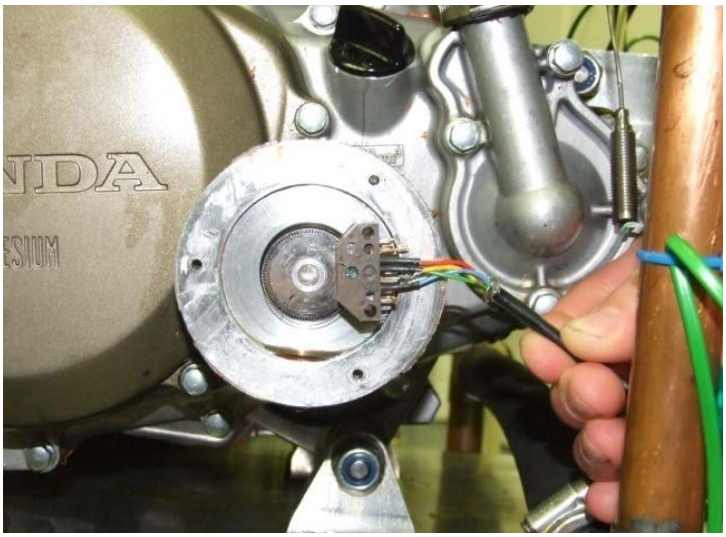

Figure 3.23: Custom encoder mounted to the side of engine

3.7.7 Throttle Position

The built-in Shenk system for throttle control gives a reading of throttle position which is an active feedback device (figure 3.24). This device is calibrated to achieve 0-100% deflection in accordance with the Honda carburettor system. This is achieved by adjusting 0 and 100% stops on the Shenk system, as well as moving the throttle cable connection point up or down a lever to achieve correct linear motion. Once set, all positions are marked and thread-locked. The test procedure includes checks to verify these settings prior to commencement of any test.

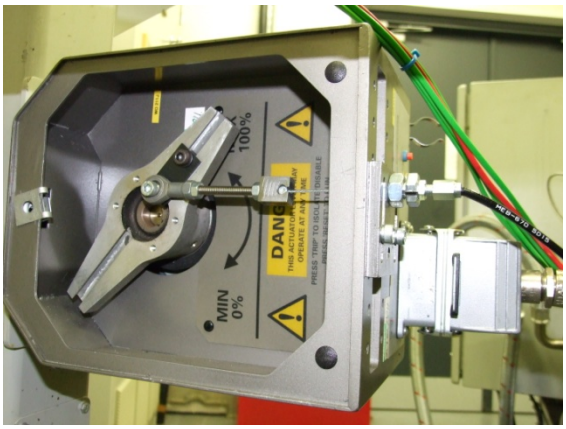

Figure 3.24: Shenk throttle control system (Part of the Ricardo S3000 system)

3.7.8 Engine Speed Monitoring

The engine speed is monitored by a TTL 1024 point encoder manufactured by Hubner Berlin (OG 90 DN 1024 TTL). This is mounted onto the back of the dynamometer and incorporated into the Ricardo monitoring system.

3.7.9 Torque Measurement

Torque is monitored by a load cell incorporated in the dynamometer and connected to the Ricardo system. This is calibrated regularly with a standard hanging weights method.

3.7.10 System Repeatability

Repeatability of test conditions and measurements is a critical factor in the overall research. All tests have to be carried out a number of times with acceptable repeatable outcomes. There should also be controlled conditions so that results of a nominally identical series of tests can be compared with those undertaken under different conditions. This is in order to enumerate changes in friction as the result of deliberating changes in parameters, such as engine speed, motored or fired conditions, etc. Therefore, after implementing standard instrumentation significant effort was placed on understanding the characteristics of the test-bed performance as well as investigating engine stability and sensitivity to parametric changes. The aim is to ensure a highly repeatable setup, coupled with rigorous test procedures which could produce accurate repeatable and most importantly reliable data with a high degree of confidence.

Figure 3.25 shows four corrected power curves run on consecutive days with day to day air temperature variations of 10°C and varying weather conditions, including cell humidity. The results show that the control over the system allows reliable and repeatable measurements within 2% repeatability after appropriate correction factors (**SAE J1349, 2005**) have been applied, this was deemed as the best possible option without humidity control.

A large amount of data concerning air fuel ratio, temperatures, humidity and general running conditions were collected as well as friction data. Friction data is of primary research interest in this thesis so these are presented in chapter 6. All other data are used to either ensure repeatable test conditions or to adjust and or correct for prevalent environmental conditions.

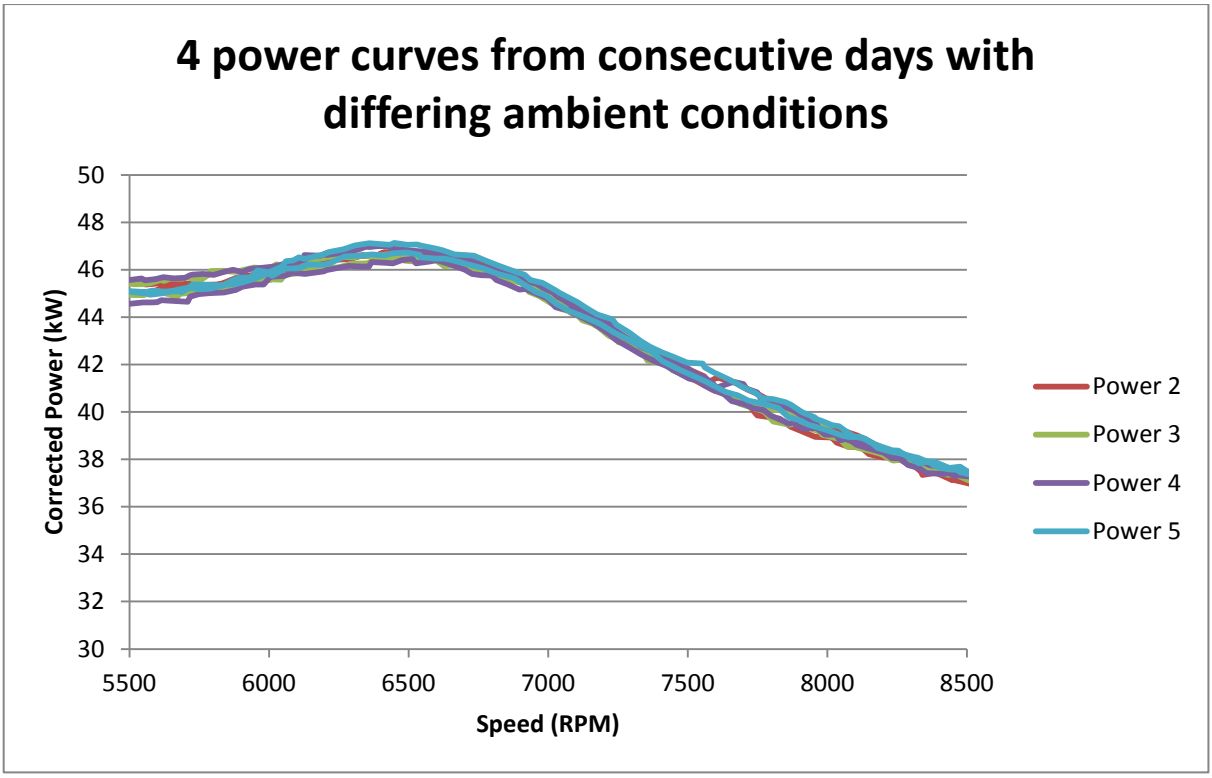

Figure 3.25: Power curve repeatability

Repeatability of test conditions is also essential in the case of other input parameters, such as geometry and topography of nominally identical cylinder liners, pistons and rings. These were undertaken by measurement of all parts with precision metrology (see chapter 5).

The engine was run at a set speed and load and then disassembled. All parts were measured for geometrical and topographical changes in order to determine when pistons, liners and rings were embedded, run-in and worn. This procedure was carried out a number of times with different lubricants and temperatures to determine maximum operation limits.

It was found that pistons, liners and rings are run-in/embedded after only 15 min of running and approximately 80% of this occurs within the first 5 min of operation (see chapter 5).

Chapter 4:

Development of a Floating Liner System for Direct Measurement of Friction

4.1 Introduction

As discussed in section 3.7 two types of instrumentation were employed for engine testing work; standard and customised types. The standard instrumentation used is described in section 3.7. The custom instrumentation comprises the design, development and use of a floating liner for direct measurement of piston-cylinder friction under a variety of operating conditions, described in chapter 6. The advantages of direct *in situ* measurement of friction, using a floating liner, over FMEP are described in the review of literature, section 2.2.

4.2 Measurement of Friction

As discussed in the literature review (section 2.2) there are two main methods of measuring friction of the piston-liner system, which incorporates the contribution of compression ring-liner interface. These are (a) through use of a floating liner and, (b) strain gauged connecting rods and use of FMEP. The former method is the approach undertaken in this thesis and obtains contributions to friction from the various conjunctions under various engine operating conditions directly *in situ*.

Frictional measurement made solely with the floating liner system does not require the use of telemetry or a grasshopper linkage. Measurements using the floating liner are obtained simultaneously with a high speed encoder for accurate reconstruction of transient changes in friction during engine cycles.

4.2.1 Principles of Operation and Mechanical Design of the Floating Liner

The principle of a floating liner device is to suspend the liner in such a way that any point of contact between the liner and any rigidly mounted components are intervened by a number of piezoelectric load cells. Figures 4.1 and 4.2 illustrate an assembly which contains the floating liner, held within a fixture through 3 piezoelectric load cells positioned at 120º spacing. As the piston assembly reciprocates, the applied forces onto the liner cause infinitesimal movements of the liner relative to its rigidly held fixture within the engine cylinder. These forces are measured by the intervening load cells as:

$$\sum f = P - F = R_l - P_r = ma_l \qquad (4.1)$$

where f is the total force, P is the preload, F is the force measured by the load cells, R_l is the load cell reading, P_r is the sensor pre-load, m is the mass of the moving floating liner system and a_l is the acceleration of the moving floating liner system.

The load cells are pre-loaded P_r, whilst *in situ* and at rest, including the weight of the liner itself. This is accomplished by zeroing the sensors in situ with the weight of the system and any pre-load. The preload value is obtained and recorded prior to any testing. The infinitesimal movement of the liner is such that the load cells remain perpetually in compression. In effect the load cells readings, R_l, less their initial measured preload provides the variations in initial inertial dynamics of the liner relative to the holding fixture. This equates to the net applied force, which is due to the pressure load applied to the top rim of the liner and friction, depending on the sense of motion. Friction can thus be obtained. Equation (4.1) assumes pure axial inertial dynamics of the piston, in which the combined load cell readings is R_l. In reality the liner pivots about its midriff brace, in contact with the holding fixture. Thus, the differences in individual readings of the load cells provide the embodied side force and the sense of any small tilt of the liner. These are taken away from the load cell readings to obtain the correct value of R_l in the vertical axial direction. Provisions are made to minimise any tilt of the liner as it is in most part

unconstrained. Design analysis is required to ensure that resonant frequencies or excess deflections are not reached under any intended engine operating condition.

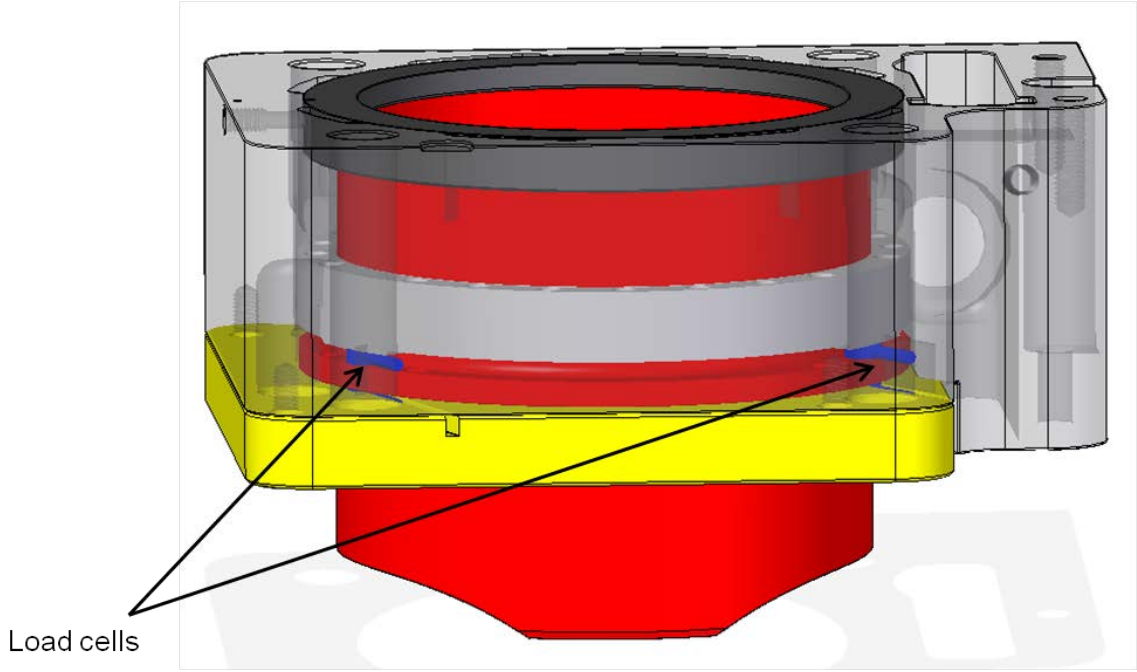

Figure 4.1: A floating liner fitted into its block holder (housing) inserted into the engine block

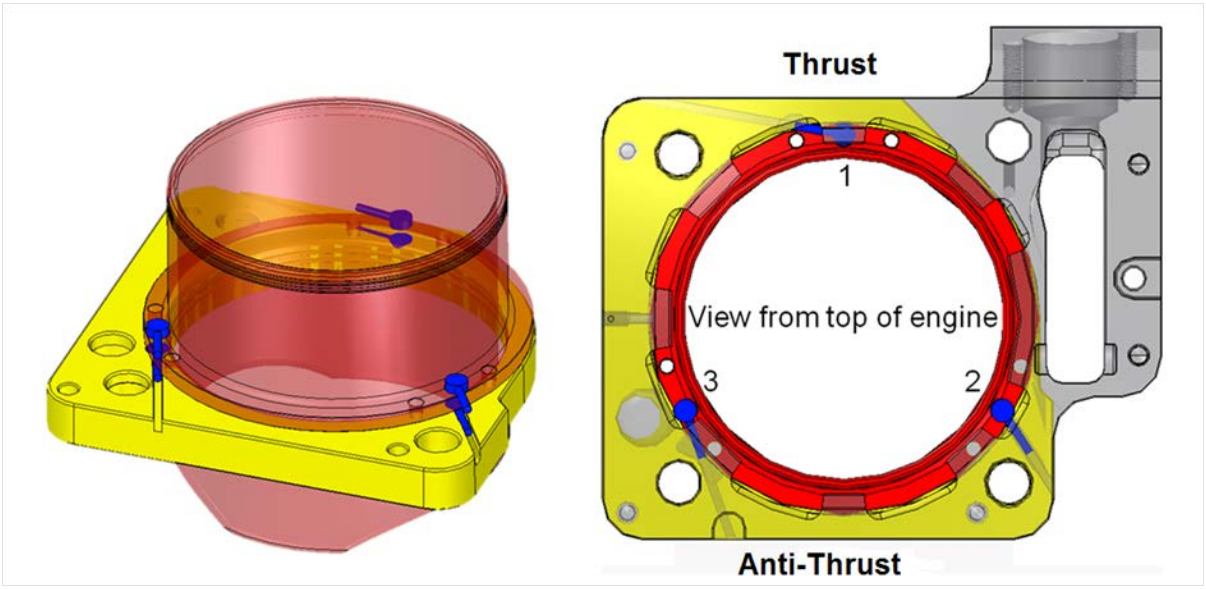

Figure 4.2: Cross-sectional view of the floating liner arrangement

Hence, friction is directly measured as noted by **O'Rourke *et al* (2010).** Care is taken to ensure that the in-cylinder gas pressure acts directly on the liner's top rim periphery only, and is not applied to the holding fixture, for if this were to occur a sharp rise, somewhat mirroring the in-cylinder pressure would result. This would introduce additional non-piston assembly friction forces acting on the load cells. To prevent these spurious in-service readings from the cylinder head clamp loading and unloading due to gas pressure, a labyrinth seal is employed. This allows the de-coupling of the required seal clamping load from the actual liner, thereby allowing quasi-unconstrained infinitesimal vertical displacements.

Figure 4.3 shows the top constrained 20MnV6 alloy steel seal ring (vertically constrained), which is an overhanging precision fit over the floating liner of the same material. The internal diameter intrusion of the alloy steel seal ring requires a stepped piston crown as shown in the figure.

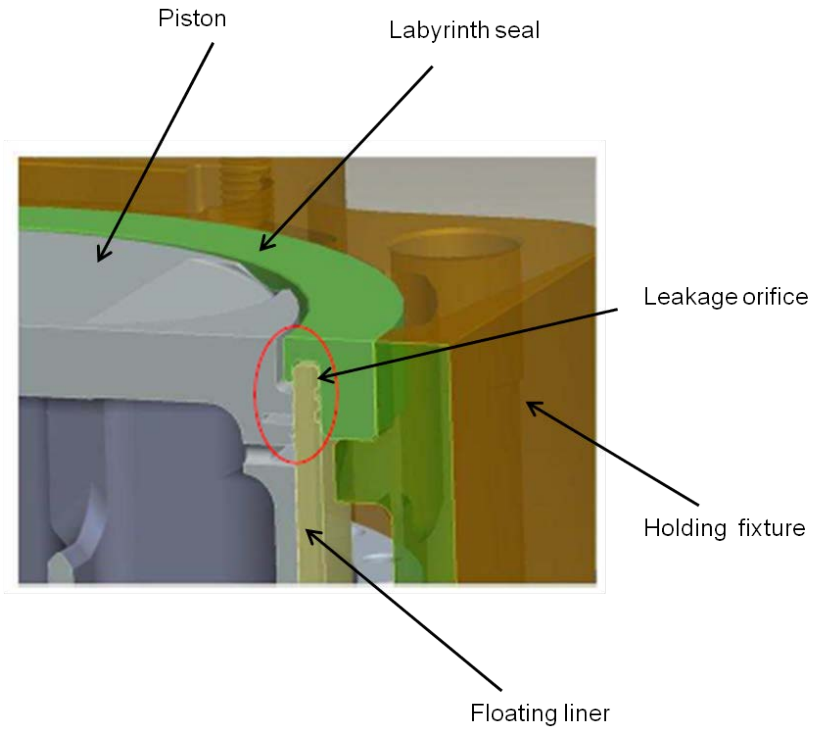

Figure 4.3: The sealing arrangement at the top of the floating liner

Unlike other floating liner arrangements, where a spring-damper arrangement is used to palliate any shock loading of the liner, the use of a labyrinth seal ensures smooth running frictionless operation at the liner top rim, but at the expense of some side leakage of gas through the sealing orifice (gap) as shown in the figure.

The labyrinth seal is incorporated into the design to allow the liner to float but also seal combustion pressure in the combustion chamber. The detail design of the labyrinth seal is provided in by **Howell-Smith (2010)**. Figure 4.3 shows the design chosen, this is very similar to that employed by **Furuhama (1984)** in his floating liner systems. This seal allows decoupling of the liner from the cylinder head and seal, and thereby prevents spurious readings from cylinder head clamping load and deflections due to cylinder pressure. The ring is manufactured from 20MnV6 alloy steel and allows for a 20μm radial gap (cold condition) which allows only small gas leakage through the labyrinth seal system, the outer of the liner is then vented to atmosphere to ensure there is no pressurisation. Coolant ingress is controlled with the use of a Nitrile rubber O-ring in the bottom groove. The ring (green component in fig 4.3) is coated with Apticote® 450F which is a low friction coating containing PTFE which reduces friction of this part on the liner should contact occur.

A miniature Kistler pressure transducer type 6081A is inserted through the gap in order to measure the leakage pressure and apply the correct applied pressure to obtain the liner pressure load as:

$$P = 2\pi r_{min} b(p_c - p_l) \qquad (4.2)$$

where p_c is the combustion pressure and p_l is the leakage pressure. Friction can now be obtained directly from equation (4.1), where *b* is the width of the labyrinth seal and r_{min} is its mean radius.

Due to geometrical constraints the smallest commercially available force transducers were used, these are produced by Kistler AG and the 9131B was selected, specifications are provided in figure 4.4.

Type	Measuring Range F_z [kN]	Overload F_z [kN]	Sensitivity [pC/N]	Rigidity [kN/µm]
9130B...	0 ... 3	3,5	≈–3,5	≈1,0
9131B...	0 ... 2,5	3	≈–4,0	≈0,7

Type	D [mm]	d [mm]	H [mm]	Weight (without cable) m [g]
9130B...	8,0	2,7	3,0	1
9131B...*	7,0	–	3,0	1

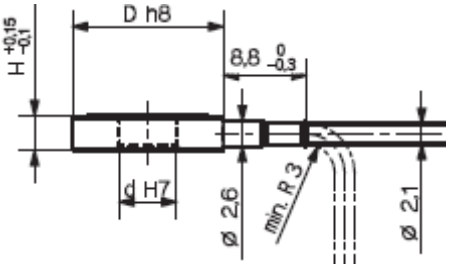

Linearity (preloaded)	%/FSO	≤±1,0
Hysteresis (preloaded)	%/FSO	≤1,0
Response threshold	N	<0,01
Operating temperature range	°C	–20 ... 120
Preloading force (recommended)	F_V	
Direct connection [1]	%/FS	≈50
Shunt mode	%/FS	≈20
Protection rating [2]	EN60529	IP65

Figure 4.4: Kistler 9131B Force transducer specification **(Kistler AG)**

The system was designed with force transducers equally spaced at 120° circumferential spacing as already noted, so that either three or six sensors could be used. Initially the system was constructed with three sensors and an additional three sensors were added after the device demonstrated that it was capable of resolving friction. This approach minimised the cost of the device, but allowed automatic calibration and error diagnostics as the sensor positioning means that the top sensor should always read the exact opposite of the bottom sensor; if this is not true then there is problem which can be immediately investigated. Figure 4.5 shows the sensor arrangement.

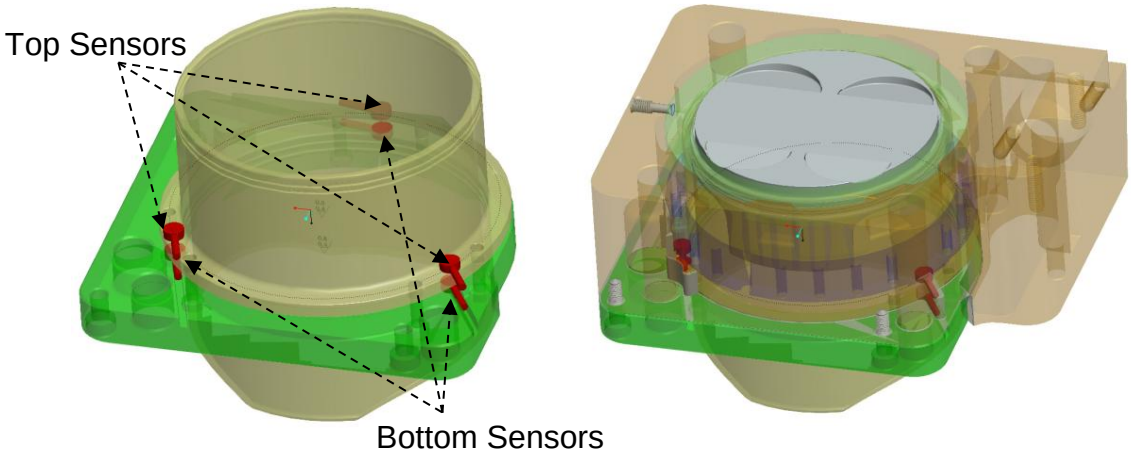

Figure 4.5 Floating liner sensor arrangement

The pairing of the sensors also allows for more accurate calibration of clamping forces which are inherent in the system.

The engine architectural constraints exclude the use of a low elastic modulus light alloy cylinder liner. Furthermore, load cell structural bending limitations and stress concentrations due to the concentrated loads preclude the use of an aluminium alloy. Therefore, 20MnV6 low alloy steel is chosen in the construction of the floating liner.

Analysis showed that a housing material with a coefficient of expansion of 16-18x10^{-6} k^{-1} and a considerably higher yield stress than the standard Honda OEM aluminium cylinder was required and Austenitic stainless steel grade 304 was chosen as it fitted these criteria and is also safe for use with coolant. The piston to steel liner nominal clearance is 100μm.

Modal analysis of the steel liner was performed by **Howell-Smith, (2010)** to check for forcing frequency issues due to engine operation. Maximum engine test speed was set at 9,500 rpm (158Hz) and the liner design work was targeted to be significantly above this value. Two model configurations were used: unconstrained and constrained by 6 points equating to the force transducer pick-up points. Figure 4.6 details the meshed solid used (Left Hand Side), unconstrained configuration mode 7 response (centre) and constrained mode 1 response (Right Hand Side). Table 4.1 details output results from the modal analysis **Howell-Smith, (2010)**.

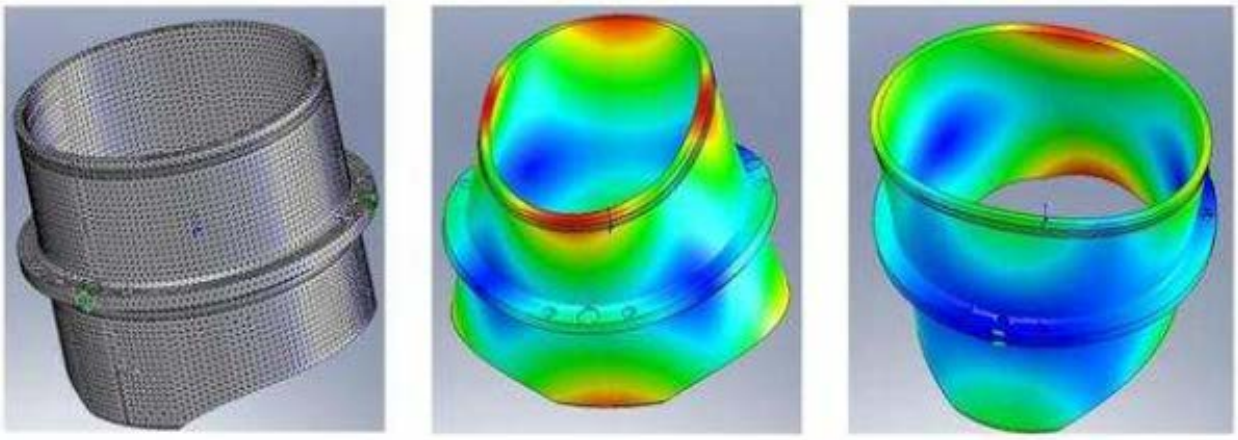

Figure 4.6: Modal analysis of floating liner

Unconstrained configuration results		Constrained configuration results	
Mode No.	Frequency(Hertz)	Mode No.	Frequency(Hertz)
1	0	1	1599
2	0	2	1622.3
3	0	3	2856.2
4	0	4	3097.4
5	0	5	4117.6
6	0	6	4487.4
7	1166	7	4539.9
8	1181.8	8	4895.5
9	1383.2	9	5021.7
10	1388.3	10	5127

Table 4.1: Modal analysis tabulated results

4.2.2 Load Cells and Signal Processing System

The load cells (described in figure 4.4) are either arranged singularly or in pairs to measure the vertical axial inertial dynamics of the floating liner, which equates to the net force, comprising the measured pressure loading and friction (equation (4.1). The load cells are connected to Kistler charge amplifiers 5073A311 which can accept up to three inputs (figure 4.7). Therefore, either one or two are used depending on if both top and bottom or bottom only sensors are used. These amplifiers convert the charge output of the load cells and convert them into a voltage output that can be interpreted by a National Instruments data acquisition system. The encoder and in-cylinder pressure transducer signals are also fed through to the National Instruments system to ensure there are no phase errors.

The National Instruments NI PXI-1031 data acquisition system runs a custom lab view code written specifically for this application. It logs the force transducer input at a rate of 200,000hz and uses a digital counter to log the encoder position. At the end of each log it matches up the nearest force measurement point with the exact encoder position and produces a file that has the force logged on a crank-angle basis. This makes processing the data significantly easier due to the single cylinder

nature of the engine. All six force transducers as well as in-cylinder, crankcase and labyrinth seal pressures are logged on this system (only 2 pressures can be logged simultaneously due to the limitation of 8 analogue inputs through the patch panel)

(1) (2) (3) (4)

1) Kistler 9131B21 Slimline 2.5kN force sensor
2) Kistler ICAM programmable industrial charge amplifier (3-input)
3) National Instruments BNC-2110 8 channel patch panel
4) National Instruments NI PXI-1031 data acquisition computer

Figure 4.7 Components used in the data acquisition system

4.3 The Calibration Procedure

Calibration is performed in three stages. The first stage involves application of static weights onto the sensors in order to ensure their functionality before assembling the floating liner system. The second stage is carried out after assembling the floating liner and applying static loads, equally distributed onto the top of the liner without the labyrinth seal in place. This is depicted in figure 4.8.

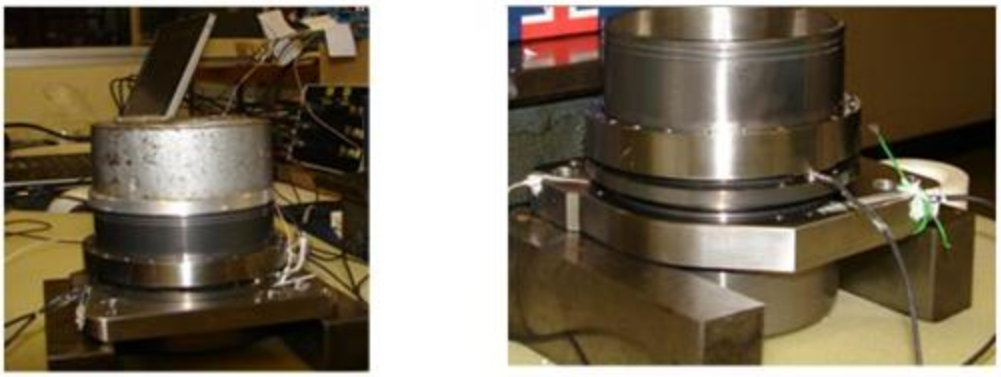

Figure 4.8 Calibration of floating liner and charge amplifier set-up

The third and final calibration stage is conducted after the floating liner is *in situ* in the engine cylinder. Weights are applied to the top of the liner with the labyrinth seal removed. Correction to the amplifier setup is only performed at the second stage of calibration, which is conducted in the metrology laboratory on an accurate flat platform and with controlled temperature and humidity conditions. The first and third calibrations are performed only to check the system functionality and to ensure there is no build up error. Figure 4.9 shows calibration at stage two showing all three sensors reading the same nominal value.

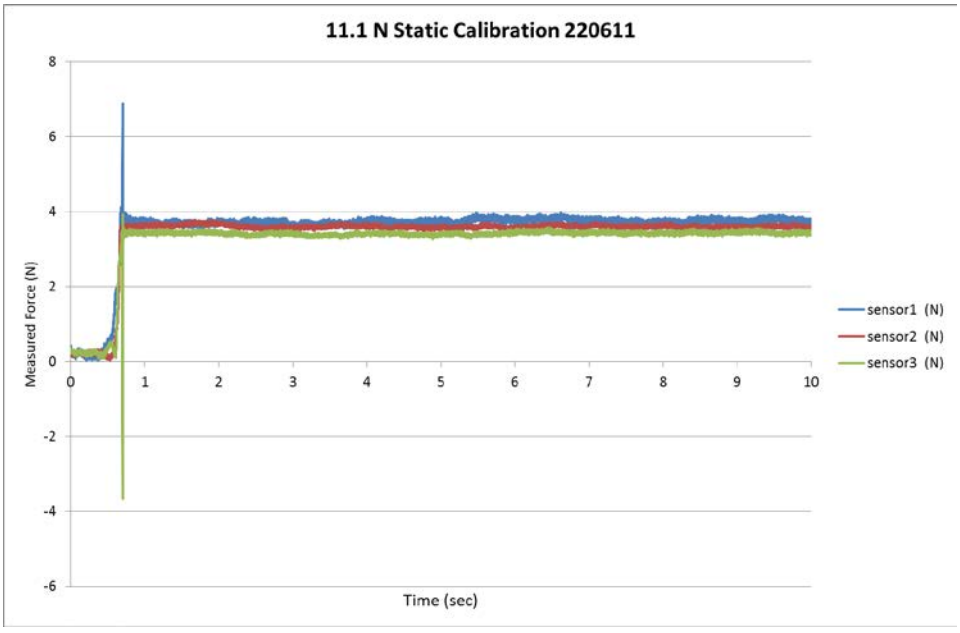

Figure 4.9 Stage-two calibration

After vertical calibration is complete a radial calibration is conducted to ensure that the sensors are balanced. This is done by simply pushing the liner along the thrust and anti-thrust axis along the liner. The corresponding output of the three sensors should equal zero. This is shown in figure 4.10.

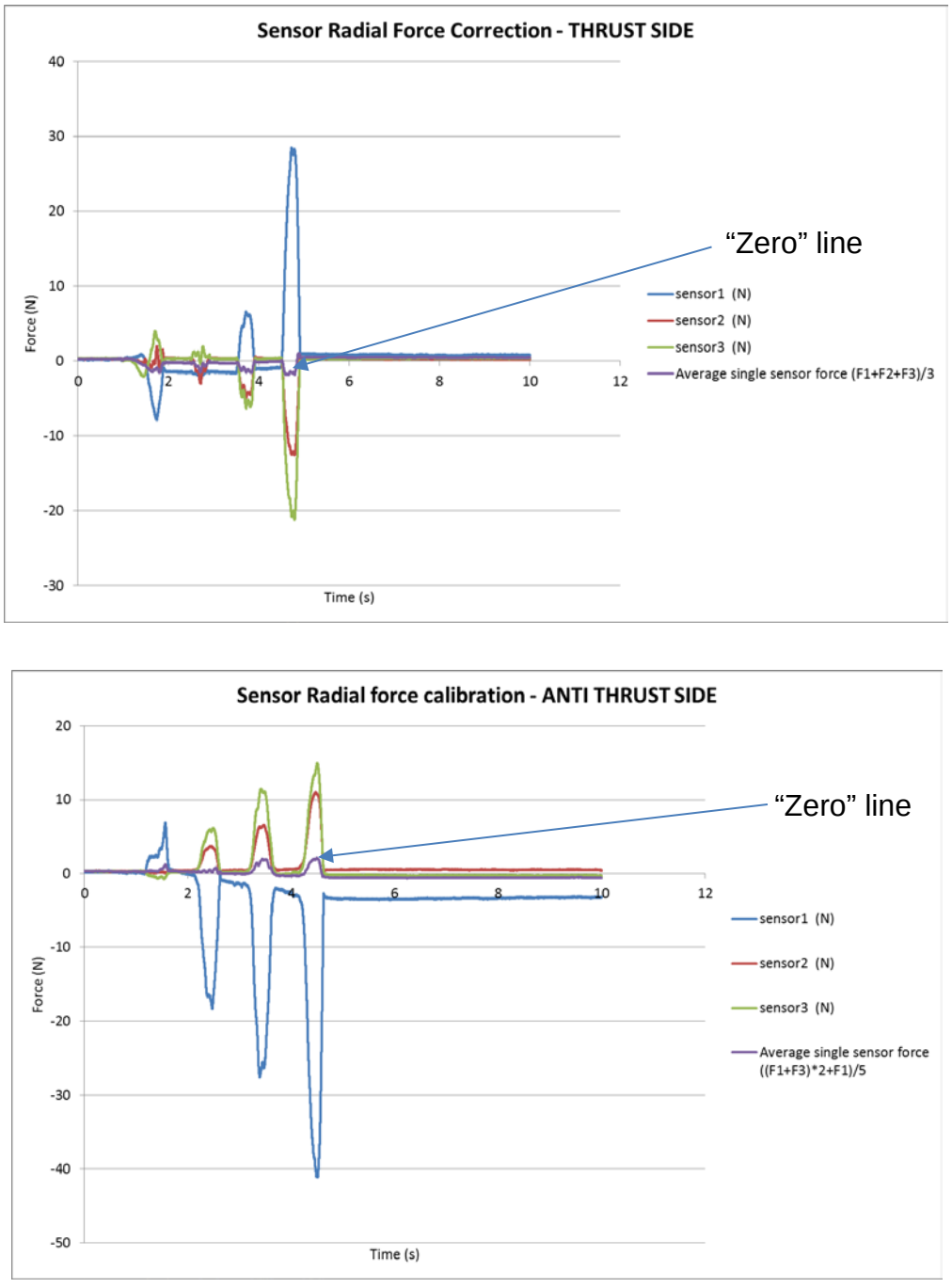

Figure 4.10 Radial calibration

Note the average lines in figure 4.10 are not perfectly zero due to the loading not being directly in at 90° to the piston direction as load was applied by pressing inside the liner.

After radial calibration shows that the sensors are balanced the engine was then motored at low speed (200 rpm) in both forward and reverse to show that the calibration is correctly functioning. This is shown in figure 4.11. Note the two lines do not line up due to piston offset.

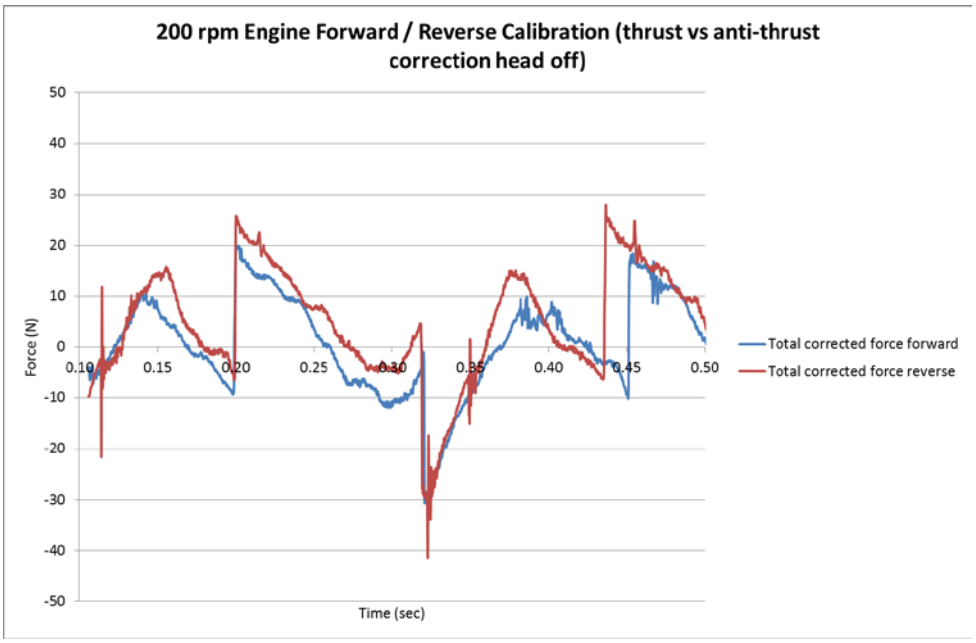

Figure 4.11 Forward vs Reverse calibration

4.4- Closure

The instrumented floating liner together with the standard instrumentation (described in chapter 3) are used in the engine testing procedures highlighted in chapter 6. Engine test results are also provided in chapter 6. Chapter 5 describes the surface topography of the sliding surfaces and their wear characteristics. These are important parameters, together with wear characteristics in order to ensure testing repeatability as well as the use of appropriate topographical parameters for analytical predictions in chapter 7.

Chapter 5:

Determination of Surface Topography and Wear

5.1 Introduction

Determination of the surface topography and wear characteristics of the cylinder liners tested in the current research is important for several reasons.

Firstly, as discussed in chapters 1 and 2 and shown in chapter 6, the regime of lubrication in the piston-cylinder conjunctions (skirt and the ring-pack) is transient and includes hydrodynamic, mixed and boundary conditions. Consequently, some of the generated friction is due to direct interaction of surfaces. Boundary lubrication is affected by surface topography of the contacting solids as well as their mechanical properties (as shown in chapter 7 by the **Greenwood and Tripp (1971)** model). Therefore, the gradual wear of the surfaces alters the boundary friction contribution. The process of wear itself comprises firstly of an initial run-in wear as well as a longer period of gradual wear leading to a final embedded condition. Therefore, it is necessary to understand this process for all liners, pistons and rings used in the investigation in order to ensure, as far as possible, repeatability in the tests reported in chapter 6.

Secondly, topographical data is required for the predictive numerical work carried out in chapter 7, in order for the combined numerical-experimental approach undertaken in this thesis to bear reliable conclusions.

Thirdly, as noted in chapter 4, the cylinder liner/bore is in reality out-of-round. This reduces the conformity of the skirt-liner and rings'-liner conjunctions and can lead to changes in frictional characteristics which are not often accounted for in numerical analysis. Therefore, measurement of liner radial out-of-roundness and axial asymmetry are needed for a comprehensive numerical analysis. The analysis in chapter 7 is for the case of compression ring-bore contact and it is one dimensional in the direction of ring face-width, because the emphasis in this thesis is put on monitoring experimental conditions. Furthermore, the analysis in chapter 7 is carried out for the case of the steel floating liner with Ni-SiC coating. These liners show good geometrical conformance to a right circular cylindrical geometry, but they are quite unlike the wet barrel aluminium liners used as inserts in the modified Honda CRF450R where the effort in numerical analysis by other members of the research team was concentrated. Consequently, their wear characteristics were evaluated as a part of this thesis, which also sheds light on longer term performance of the liners as well as the short period frictional behaviour of the floating liner. In this manner the effect of the wear process on the frictional characteristics can be surmised and ideally related to the surface topographical measures.

5.2 Brief Introduction to Statistical Topographical Measures

Engineering surfaces, like all natural surfaces, are rough. They comprise of many features; peaks and troughs of various scales. They include surface waviness, typically of several micrometres or larger, as well as roughness, which is considered to be significantly smaller than the contact dimensions and the nominally lubricated conjunctional gap. These features are of the order of a few tenths of micrometres in height. Of course, as **Gohar and Rahnejat (2008)** explain on all micro-scale roughness features many other smaller features reside in the nano-scale. Therefore, when measuring the surface topography the measurement resolution is a function of the instrumentation used.

There are many such instruments available which are suited to the level of resolution required, including non-contacting white light interferometry systems with z-direction resolutions typically in the nano-scale and scanning areas of several square micrometres. These devices include Zygo and infinite-focus microscopes such as Alicona. Even further down the scale surface topography may be measured in terms of fractals, which constituting a minute patch which when reconstructed lead to nano-scale surface roughness measures. Atomic Force Microscopes (AFM) may be employed for this purpose.

For the purpose of this wear research a contact measurement technique had to be chosen due to the nature of a closed cylinder liner. In order to use an optical technique the liners would need to be cut into strips so that they could be put under the lens of the measurement machine. After cutting strips from a liner the liner can no longer be run in the engine so this is not feasible. Some devices can be used with mirrors or extension tubes. However, these were not available for this research and a high precision contact measurement technique provided more than adequate resolution.

A Taylor Hobson precision PGI 1250 Aspheric mould measurement system using a 2µm stylus tip 155-P54469 was used for the measurement of the liners. This machine had a resolution of 0.8nm and is a contact type surface measurement device as shown in figure 5.1. It is based on a small stylus that traces the surface and generates a line plot representation. Two types of such device are available; skidless and skidded, as shown in figure 5.1, with the latter measuring the surface relative to a reference surface. A skidless system was used so that the curvature could be removed through software after measurement and for higher accuracy. With the stylus type devices, the lateral resolution is related to the size of the stylus tip itself **Gohar and Rahnejat (2008).** This means that features which are smaller than the stylus tip are undetected in the scan of the surface and thus do not feature in the evaluated statistical surface parameters, such as the average surface roughness, known as R_a (figure 5.2).

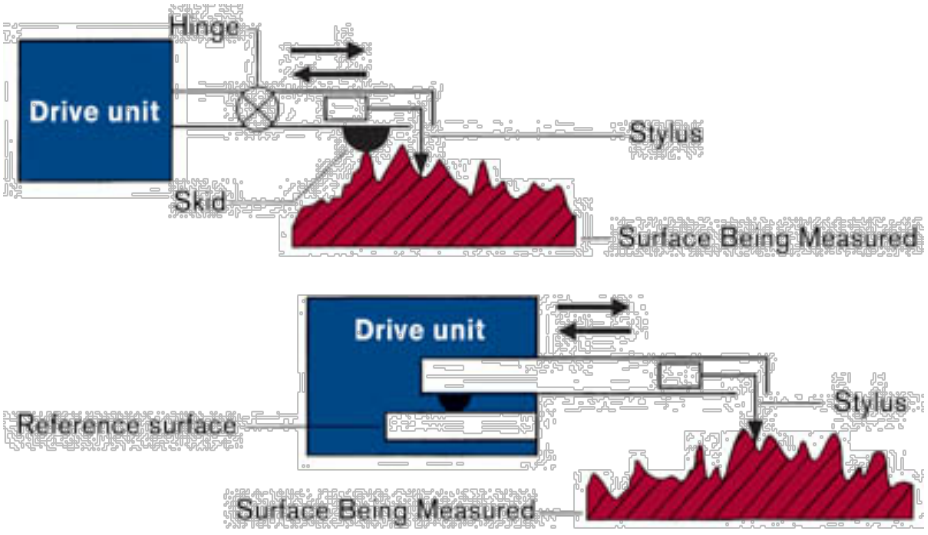

Fig 5.1: The principle of operation for contact measurement devices

As shown in figure 5.3, Ra is not a very good measure of many surfaces, particularly as it does not fully represent the “peakiness” of a surface (R_p) or any deep groove/valleys (R_v). In other words. It does not distinguish between two surfaces which may have a similar average roughness, but quite distinctly different peak-to-valley height variations.

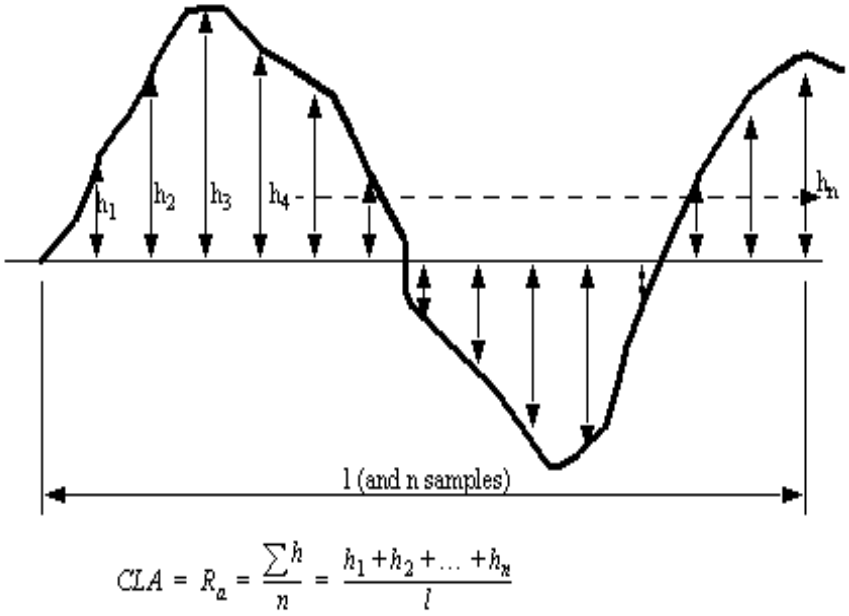

Fig 5.2: Average surface roughness, R_a

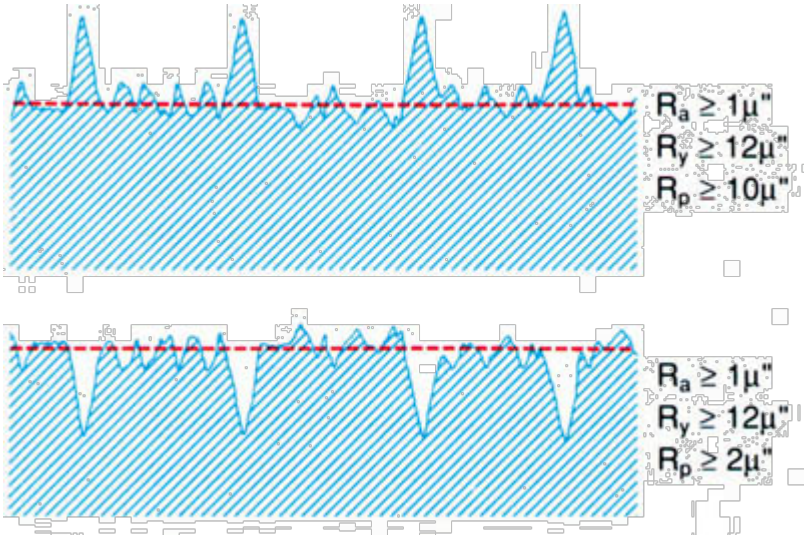

Figure 5.3: Two distinct surfaces with same value of R_a

It should be noted that cylinder liner surfaces are quite rough pre fitment into the cylinder bore. After fitting, an in situ cross-hatch honing process is carried out. This process renders a plateau form topography with hatching marks according to the tool used at an angle to the horizontal (orthogonal to the cylinder liner vertical axis). Cross-hatching creates plateaus of diamond shape surrounded by valleys which act as reservoirs for lubricant, when in operation. A thinner film forms on the plateau surface which would most likely affect the regime of lubrication. The depth of the valleys should be much larger than the topographical surface roughness on the plateau. Some researchers, for example **Spencer et al (2011)** and **Michail and Barber (1995)** have suggested that special film shape functions have to be determined in order to study the lubrication of cross-hatched surfaces and that the usual statistical surface parameters are not suitable for inclusion in the analytical methods, such as that described in chapter 7 for the case of **Greenwood and Tripp (1971)** model. The model, is argued, to best suit to polished surfaces where a Gaussian-type asperity distribution may be assumed, a principle which underlies its derivation. In this thesis it is assumed that the contact conjunction is between the diamond shaped plateau regions and the piston or ring-pack and that the valleys created by the cross-hatching only improve the lubricant availability to ensure sufficient flooded conjunctions. Their contribution to friction is thus negligible. To

show this, it is essential to demonstrate through engine testing and in-process wear of topography that the depth of valleys remains unaltered.

It is also quite clear that R_a values cannot be a reasonable representation of cross-hatched honed surfaces. Specific surface parameters are required to determine the height of the plateau, the "peakiness" of the surface standing proud of the plateau and the average depth of the valleys. Figure 5.4 shows the basic principles behind 3 key surface statistical parameters used in order to define such a surface. They include the average height of the plateau, defined by R_k, the average "peakiness" of the surface above the plateau, R_{pk} and that of the valleys below the plateau R_{vk}.

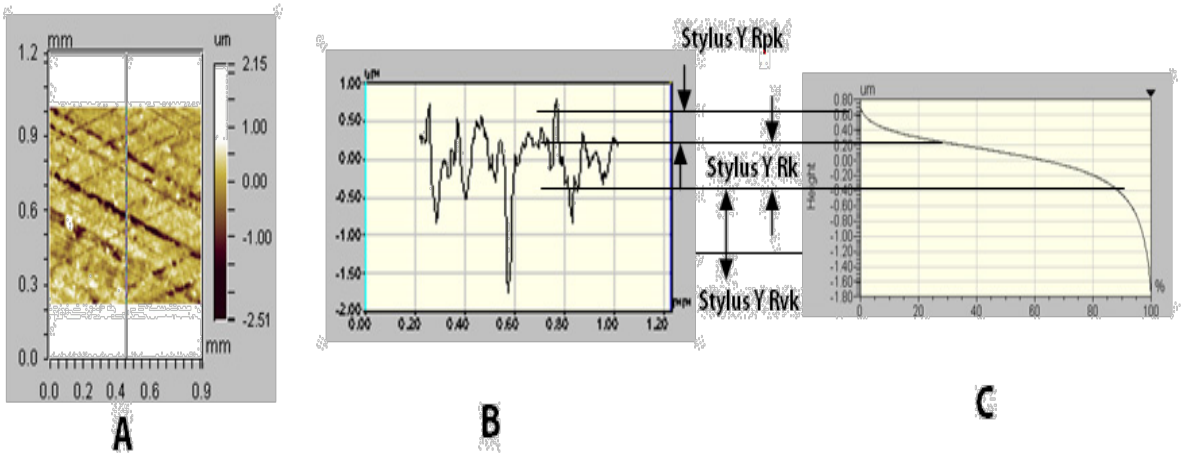

A - Line trace across the cross-hatch geometry

B- The signal trace,

C- Result of statistical analysis

Figure 5.4: Determination of surface parameters R_k, R_{pk} and R_{vk}

Figure 5.5 shows how these parameters are defined. Note that R_k is obtained by using the slope of the plateau. R_{pk} is the height of the peaks above this plateau and R_{vk}, the depth of the valley. The proportional area of the trace occupied by the plateau peaks and the groove/valley are also shown in the figure. Clearly, only a small proportion of the area on the plateau is usually occupied by roughness peaks. However, as **Gohar and Rahnejat (2008)** have shown a very small percentage of

asperity peaks can significantly increase friction. This may be reduced during the running-in period. Therefore, it may be surmised that during the process of running-in wear the correct topographical measure for evaluation of friction would be R_{pk}, whereas during subsequent gradual wear the correct topographical measure would be R_k. The significance of R_{vk} on friction would only be in holding a reservoir of lubricant which can be entrained into the contact conjunctions formed on the diamond shape plateaus, unless the wear process completely removes the plateau itself. In such a case, it is expected that a larger clearance than that designed would emerge and the liner may be considered as having reached the end of its useful life.

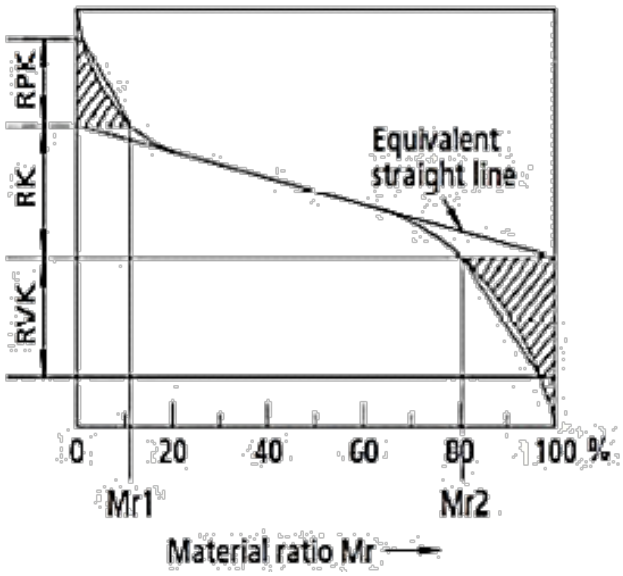

Figure 5.5: Definition of plateau surface parameters

5.3 Wear Characteristics of Cross-Hatch Honed Liners

It is necessary to determine the wear characteristics of cross-hatch honed liners used in this project on a number of counts.

Firstly, it is important to ascertain the validity of the assumption made in the preceding section that the wear process from an initial running-in period to gradual wear and embedding renders a topography that can be characterised by statistical

surface roughness parameters. This means that specific surface parameters should be used in numerical/analytical predictions which represent the state of surfaces accurately according to the state of wear.

Secondly, it is necessary to justify the assumption made that valleys created by the usual cross-hatch honing process remain almost unaffected during the initial and gradual wear processes. This means that unlike the suggestion made by other research workers in the field ((**Spencer et al, 2011** and **Michail and Barber, 1995**), no special film shape provision is necessary for representation of the plateau regions.

Wear, particularly its steady state phase post the running-in phase is a very slow process if no untoward conditions arise. Therefore, to evaluate the wear performance of a surface requires means of an accelerated process. Fortunately, a procedure under firing engine conditions has been devised by Capricorn Automotive, which is the supplier of the cylinder liner variants used in the current research to the racing fraternity. The procedure employed is depicted in figure 5.6 and table 5.1, adopted for the Honda CRF450R motocross motorbike engine used in this thesis.

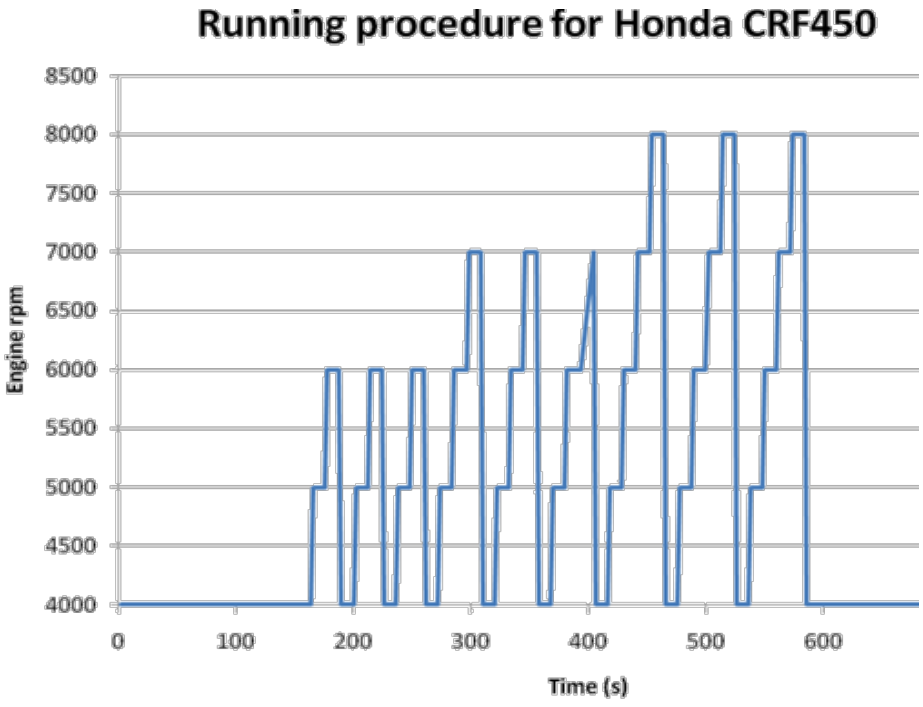

Figure 5.6: The engine testing procedure for liner wear study

Time (sec)	Speed (rpm)	Throttle (%)
150	4000	25
10	4000	50
10	5000	50
10	6000	50
10	4000	50
10	5000	50
10	6000	50
10	4000	50
10	5000	50
10	6000	50
10	4000	75
10	5000	75
10	6000	75
10	7000	75
10	4000	75
10	5000	75
10	6000	75
10	7000	75
10	4000	75
10	5000	75
10	6000	75
10	7000	75
10	4000	100
10	5000	100
10	6000	100
10	7000	100
10	8000	100
10	4000	100
10	5000	100
10	6000	100
10	7000	100
10	8000	100
10	4000	100
10	5000	100
10	6000	100
10	7000	100
10	8000	100
150	4000	25

Table 5.1: Engine test condition corresponding to figure 5.6

The test conditions illustrated in figure 5.6 and detailed in table 5.1 represent accelerated wear tests that lead to a fully embedded liner at its culmination. The engine tests were carried out on the test-bed described in chapter 4. A repeatable combined test and surface measurement procedure was followed, both with a base lubricant (without any additives) and BP Castrol's usual grade fully blended SAE 10W40-A3/B3 oil. The reason for the choice of the base and fully blended lubricant was that oil-surface combination is very important issue. As **Erdemir (2005)** has observed tribology should be viewed as a lubricant–surface system. The fully formulated lubricant enjoys boundary active elements such as a small percentage of long chain polymeric molecules that adsorb onto the surfaces and form a thin low shear strength boundary. These alter the boundary friction contribution and are traditionally represented by the Eyring shear stress of the lubricant in the **Greenwood and Tripp (1971)** model (chapter 7). It was necessary to note the effect of this low shear strength film as additional information for the analytical work in chapter 7.

Prior to any testing the cylinder liner topography was measured and all surface parameters of interest, as highlighted above were recorded. The engine running-in schedule is shown in Figure 5.6. The test intervals were 11 min periods, commencing with a minimum speed of 4000 rpm, rising to a maximum of 8000 rpm, and from application of 25% throttle to maximum power (table 5.1).

All the surface parameters were obtained within specified regions of the tested liners. Measurements were taken from the thrust side, anti-thrust side and one neutral side, on each of these sides 6 line measurements were taken as shown in figure 5.7, therefore an overall total of 18 line traces were taken per cycle. The 18 lines which include max piston speed and reversal positions were all averaged to give the presented results. The liners were placed into a specially designed rig to ensure flatness of the liner relative to the stylus and to achieve within reasonable repeatability the various regions measured repetitively during the testing procedure. The device used was a Taylor Hobson model PGI 1250 Aspheric mould measurement system using a 2µm stylus tip 155-P54469 system with a resolution of

0.8µm. The set up including a liner, the holding jig and the overall machine is shown in figure 5.8 and figure 5.9.

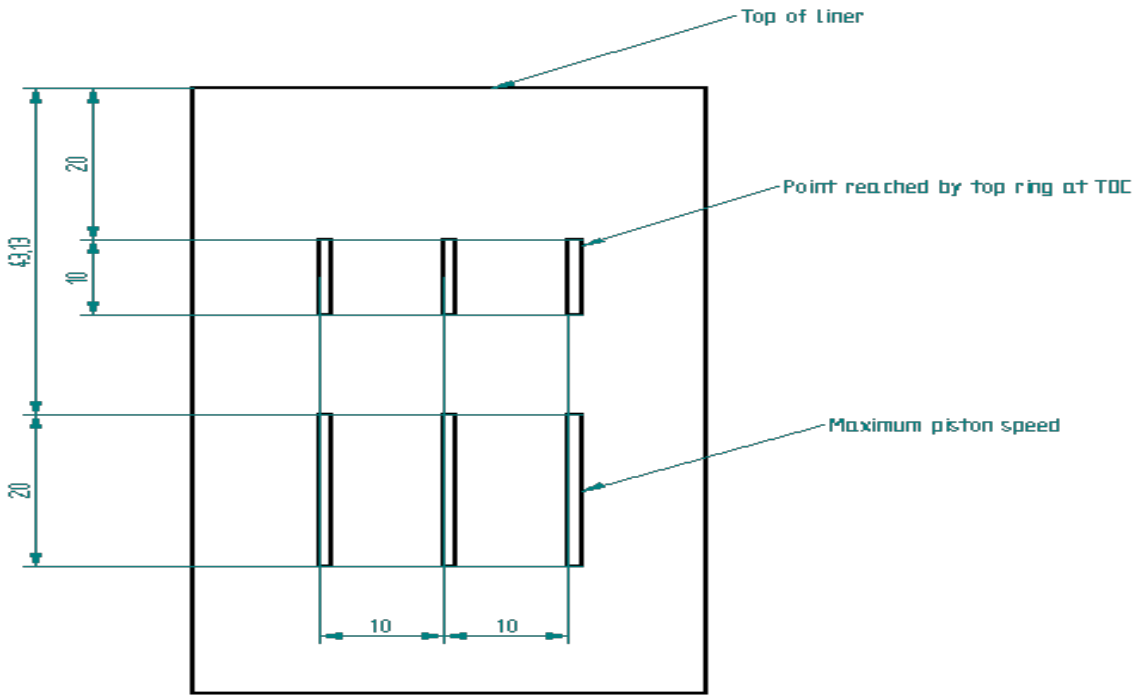

Figure 5.7: Regions of measurement of liner surface topography

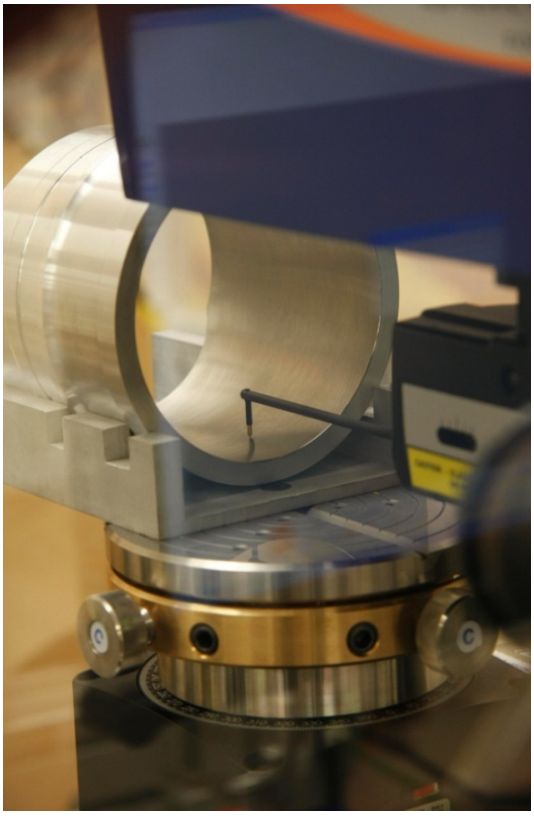

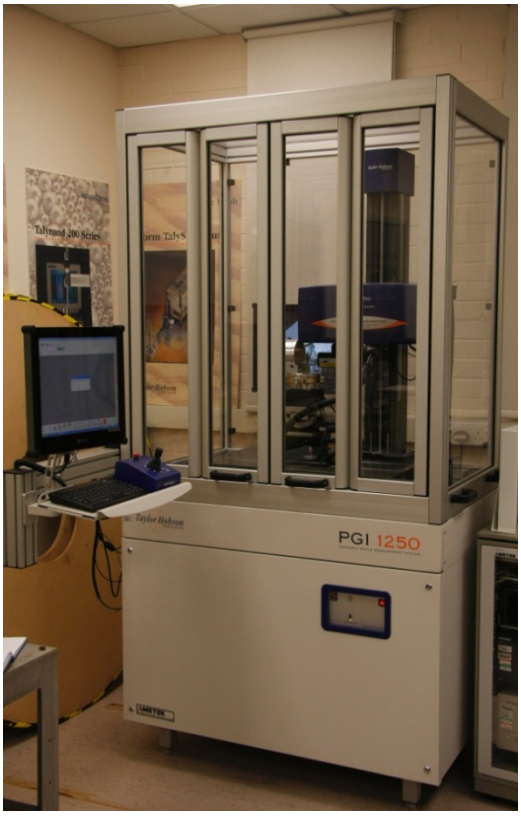

Figure 5.8 + 5.9: PGI 1250 Aspheric mould measurement system with cylinder liner insert and the measuring stylus

After the first 11 min running period the lubricant was drained and replaced with clean lubricant. Thereupon, the same lubricant volume was maintained in all subsequent runs. The surface roughness parameters were obtained at the end of each four consecutive engine running periods with the base oil and at the end of each of five consecutive running periods with the SAE 10W40-A3/B3 oil. At the end of each running period the engine was dismantled and the liner was removed and measured as shown in figures 5.8 and 5.9. It should be noted that a fully embedded (run-in) ring pack and piston was used for all these tests in order to eliminate the effect of the counterfaces on the wear characteristics of the liners used.

As expected the results obtained for changes in the surface roughness R_a showed no appreciable change. However, the more pertinent surface roughness parameter R_{pk} showed rapid reduction in its value as shown in figure 5.10 for both cases of

base oil and the fully formulated lubricant. Note that the value of R_{pk} quickly settles down after a rapid period of wear within the first few minutes of testing procedure. This is in line with the expectation that peaks protruding above the plateau are rapidly removed within a number of engine cycles. In both cases with base oil or the fully formulated oil the R_{pk} value is reduced to half its original value, but at a slightly faster rate with the base oil which does not afford the surface of the protection of boundary active molecular species. The error bars in the figures indicate the spread of results for the many nominally similar liner surfaces tested in this manner.

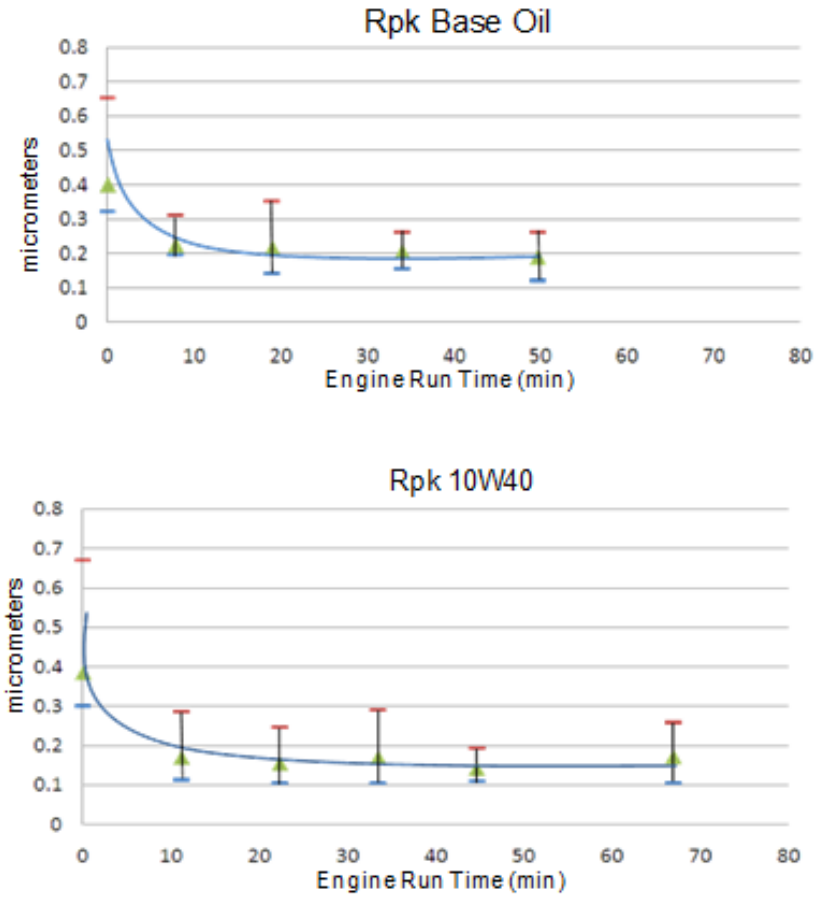

Figure 5.10: Changes in surface "peakiness" parameter R_{pk} during the running-in wear phase

After the initial run-in period, as shown in the figure, the value of R_{pk} hardly alters. This means that for analysis pertaining to embedded surfaces and under steady

state conditions, the appropriate measure of wear performance would be the plateau roughness rather than the evolving value of R_{pk}. This parameter is, of course, R_k.

The depth of valleys is indicated by the parameter R_{vk}. Its variation during testing intervals is shown in figure 5.11. It is clear that no appreciable change can be noted with either lubricant for the R_{vk} from its initial value. This confirms the initial hypothesis that the depth of valleys would remain unaltered irrespective of fairly severe accelerated wear conditions.

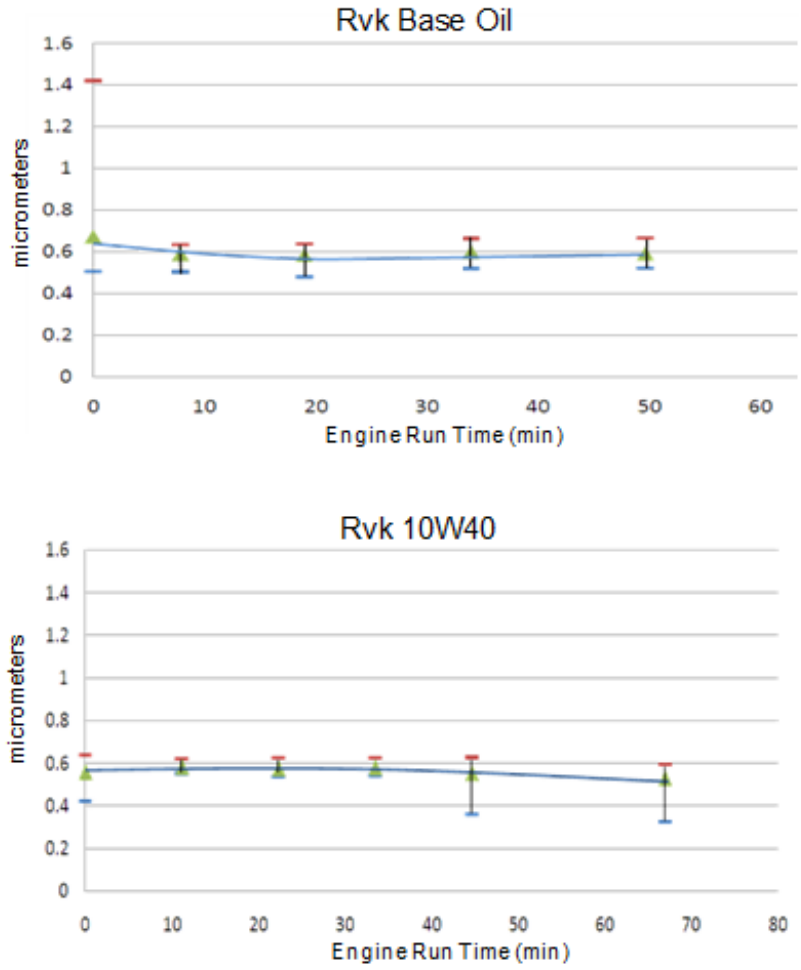

Figure 5.11: The unaffected R_{vk} parameter through severe accelerated wear in a fired engine

Whilst R_{pk} shows formation of a run-in plateau, the same is not true of the overall plateau height, R_k (figure 5.12). This means that R_k is a good measure of the gradual wear phase, post the initial run-in phase. It is this gradual wear and embedding process, which eventually over many cycles of engine result in functional deterioration of the liner (its useful life). Of course emerging clearances and loss of coating protection on the rings occur ahead of this eventuality. Again the sharper gradual wear rate with the use of base oil is evident.

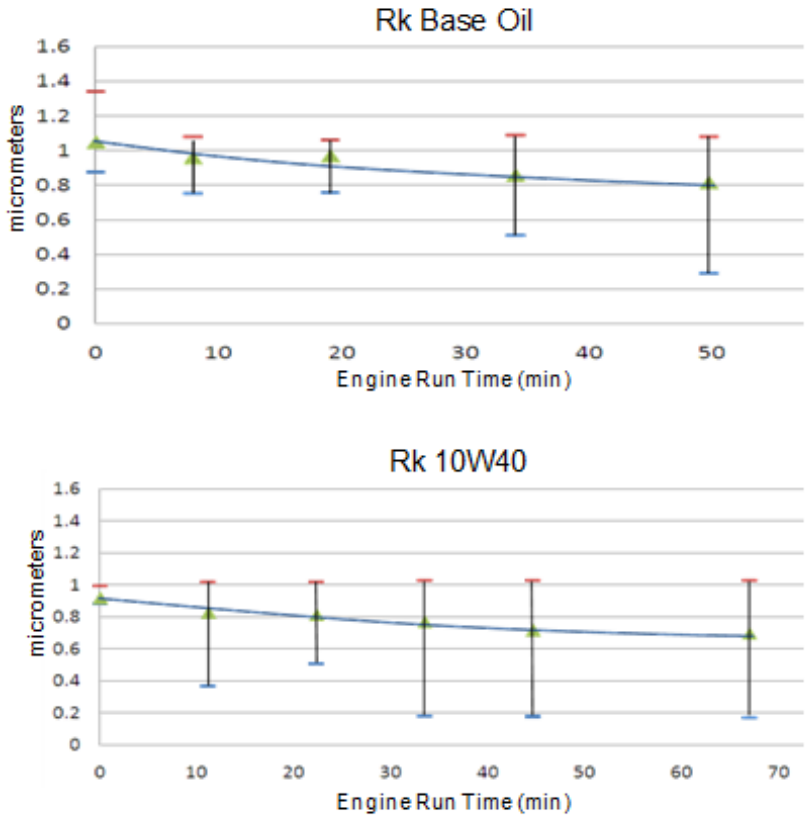

Figure 5.12: Gradual wear phase noted by the R_k value

5.4 Closure

A number of key conclusions can be made as the result of investigations reported in this chapter.

Firstly, with careful and precise measurement of topography the evolving process of wear can be represented by correct choice of surface parameters. During the running-in phase of wear, for plateau honed liners, R_{pk} (the “peakiness” parameter) may be used to reasonably determine the instance that a liner can be deemed to be run-in. Prior to this period any numerical analysis should use R_{pk} value for any predictive boundary friction model. Then after, a good measure of gradual wear and surface embedding is the platform height as given by the R_k value. This finding is used for subsequent test procedures with the floating liner in chapter 6. Clearly, it makes a part of testing repeatability which also includes surface temperatures, lubricant, fuel and coolant temperatures as well as test cell environmental conditions; temperature and humidity.

Secondly, it can be surmised that the role of grooves/valleys formed through cross-hatch honing is in acting as reservoirs of lubricant and as micro-wedges in the entrainment of lubricant into the contacting plateau regions. Since R_{vk} hardly changes for the hard wear resistant coated surfaces such as the Ni-SiC on all the liner surfaces reported in this thesis, it is not a very good measure of any form of wear performance. Fully flooded inlets are assumed as the result of this finding in all the analytical predictions on chapter 7.

Finally, it is clear that the conclusions made here are quite novel, and not hitherto reported by any study in open literature, except by the current study **Gore et al (2011)**. They are, however, only generic to the range of plateau honed liners with hard wear resistant coatings and configurations used in motor racing high performance engines. However, it is reasonable to assume that these findings can be extended to any similar engine configuration as the running conditions reported here result in sliding speed range of 0-35m/s and side loads (contact forces) in excess of 4.5kN, which more than envelopes the running conditions of most IC engines.

Chapter 6

Experimental Procedure and Results

6.1 Introduction

This chapter is devoted to the experimental results obtained using the designed and developed floating liner described in chapter 4. In order to ensure repeatability of the results a detailed experimental procedure was developed and adhered to for all the tests carried out. This procedure is highlighted in this chapter and is complemented by the topographical measurements and reported wear characteristics in chapter 5.

This chapter reports on a series of tests carried out with the floating liner in a systematic manner. All tests were carried out on the engine test bed described in chapter 3. These comprise some initial engine tests under a motorised condition with the cylinder head removed (open cylinder, unpressurised) to ensure operational integrity of the floating liner principle described in chapter 4. A number of engine tests were then undertaken with the cylinder head in place and with the engine motorised. Quite representative results of engine cold running conditions can be achieved with this testing configuration as the Honda CRF 450R engine develops chamber pressures of the order of 20-30bar even when not fired. However, the temperature of surfaces and the lubricant alters under the usual engine fired conditions, as does thermo-elastic deformation of piston skirts and the floating cylinder liner. The loading of the contacts is also different to that usually experienced under fired conditions. These effects alter the tribological conditions in piston skirt-liner and ring-pack-liner conjunctions. Therefore, a large number of tests under various engine fired conditions (load-speed combinations) were carried out, a representative sample of which is provided with analysis of results in this chapter.

6.2 Controlled Parameters

Table 6.1 provides a list of parameters controlled during the reported engine testing work with the Honda CRF 450R engine, fitted with the floating liner. The method of control undertaken and the reason(s) for the control of each parameter are also noted in the table.

Controlled Parameters				
Parameter	Control method	Min	Max	Reason
Water temperature	A thermostatic controller was used to control the feed pump.	80°C	100°C	Engine temperature must be controlled as the lubricant viscosity varies with temperature. Common industry-based operating temperatures are used.
Oil temperature	Monitored. Tests are terminated if requirements not met.	90°C	120°C	Oil viscosity and load carrying capacity varies with temperature. These are the optimal temperatures for test oils used in this investigation.
Exhaust temperature	Monitored. Tests are terminated if requirements not met.	650°C	800°C	Excessive or low temperature is a sign of poor engine running and deemed as unrepresentative.
Fuel temperature	Monitored by computer.	air temp -1°C	air temp +1°C	Required for correction factor.
Cell air temperature	Monitored by computer.	-1°C from start	+1°C from start	Required for correction factor.
Air Fuel Ratio	Monitored by computer, test stopped if out of limits.	12.5	14	High or low ARF is a sign of poor engine running and is not considered as representative of proper test conditions.

Oil quality	Changed after every test or after 1hour of running. Single batch used for all testing.	Sent for chemical analysis after testing.		Oil degradation affects load carrying capacity and debris can damage surfaces and cause excessive wear.
Intake Air Humidity	Monitored by computer.			Monitored and used for correction factor.
Speed	Dyno controlled	1% of demand		
Torque	Dyno controlled	1% of demand		
Throttle	Dyno controlled	1% of demand		
Fuel Quality	Same batch for all tests.	Sent for chemical analysis after testing.		Fuel affects power.
Piston, rings, cyl liner	Measured for geometry and topography prior to testing.	Tolerances specified on component drawings.		Incorrect component sizes/finishes will influence clearances and thus tribological conditions.
Cylinder Pressure	Monitored by computer, test stopped if out of limits.	5% of maximum at all speeds at start of test.		High or low cylinder pressure is a sign of poor engine running and is not representative.
Blow-by	Monitored by computer, test stopped if out of limits.	10L/min	60L/min	High or low blow-by is a sign of poor engine running and is not representative.

Table 6.1: Control parameters

6.3 Operational Performance of the Floating Liner

The first step in the testing program is to ascertain the operational integrity of the floating liner system as was initially perceived in its design and described in section 4.2.1. Referring to equation (4.1) in section 4.2.1, it is clear that with the cylinder head removed (figure 6.1(c)), there is no significant pressure loading of the liner. Thus, the only applied force to the liner would be friction as the result of its interactions with the piston: $P \approx 0, -F = ma_l$. Considering the interfacial shear between a film of lubricant and the bounding solid surfaces (those of the piston and the liner), figure 6.1 (b) shows that the friction acting on the liner and the piston are in the same sense. Thus, the liner is dragged by the moving piston. The liner is restrained by the arrangement of the load cells (see chapter 4), hence there is a significant difference between its acceleration, a_l and that of the piston, a_p due to the sliding motion. Therefore, a film of lubricant is expected to entrain into all the piston-liner conjunctions, which is sheared at the relative sliding velocity:$\Delta u = v_p - v_l$ in the opposite sense to that of the piston motion. So long as this relative motion persists (i.e. $\Delta u \neq 0$), the liner velocity remains proportional to the piston speed, which follows a quasi-harmonic (sinusoidal) variation **Rahnejat (1998)** as in figure 6.1(a):

$$v_p(\varphi) = r\omega(sin\omega t + \frac{r}{2l} sin2\omega t + \cdots) \tag{6.1}$$

where: $\varphi = \omega t$ is the nominal crank-angle position (with the top dead centre, TDC designated at position $\varphi = 0°$ crank angle in transition between the compression and the power stroke and every 720° thereafter in the 4-stroke engine used in this thesis) *r* and l are the crank-pin radius and connecting rod length respectively.

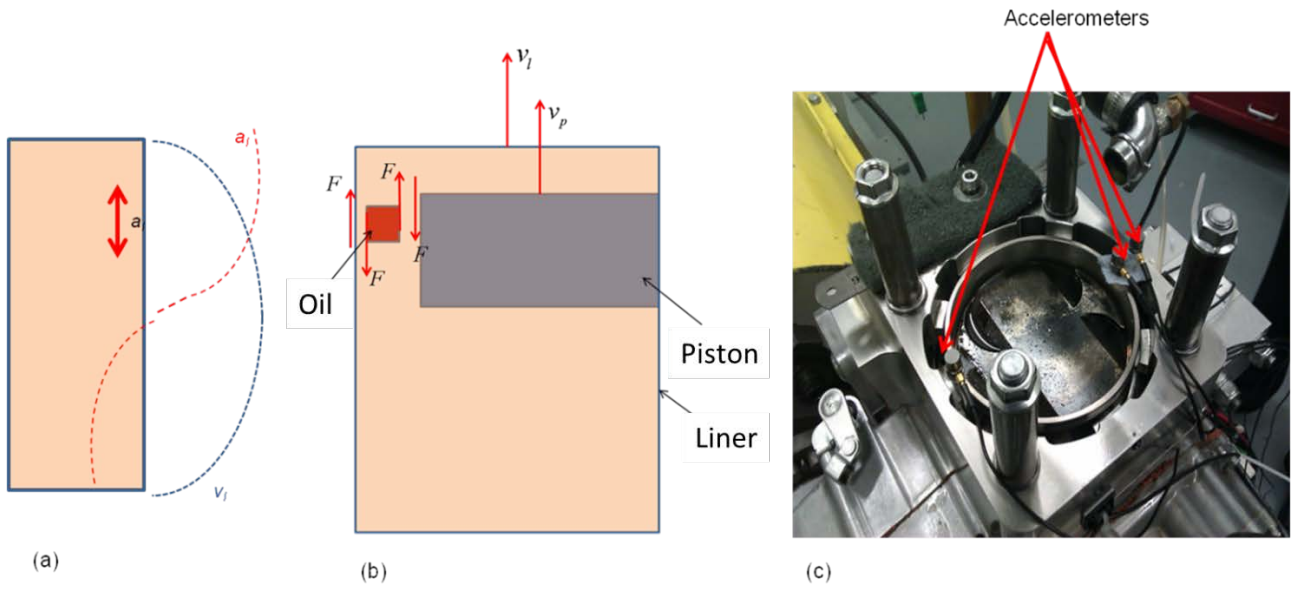

Figure 6.1: Floating liner with cylinder head off

(a)- Liner kinematics, (b)- Friction generation, (c)- Measuring inertial dynamics

There are two components contributing to the shear of the lubricant film as it is entrained into the various piston-liner conjunctions and flow along the contact conjunctions (piston skirt-liner and ring-pack-liner contacts). The first component of shear is caused by pressure rise at the inlet. This is known as the Poiseuille shear. The second contributing source to lubricant shear is prominent in the flow of lubricant within a conjunction itself, due to relative velocity of the surfaces. This is termed Couette shear. Therefore, viscous shear is a combination of these two effects, yielding the viscous friction as:

Viscous friction is: $F = \tau A = \left(\pm \frac{h}{2}\frac{\delta p}{\delta x} + \frac{\eta \Delta u}{h}\right) A$ (6.2)

with the Poiseuille shear (the former term in the parenthesis) being insignificant due to the small pressure gradient in the axial direction of the piston with an open cylinder head. Hence, friction, $F \propto \Delta u \propto v_p$ (proportional to the piston speed) and the motion of the floating liner with the cylinder head off is also quasi-harmonic following a similar trend as in figure 6.1(a). This is ascertained by positioning

accelerometers on the rim of the floating liner as well as the holding fixture, firmly attached to the engine block. This test is crucial in order to ensure that the engine block vibration, which is prevalent in the case of a single cylinder engine, does not affect the integrity of the load cell readings. Therefore, with the cylinder head removed and friction being the only applied force, a quasi-harmonic load cell output is expected, proportional to Δu (or the piston speed, v_p). The floating liner motion may be regarded as semi-simple harmonic. This is verified by the results in figure 6.2.

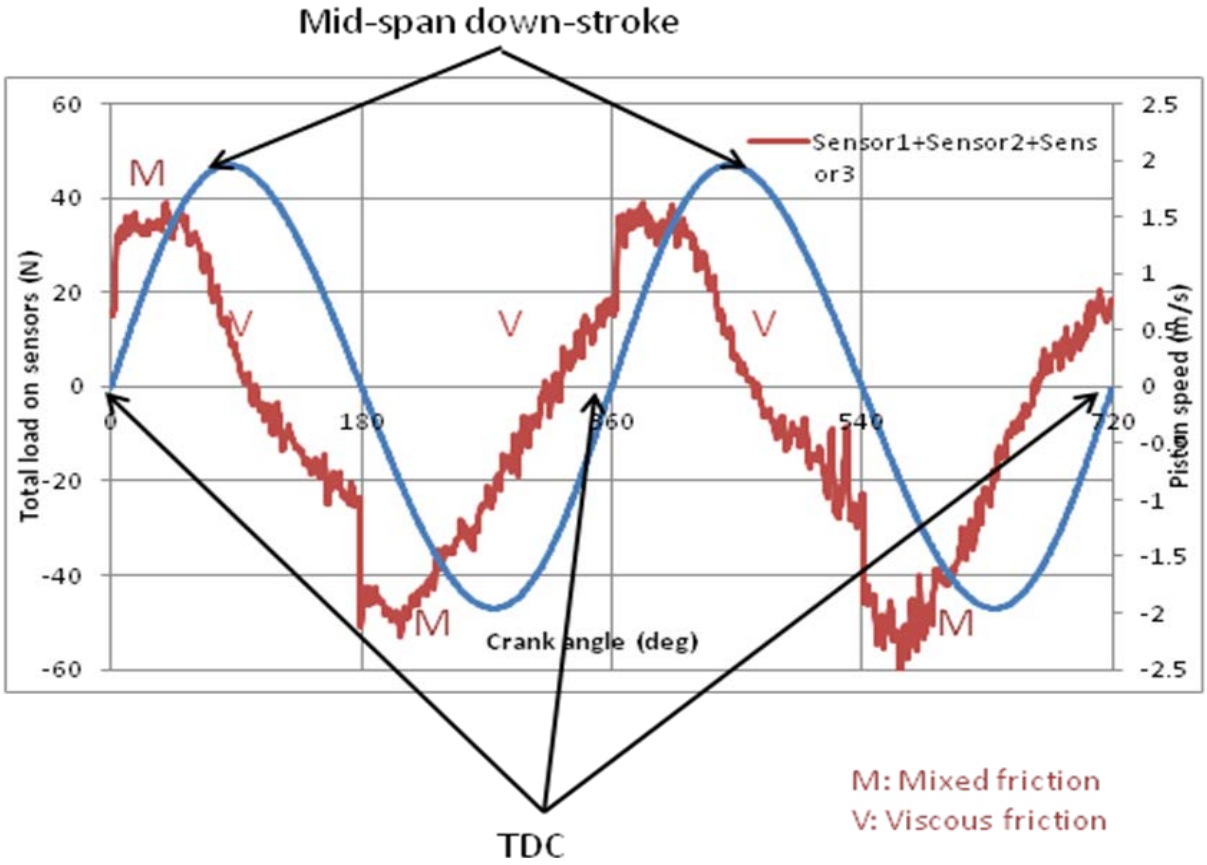

Figure 6.2: Measured friction with cylinder head removed

Figure 6.2 shows the measured friction at the engine speed of 500 rpm; $F = -ma_i$ for 2 engine cycles with no cylinder head in place. The piston speed (equation (6.1)) is also plotted on the same figure. Note that except at the dead centre reversals (TDC and BDC, every 180°crank angle position) and in their immediate vicinity, the

slope of the friction trace is directly proportional to that of piston speed or the relative sliding velocity Δu. This suggests that the dominant mechanism underlying friction is through viscous shear of a lubricant film (the Couette component of lubricant shear), as already discussed above. This direct proportionality is lost at the dead centre reversals, indicating the presence of some boundary friction. Therefore, a mixed regime of lubrication is prevalent at the TDC and BDC (figure 6.2). The change of sense of friction occurs at mid-span piston position. This indicates momentary uniform velocity of the liner at mid-stroke position (i.e. $a_l = a_p = 0, \Delta u = 0, F = 0$). These are instances of *freely* floating liner.

Now with the operational integrity of the floating liner ascertained a series of test conditions under motorised and fired engine conditions are undertaken.

6.4 Monitoring of Piston Friction Under Motorised Running Condition

Most reported work with floating liners incorporated in test rigs or engines (see chapter 2) relate to motorised engine running conditions or tests undertaken at quite low speed fired tests with significant noise and vibration (**Akalin and Newaz, 2001, Furuhama, 1980, Yoshida *et al,* 1990 and O'Rourke *et a,l* 2010**). However, some improvements were made to enable measurements under fired conditions, for example by **Furuhama and Sasaki (1983)**. The motorised tests represent relatively cold running conditions, which at low engine speeds correspond to some urban driving conditions which can lead to more significant viscous frictional power loss and increased emissions on account of higher lubricant viscosity at lower surface temperatures (i.e. $f \propto \tau \propto \eta$). These conditions constitute parts of the North American emission cycle tests and the New European Emission Drive Cycle (NEDC) (**The European Federation for Transport and Environment, 2006**). These conditions also reproduce the large number of interactions which occur under fired engine running conditions, which are initiated by reduced lubricant viscosity (thinner films, thus increased boundary interactions) and thermo-elastic deformation of the

liner and the piston skirt, thus reduced running clearances (**McClure, 2007 and Bai, 2012**).

Morris *et al* (2013) have shown through numerical analysis that thermal mixing at the inlet nib of the compression ring-liner contact results in lubricant temperature rise above that of both the solid boundaries; the liner surface and that of the ring itself. This is as the result of convective heat transfer from the solid surfaces into the entrant lubricant, and its subsequent shear heating within the contact. Therefore, under motorised conditions, with low solid boundary temperatures, the lubricant contact temperature remains only marginally above that in the bulk (the sump temperature). Consequently, the relatively high viscosity of cold lubricant in motorised tests means that the dominant cyclic friction would be due to lubricant viscous action in the presence of any film of lubricant. The other source of lubricant shear is due to the Poiseuille flow (described in the previous section) at the conjunctional inlet at the TDC reversal, if significant chamber pressure is generated under motorised conditions, which is around 19 bar for the Honda CRF 450R with the cylinder head in place and motoring at 2500 rpm (figure 6.3). Therefore, unlike other reported test rigs, the effect of realistic pressure loading, particularly on the compression ring conjunction is included in the current motorised tests.

Table 6.2 provides a list of engine test conditions reported here for the engine speed of 2500 rpm. The aim is to present a full set of results for motorised engine testing and fired engine conditions at partial (30Nm) load and full (72Nm) load conditions. Then, the dominant transient nature of tribological conditions can be ascertained and described. Subsequently, in later sections the effect of higher engine speeds are also demonstrated.

	Motorised engine	Fired engine	
Engine speed (rpm)	2500	2500	2500
Throttle position (%)	100	25	33
Chamber pressure (bar)	19	16	35
Dyno Torque (Nm)	n/a	30	72
Engine Torque (Nm)	n/a	7.5	18
Test cell temp. (˚C)	20.8	21.6	20.2
Test cell pressure (mbar)	1020	1015	1006
Test duration (sec)	30	20	20
Air fuel Ratio	n/a	13.5:1	13.0:1
Coolant temperature (˚C)	n/a	n/a	n/a
Sump oil Temperature (˚C)	25	25	35
Liner Temperature (˚C)	38	42	48
Gear Ratio	4.02	4.02	4.02
Lubricant	SAE 10W40	SAE 10W40	SAE 10W40

Table 6.2: Test conditions: motorised and fired with different engine loading

Figure 6.4(a) shows the measured friction by the floating liner, motorised at the engine speed of 2500 rpm. The TDC position is at 720° crank-angle (in transition from the compression to the power stroke). The maximum chamber pressure of 19bar occurs at this position and every 720° crank-angle thereafter. Positions 180° crank-angle and every 360° thereafter correspond to the BDC reversal. Friction changes sense of application at the motion reversal positions. There are slight differences in friction characteristics at the BDC from power to exhaust stroke and that from the intake to the compression stroke. The higher friction in the former transition (i.e. power to exhaust stoke) is because of a higher pressure gradient change. As in the case of the open cylinder head described in the previous section (i.e. head off), the regions that the friction trace remain proportional to the service parameter $\eta_0 \Delta u \propto v_p$ are due to viscous shear of the lubricant film (second term in equation (6.2)). These mainly occur in all the strokes between piston reversals and particularly at piston mid-strokes (at crank angle of 90˚ and every 180˚ thereafter).

With an oversized piston closely conforming to the floating liner providing a nominal clearance of 50μm it is possible to remove the two piston rings (compression and oil

control ring) for motored testing only. Figure 6.4(b) shows the measured friction characteristics with the piston skirt only. Comparison of the result with that of the complete piston assembly (including the rings) shows some interesting features. Firstly, the stipulated friction due to Poiseuille shear occurs precisely at the BDC reversal from power to exhaust strokes (at 180˚, 900˚, ...) rather than the somewhat delayed peak in figure 6.4(a). This is because at the BDC reversal the compression ring moves from the top piston groove land as the motion reverses, thus the pressure gradient has a delayed characteristics. Ring axial flutter is often surmised through numerical analysis, but no experimental evidence has hitherto been provided.

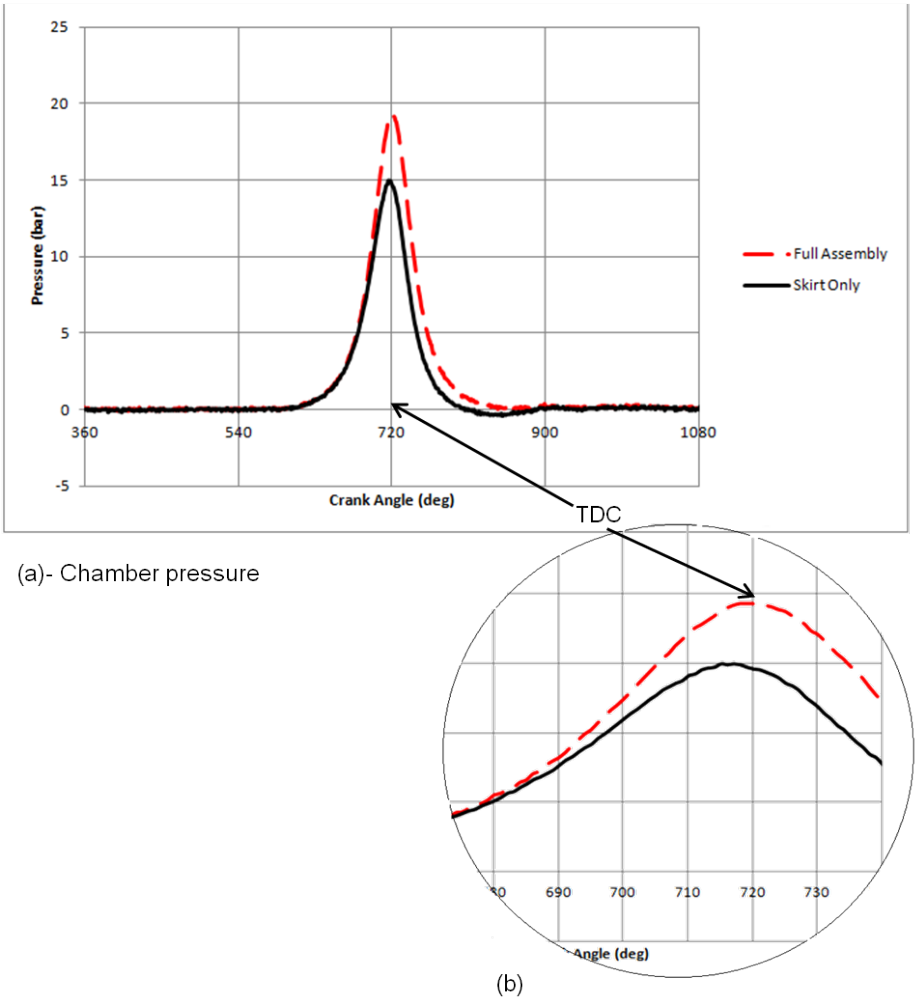

Figure 6.3: Chamber pressure under motorised condition at 2500 rpm

At piston mid-span positions, the viscous friction is significantly diminished, because without the oil control ring the skirt-liner conjunction is flooded. Friction in transition from compression to power stroke (0˚,720˚) is reduced at the reversal, because of the flooded inlet to the conjunction due to the lack of an oil control ring . Hence, the rise in friction prior to the TDC is entirely due to reduced Poiseuille flow shear loading. With a compression ring present, the peak transition friction occurs closer to the reversal, again as the ring moves this time from the bottom groove land. This is clearly observed in the difference in the measured chamber pressure variation near the TDC between the full piston assembly and that with the skirt only (figure 6.3(b)). The sharp rise in friction in the power stroke is a combination of Poiseuille shear and somewhat reduced boundary interactions.

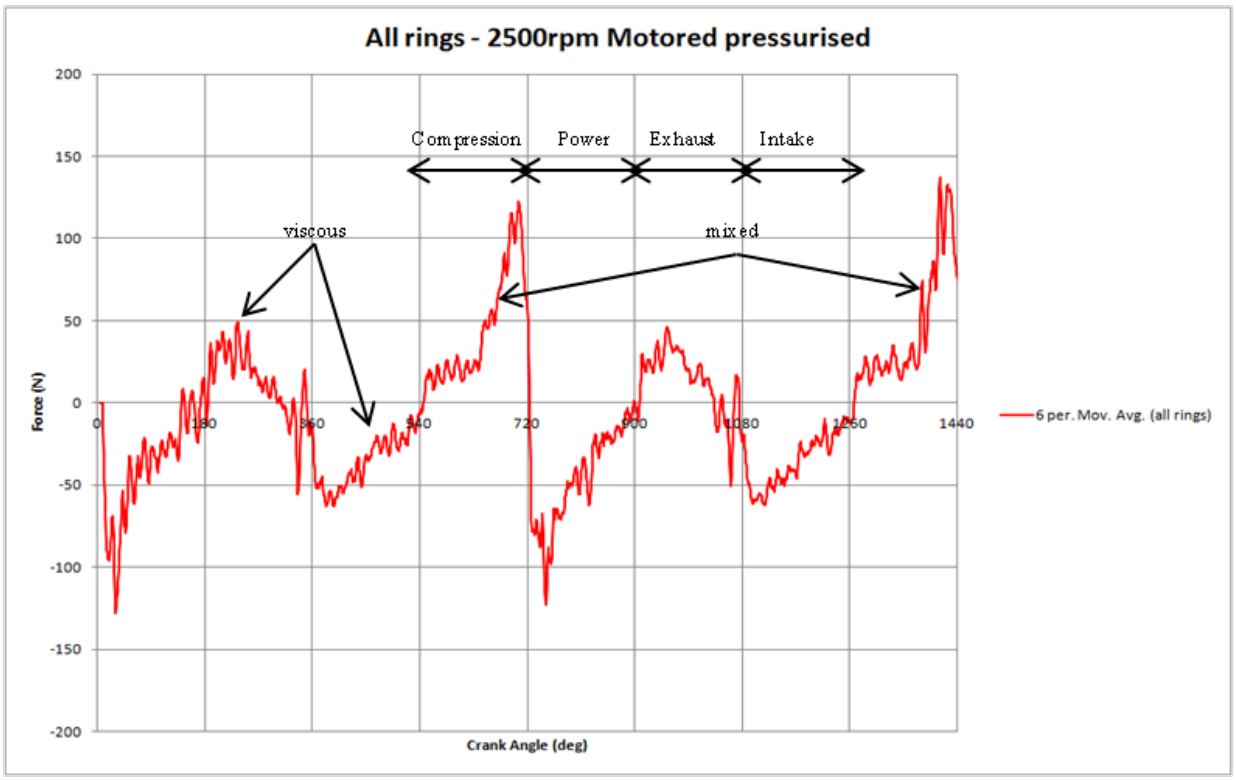

(a)

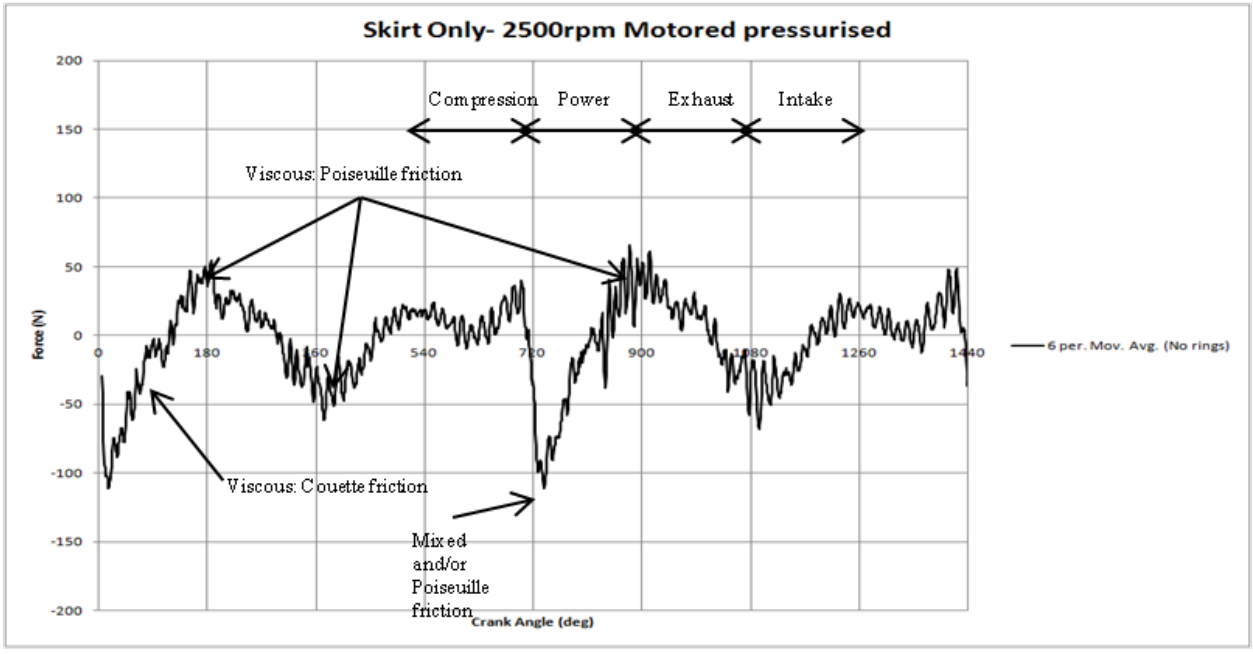

(b)

Figure 6.4: Measured friction under motored condition

(a)- complete piston assembly, (b)- piston skirt conjunction only

An overall comparison of figures 6.4(a) and 6.4(b) shows that piston-liner friction is mainly governed by the compression ring sealing at the reversals, particularly in the transition between the compression to power stroke. At the BDC reversals and at the TDC in transition from exhaust to intake, the Poiseuille shear is the dominant source of friction, which can be affected by the axial flutter of the compression ring. The delayed nature of Poiseuille friction due to ring axial motion is indicative of the crucial sealing role of the compression ring. Another important observation from the motorised test results is that for most of the engine cycle lubricant shear, either as the result of Couette or Poiseuille flow, accounts or the main contributions, except for the TDC reversal from compression to the power stroke. However, this may not directly correspond to real engine fired conditions.

6.5 Monitoring of Piston Friction Under Engine Fired Conditions

The fired engine results correspond to a steady running condition at 2500 rpm, a torque of 30 Nm at 25% throttle and a maximum combustion pressure of 16bar at 13˚ past the TDC in the power stroke is shown in figure 6.5. In figures 6.4,6.5 and 6.6 friction is represented as opposing the direction of motion.

A comparison of results in figure 6.5 with those of figure 6.4(a) shows a number of important changes. Firstly, as it would be expected, the contribution to friction due to viscous shear of the lubricant film is decreased because of the lower effective viscosity caused by the rising temperatures of contacting bounding solids under fired conditions. Note that the steady bulk oil temperature at 25˚C is increased above the liner temperature at the contact inlet and is further increased through shear in transit through the contact. Thus, the entrant lubricant flows into the contact of all the piston-liner conjunctions at a higher temperature. As the result of short testing times the difference in the liner temperature between the motored and fired conditions is only few ˚C in these cases. However, with longer testing periods a larger difference would be expected. There is a significant reduction in friction at the TDC reversal in

the latter stages of compression under fired condition. This is because of a higher side load (engine torque), and the compression ring sealing function is enhanced. Thus, there is lesser pressure gradient, $\frac{dp}{dx}$ across the ring as well as a reduced film thickness due to lower lubricant viscosity as already noted. Therefore, the influence of Poiseuille shear; $\frac{h}{2}\frac{dp}{dx}$ is significantly diminished compared with the motored results in figure 6.4(a). Immediately upon reversal and within the power stroke, however, friction is increased under fired condition because a thinner lubricant film results in increased boundary interactions.

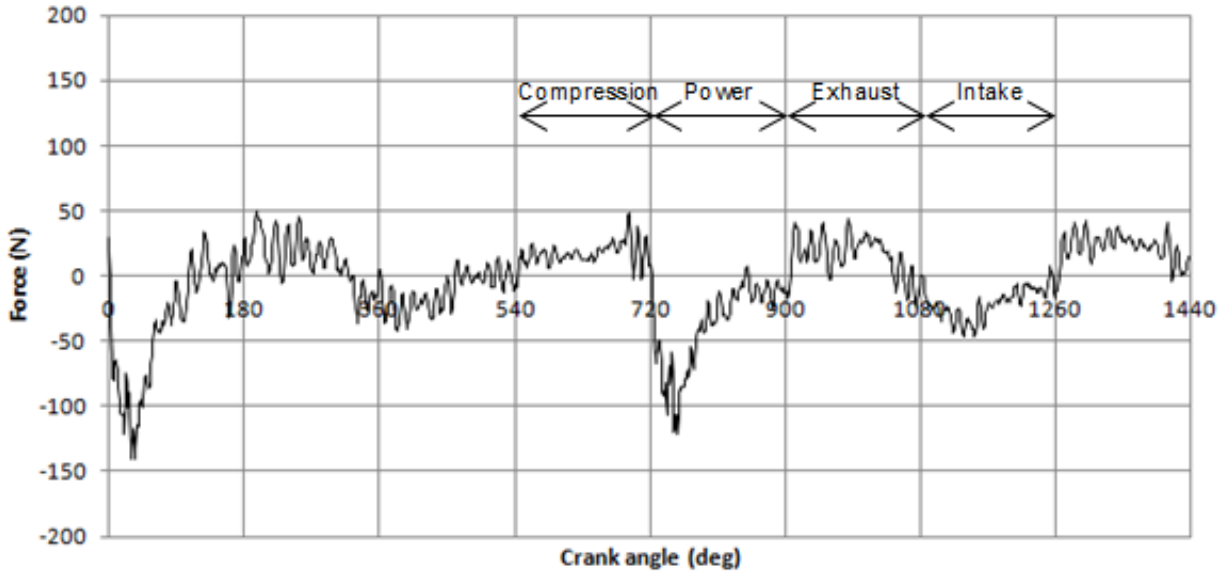

Figure 6.5: Measured friction under fired engine condition at 2500 rpm, torque of 30Nm

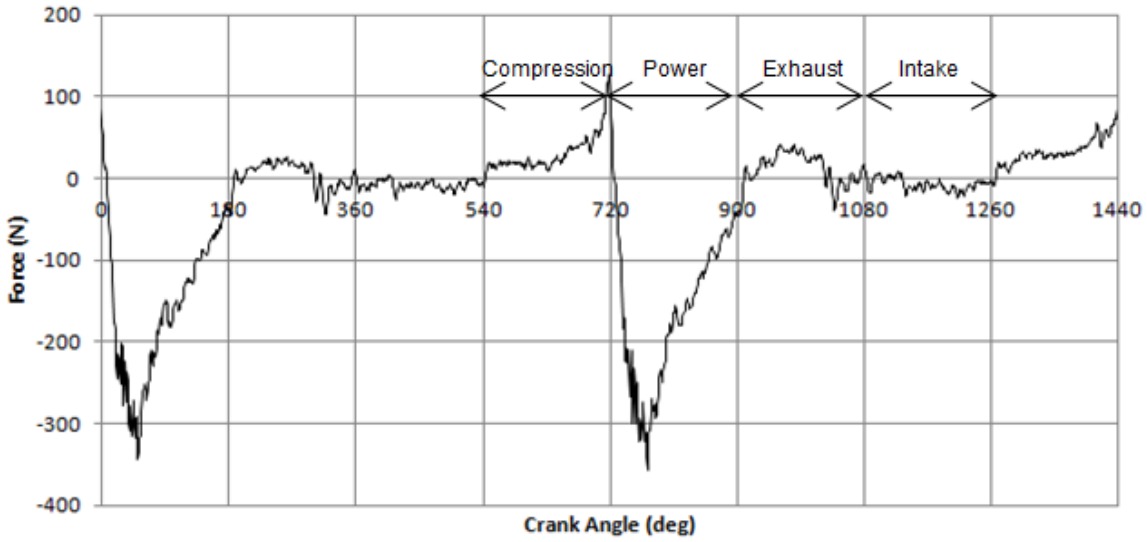

Figure 6.6: Measured friction under fired condition at 2500 rpm, torque of 72 Nm

With increased throttle, the engine torque is increased to 72 Nm in figure 6.6. The boundary friction at reversals (0° crank-angle at TDC and every 720° thereafter) is increased compared with figure 6.5, because of increased contact load. The increased contact load is due to increased combustion pressure acting behind the compression ring, pushing it to adhere to the cylinder liner wall. Therefore, the boundary friction at TDC reversal has nearly doubled with increased engine loading as one would expect. Another interesting point to note is that there is no increase in friction elsewhere during the engine cycle with increased throttle. This is because for most of the cycle viscous friction is dominant, which is a direct function of piston sliding speed which is the same for both figures 6.5 and 6.6. Therefore, one can observe that with increased engine loading at the same engine speed the proportion of cyclic friction at TDC reversal from compression to power stroke increases markedly as a function of combustion pressure. The area under the friction trace in all these figures represents the work done to overcome friction, or directly proportional to the frictional power loss. It is now clear that the reversal at the TDC from compression to power stroke represents the most significant part of frictional losses, which is exacerbated with increased engine loading. Although this finding is

intuitive and often surmised in literature, it has not hitherto been demonstrated as shown here.

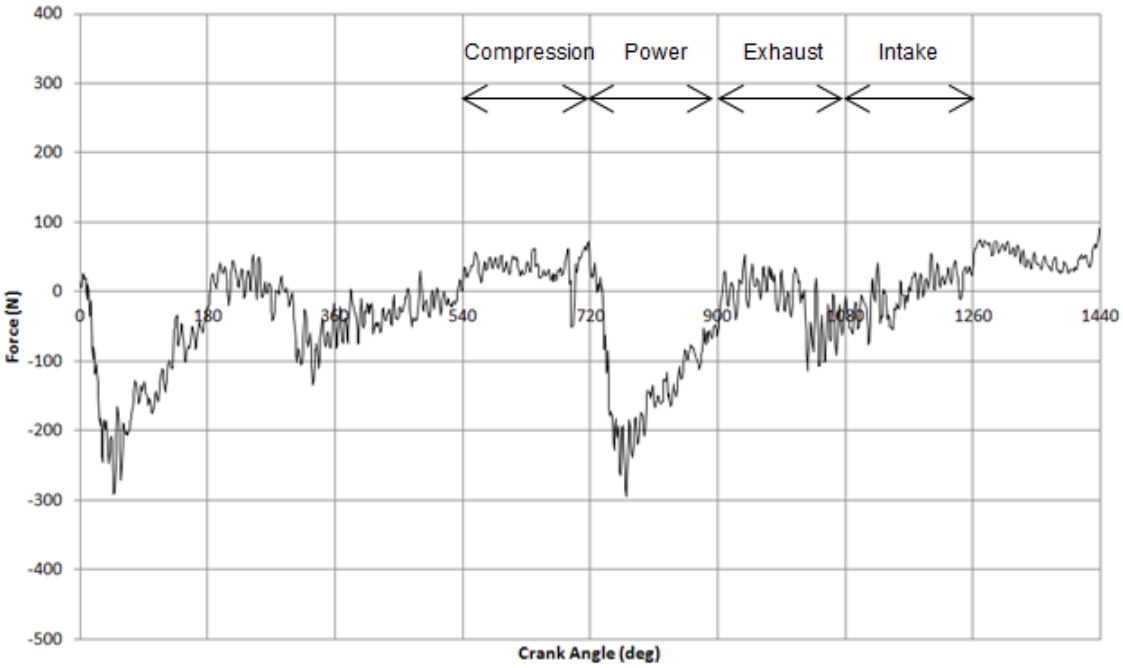

Figure 6.7: Measured friction under fired engine condition at 4000 rpm, torque of 72 Nm

Figure 6.7 is at the same engine torque, but at the higher speed of 4000 rpm as opposed to the results in figure 6.6. Two points are noteworthy in comparing figures 6.6 and 6.7. With increased engine speed, the piston sliding speed is increased, thus the lubricant shear rate increases as shear stress is directly proportional to the sliding speed. Therefore, viscous friction is slightly increased throughout the cycle. However, this is not as notable as the decrease in friction at the TDC from compression to power stroke (from more than 300 N to less than the same value). This shows that the regime of lubrication at the TDC reversal is actually mixed rather than pure boundary condition. With an increased sliding speed a thicker film is retained through the reversal. This somewhat reduces the extent of boundary interactions and hence reduces friction. Nevertheless, the significant finding remains that a significant portion of friction is at TDC from compression to power stroke. This means that surface modification features to retain a film of lubricant at the TDC is the most appropriate method of reducing cylinder friction rather than reducing the

lubricant viscosity as it is sometimes suggested. This is another important finding of this thesis.

There are several possible sources of error in the recorded data. Firstly, the single cylinder geometry is prone to unbalanced vibration (**Rahnejat, 1998**). This causes a certain amount of noise in the recorded load cell data (see typical figure 6.7). Therefore it is essential to remove the noise from the output signal. A 10-point moving average method is employed to achieve this.

There may be some noise content due to slip-stick conditions, particularly at reversals with thin films and some direct asperity contact. There is also the possibility of side impacts which may appear as noise on the signal, this cannot be ascertained with the current apparatus. However, overall the experimental results show good characteristic repeatability and conform to numerical predictions, which imparts a good degree of confidence in their validity.

Chapter 7

Numerical Modelling and Predictions

7.1 Introduction

It is necessary to develop an analytical solution in order to combine predictions with measured tribological conditions in the previous chapters and fundamentally understand the mechanism of lubrication in a typical engine cycle under various conditions. This chapter deals with the development of such a representative analysis tool. An analytical, rather than a numerical approach is preferred in this thesis, because firstly it suffices for the purpose highlighted here (see section 7.2) and it is a closed form elegant and computationally rapid solution.

Simulations are carried out for comparison of predictions with friction measurements using the slider rig mechanism as well as the floating liner results from the engine tests. This serves the purpose of gauging the validity of the modelling method at the basic science level, where many interactions present for engine conditions do not exist. The evaluated analytical approach is then refined and used together with the engine test results to ascertain in situ tribological conditions under the various engine testing conditions.

The one dimensional model described in section 7.2 assumes a fully circumferentially conforming ring-bore contact. This means that any ring gap gas flow is ignored in the analysis. To include the effect of ring gap and its conformance with the cylinder bore a number of features are required. These include bore out-of-roundness and a 2D analysis of the contact, such as reported by **Rahmani et al (2012)**.

7.2 One Dimensional Long Line Contact Solution

The one dimensional analysis in this section applies to the slider bearing conjunction (section 3.3) or a fully circumferentially assumed conforming ring to the liner surface. One can start from a one dimensional solution to Reynolds' equation. The assumptions for this to hold true are:

- The ring face-width is much smaller than its length in effective contact with the cylinder bore. **Haddad and Tian (1995)** and **Perera et al (2010)** state that this assumption can be upheld, if: $b < \frac{1}{30}\pi D$, where b is the ring face-width and D is the bore diameter (assuming perfect conformance between the ring and the bore in the circumferential direction). Therefore, the pressure gradient along the ring face-width (axial x-direction) is considered to be much larger than along its periphery (circumferential direction: $y = \frac{D}{2}\emptyset$, y assumed to be the representative unwrapped ring dimension). **Mishra et al (2008)** for a typical motocross motorsport engine (Honda CRF 450R), using 2D numerical analysis shows that for typically very thin compression rings (b≈0.8-1.2mm) this assumption is quite reasonable. Thus: $\frac{\partial p}{\partial x} \gg \frac{\partial p}{\partial y}$, hence: $\frac{\partial p}{\partial y} \approx 0$

- Side leakage of lubricant into the direction of ring periphery y is considered to be negligible. This is quite a reasonable assumption, given that the regime of lubrication remains mixed or boundary for some of the piston cycle, particularly at the dead centres and immediately after or prior to these locations (**Mishra et al (2009)**, **Bolander et al (2005)** and **Hu et al (1994)**). This is because the film thickness is usually very thin. The lubricant film is found to be of the order of a few tenths to several micrometres even away from these locations (**Akalin and Newaz (2001)**, **Mishra et al (2009)**). Hence, one can safely assume that there is an insufficient supply of lubricant to initiate any side leakage of small entrained volume, $v \approx 0$. This assumption

eliminates the term $v\frac{\partial h}{\partial y}$ in Reynolds' equation. Thus, Reynolds' equation becomes:

$$\frac{\partial}{\partial x}\left(\frac{\rho h^3}{\eta}\frac{\partial p}{\partial x}\right) = 12\left(U\frac{\partial(\rho h)}{\partial x} + \frac{\partial(\rho h)}{\partial t}\right) \tag{7.1}$$

where the lubricant entrainment velocity is given as: $U = \frac{1}{2}(u_1 + u_2)$, these being the axial sliding velocities of the ring and the bore surface respectively. Thus: $u_2 = 0$. Hence: $U = \frac{1}{2}u_1 = \frac{1}{2}\dot{x} = \frac{1}{2}\frac{dx}{dt}$. Furthermore, low hydrodynamic pressures (of the order of few to few tens of MPa) have insignificant effect on lubricant density and viscosity. Thus, the most simplified form of Reynolds' equation for iso-viscous condition is arrived at:

$$\frac{\partial}{\partial x}\left(h^3\frac{\partial p}{\partial x}\right) = 6\eta_0\left(U\frac{\partial h}{\partial x} + 2\frac{\partial h}{\partial t}\right) \tag{7.2}$$

The above stated assumption with regard to lubricant rheological state needs to be justified if the form of Reynolds' equation (7.2) is to be used for an analytical approach. The validity of an iso-viscous assumption holds for very low values of the product αp, where α is the pressure viscosity coefficient of the lubricant. For most engine oils this is around $10^{-8}Pa^{-1}$. Pressures reported in the studies carried out by **Mishra et al (2008, 2009)**, **Akalin and Newaz (2001)**, **Ma et al (1997)** and **Bolander et al (2005)** among others are in the range of $10^7 - 10^8 Pa$, making $\alpha p \leq 1$. If one uses the **Barus law (1893)** as the basis for lubricant viscosity dependence on pressure; $\eta = \eta_0 e^{\alpha p}$, then it is clear that viscosity of lubricant hardly alters, and one can, for simplicity, assume an iso-viscous behaviour. This makes for a simple 1D analytic solution described below in section 7.1.2. However, such a solution can be extended to piezo-viscous pressures as in **Rahnejat (1984)**.

The most basic analytical solution for equation (7.2) for a sliding contact can be obtained where: u, the speed of entraining motion, is replaced by the sliding speed

$\Delta U = U_1 - U_2 = U_1$, where $U_2 = 0$, for example for the slider rig, described previously or the cylinder liner/bore surface. Hence:

$$\frac{\partial}{\partial x}\left(h^3 \frac{\partial p}{\partial x}\right) = 6\eta_0 \left(U \frac{\partial h}{\partial x} + 2\frac{\partial h}{\partial t}\right) \tag{7.3}$$

assuming a hydrodynamic film thickness of the form:

$$h = h_0 + \frac{x^2}{2R} \tag{7.4}$$

since the equivalent radius of the contact: $R \gg h_0$ R is the crown radius of an assumed parabolic ring face-width profile.

Rahnejat (1984) and **Sasaki et al (1962)** have obtained such analytical solutions. Assuming steady state sliding, i.e. without the second term on the right hand side of equation (7.3), then:

$$\frac{\partial p}{\partial x} 6U\eta_0 \frac{h-h_0}{h^3} \tag{7.5}$$

using the non-dimensional groups: $\bar{x} = \frac{x}{\sqrt{2Rh_0}}$, $\bar{h} = \frac{h}{h_0}$then equation (7.4) becomes:

$$\bar{h} = 1 + \bar{x}^2 \tag{7.6}$$

letting: $\bar{p} = \frac{{h_0}^{3}/_{2} p}{6U\eta_0\sqrt{2R}}$, then equation (7.5) without the ultimate term can be written as:

$$\frac{d\bar{p}}{d\bar{x}} = \frac{\bar{x}^2 - {\bar{x}_0}^2}{(1-\bar{x}^2)^3} \tag{7.7}$$

integrating with respect to $\bar{x}$:

$$\bar{p}\int \frac{\bar{x}^2 d\bar{x}}{(1-\bar{x}^2)^3} - {\bar{x}_c}^2 \int \frac{d\bar{x}}{(1+\bar{x}^2)^3} \tag{7.8}$$

Carrying out the integration shows that:

$$\bar{p} = \left[\frac{-\bar{x}}{4(1+\bar{x}^2)^2} + \frac{\bar{x}}{8(1+\bar{x}^2)} + \frac{1}{8}tan^{-1}\bar{x}\right] - {\bar{x}_c}^2\left[\frac{x}{4(1+\bar{x}^2)^2} + \frac{3}{8}\frac{\bar{x}}{(1+\bar{x}^2)} + \frac{3}{8}tan^{-1}\bar{x}\right] + C_1 \tag{7.9}$$

where the position x_c for $\frac{d\bar{p}}{d\bar{x}} = 0$ (maximum position in Sommerfeld boundary conditions or film rupture in the case of Swift-Stieber boundary conditions) is not known. Also, the constant of integration C_1 should also be evaluated.

the Swift-Stieber boundary conditions state:

$$\bar{p} = \frac{d\bar{p}}{d\bar{x}} = 0 \; at \; \bar{x} = \bar{x}_c \tag{7.10}$$

using equations (7.9), (7.10) and integrating over the ring face-width, the lubricant reaction per unit length of the ring (viewed as wrapped) becomes:

$$\frac{W}{l} = \frac{2.45 U \eta_o R}{h_0} \tag{7.11}$$

where, the length of the ring is:

$$l = 2\pi r_0, \qquad where \; r_0 = bore \; radius$$

this expression can be used to determine the film thickness, if the applied contact load is assumed to equilibrate with the lubricant reaction (a quasi-static condition). The applied load on the strip straight ring section is known, thus for the slider rig, the film thickness can be determined readily. For the case of the engine compression ring, the applied load (W) is a combination of ring tension force (elastic force) (F_e) and the gas force acting behind the ring's inner peripheral rim (F_g):

$$W = F_e + F_g$$

both these forces tend to push the ring to conform to the liner surface. The elastic force is given as:

$$F_e = \frac{e_g E J}{3\pi r^3} \tag{7.12}$$

where: E is the modulus of elasticity of the ring, e.g. its end-gap before fitment $J = \frac{1}{12} b d^3$ and d is the ring thickness.

the gas force is obtained as:

$$F_g = 2\pi r_0 b p_g \tag{7.13}$$

which assumes complete circumferential conformance of the ring to the bore, which is not strictly true in practice, and p_g is the gas pressure, which is measured in chapter 6 under various conditions. Finally, the sliding velocity is measured by the encoder in the slider bearing rig and in the case of engine piston is given as **Rahnejat (1998)**: $\Delta U = \dot{x} = R\omega\left(sin\varphi + \frac{R}{2L}sin2\varphi\right)$, where φ is crank-angle, L the connecting rod length and R the crank-pin radius.

However, for the case of engine, the solution provided above ignores certain important salient practical considerations. In particular, there is no consideration of proper boundary conditions during the various strokes of the engine. Also, depending upon motored or fired engine tests, lubricant and surface temperatures should be taken into account. Finally, the lubricant film may be considered to comprise a number of zones or regions as shown in figure 7.1.

7.3 Long Line Contact Solution with Cavitation

The lubricant entrainment occurs along the ring face-width, x in a domain characterised by:

$$\mathrm{x} \in [\mathrm{a}, \mathrm{b}], \text{ where: } \mathrm{a} \leq \mathrm{c} < r \leq b \tag{7.14}$$

the parameters a, c, r and b represent the contact inlet (a), lubricant film rupture point and onset of cavitation region (c) , lubricant reformation boundary (r) and the outlet edge of the ring-face-width (b) respectively (Figure 7.1). These positions demarcate regions of assumed full film, cavitation and lubricant film reformation.

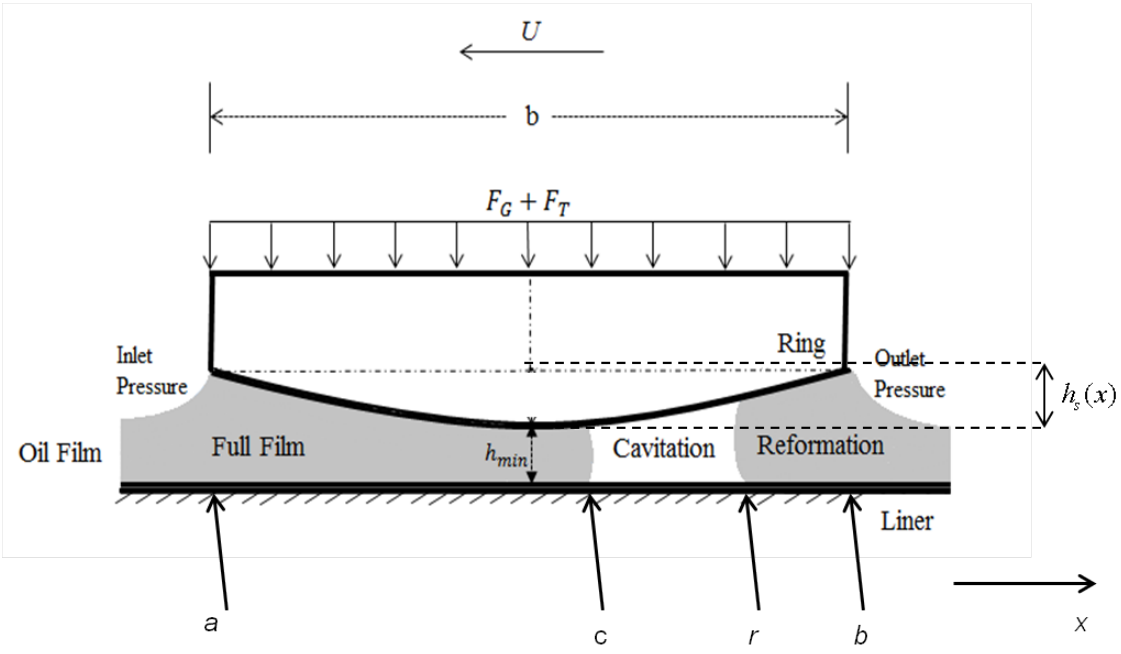

Figure 7.1: Lubricant film variation within the contact domain

Reynolds equation has to be solved simultaneously with the film shape function in a transient manner:

$$\mathrm{h}(\mathrm{x},\mathrm{t}) = \mathrm{h}_0(\mathrm{t}) + \mathrm{h}_\mathrm{s}(\mathrm{x}) \tag{7.15}$$

where, $\mathrm{h}_\mathrm{s}(\mathrm{x}) = \frac{\mathrm{x}^2}{2\mathrm{R}}$ is the parabolic shape of the ring face-width profile as in equation (7.4). h_0 is the same as the minimum film thickness in figure 7.1.

The appropriate boundary conditions for solution of Reynolds equation are:

$$\begin{cases} \mathrm{p}|_{\mathrm{x=a}} = \mathrm{P_a} & \text{(I)} \\ \mathrm{p}|_{\mathrm{x=c}} = \mathrm{P_c} & \text{(II)} \\ \left.\frac{\partial \mathrm{p}}{\partial \mathrm{x}}\right|_{\mathrm{x=c}} = 0 & \text{(III)} \\ \mathrm{p}|_{\mathrm{x=r}} = \mathrm{P_r} = \mathrm{P_c} & \text{(IV)} \\ \mathrm{p}|_{\mathrm{x=b}} = \mathrm{P_b} & \text{(V)} \end{cases} \tag{7.16}$$

The inlet pressure P_a varies according to the sense of motion of the piston (condition (I)). In the upstroke, it is the combustion chamber pressure, whilst in the down-stroke it is the inter-ring pressure, which is considered to be the atmospheric pressure in

the current study. The lubricant film ruptures at a position $x = c$, where the lubricant pressure falls below its cavitation vaporisation pressure P_c (Condition (II)). At this location, the third boundary condition in equation (7.16) is also taken into account which ensures flow continuity (Condition (III)). The second and third boundary conditions, taken together, are known as the Swift-Stieber boundary conditions as in equation (7.10). The pressure remains the same in the cavitation region, and gradually rises to that prevailing at the lubricant exit boundary at the edge of the ring (Conditions (IV) and (V)). These induce lubricant film reformation.

The solution to Reynolds equations has to take into account these differing boundary conditions in the various regions of the contact domain as shown in Figure 7.1.

7.3.1 Region of Full Film: $(a \leq x \leq c)$

In this region the boundary conditions are:

$$\begin{cases} \mathrm{p}|_{\mathrm{x=a}} = \mathrm{P_a} \\ \mathrm{p}|_{\mathrm{x=c}} = \mathrm{P_c} \\ \left.\frac{\partial \mathrm{p}}{\partial \mathrm{x}}\right|_{\mathrm{x=c}} = 0 \end{cases} \tag{7.17}$$

integrating from the conjunctional inlet (Entrance point, $x = a$) leads to:

$$\frac{\partial \mathrm{p}}{\partial \mathrm{x}} = \frac{6\eta\Delta\mathrm{U}}{\mathrm{h}^2} + \frac{12\eta}{\rho\mathrm{h}^3}\int_{\mathrm{a}}^{\mathrm{x}} \frac{\partial(\rho\mathrm{h})}{\partial \mathrm{t}}\,\mathrm{ds} + \frac{6\eta}{\rho\mathrm{h}^3}\mathrm{C}_1 \tag{7.18}$$

and a further integration yields:

$$\mathrm{p} = 6\Delta\mathrm{U}\int_{\mathrm{a}}^{\mathrm{x}} \frac{\eta}{\mathrm{h}^2}\,\mathrm{ds} + 12\int_{\mathrm{a}}^{\mathrm{x}} \left[\frac{\eta}{\rho\mathrm{h}^3}\int_{\mathrm{a}}^{\mathrm{s}} \frac{\partial(\rho\mathrm{h})}{\partial \mathrm{t}}\,\mathrm{d\acute{s}}\right]\mathrm{ds} + 6\mathrm{C}_1\int_{\mathrm{a}}^{\mathrm{x}} \frac{\eta}{\rho\mathrm{h}^3}\,\mathrm{ds} + \mathrm{C}_2 \tag{7.19}$$

using the first boundary condition, yields the value of C_2:

$$\mathrm{C}_2 = \mathrm{P_a} \tag{7.20}$$

from the second boundary condition ($\mathrm{p}|_{\mathrm{x=c}} = \mathrm{P_c}$):

$$\mathrm{P_c} = 6\Delta\mathrm{U}\int_{\mathrm{a}}^{\mathrm{c}} \frac{\eta}{\mathrm{h}^2}\,\mathrm{dx} + 12\int_{\mathrm{a}}^{\mathrm{c}} \left[\frac{\eta}{\rho\mathrm{h}^3}\int_{\mathrm{a}}^{\mathrm{x}} \frac{\partial(\rho\mathrm{h})}{\partial \mathrm{t}}\,\mathrm{ds}\right]\mathrm{dx} + 6\mathrm{C}_1\int_{\mathrm{a}}^{\mathrm{c}} \frac{\eta}{\rho\mathrm{h}^3}\,\mathrm{dx} + \mathrm{P_a} \tag{7.21}$$

from which the integration constant becomes:

$$C_1 = \frac{(P_c - P_a) - \left\{6\Delta U \int_a^c \frac{\eta}{h^2} dx + 12 \int_a^c \left[\frac{\eta}{\rho h^3} \int_a^x \frac{\partial(\rho h)}{\partial t} ds\right] dx\right\}}{6 \int_a^c \frac{\eta}{\rho h^3} dx} \quad (7.22)$$

now implementing the third boundary condition ($\left.\frac{\partial p}{\partial x}\right|_{x=c} = 0$):

$$\left.\frac{\partial p}{\partial x}\right|_{x=c} = \frac{6\eta_c}{\rho_c h_c^3}\left(\rho_c \Delta U h_c + 2\int_a^c \frac{\partial(\rho h)}{\partial t} ds + C_1\right) = 0 \quad (7.23)$$

or:

$$6\Delta U + \frac{12}{\rho_c h_c}\int_a^c \frac{\partial(\rho h)}{\partial t} ds + C_1 = 0 \quad (7.24)$$

replacing for C_1:

$$6\Delta U + \frac{12}{\rho_c h_c}\int_a^c \frac{\partial(\rho h)}{\partial t} ds + \frac{(P_c - P_a) - \left\{6\Delta U \int_a^c \frac{\eta}{h^2} dx + 12 \int_a^c \left[\frac{\eta}{\rho h^3} \int_a^x \frac{\partial(\rho h)}{\partial t} ds\right] dx\right\}}{6 \int_a^c \frac{\eta}{\rho h^3} dx} = 0 \quad (7.25)$$

solving this equation determines the point c; the location of the lubricant film rupture point.

Equation (7.25) is solved by Newton-Raphson iterations to determine the position $x = c$. Note that both P_a and ΔU are functions of the crank-angle location in an engine cycle. P_a is a function of chamber pressure or is simply atmospheric in the down-stroke of the piston.

7.3.2- The Film Reformation Region $(r \leq x \leq b)$

The boundary conditions for this region (cavitation) are:

$$\begin{cases} p|_{x=r} = P_r = P_c \\ p|_{x=b} = P_b \end{cases} \quad (7.26)$$

integrating Reynolds equation from reformation point r onwards up to the end of the conjunction (at the edge of the ring):

$$\frac{\partial p}{\partial x} = \frac{6\eta\Delta U}{h^2} + \frac{12\eta}{\rho h^3}\int_r^x \frac{\partial(\rho h)}{\partial t}\,ds + \frac{6\eta}{\rho h^3}C_3 \tag{7.27}$$

integrating again yields:

$$p = 6\Delta U\int_r^x \frac{\eta}{h^2}\,ds + 12\int_r^x\left[\frac{\eta}{\rho h^3}\int_r^s \frac{\partial(\rho h)}{\partial t}\,d\acute{s}\right]ds + 6C_3\int_r^x \frac{\eta}{\rho h^3}\,ds + C_4 \tag{7.28}$$

from the first boundary ($p|_{x=r} = P_r$):

$$C_4 = P_r \tag{7.29}$$

and using the second boundary condition ($p|_{x=b} = P_b$):

$$P_b = 6\Delta U\int_r^b \frac{\eta}{h^2}\,dx + 12\int_r^b\left(\frac{\eta}{\rho h^3}\int_r^x \frac{\partial(\rho h)}{\partial t}\,ds\right)dx + 6C_3\int_r^b \frac{\eta}{\rho h^3}\,dx + P_r \tag{7.30}$$

from which the integration constant becomes:

$$C_3 = \frac{(P_b - P_r) - \left[6\Delta U\int_r^b \frac{\eta}{h^2}dx + 12\int_r^b\left(\frac{\eta}{\rho h^3}\int_r^x \frac{\partial(\rho h)}{\partial t}ds\right)dx\right]}{6\int_r^b \frac{\eta}{\rho h^3}dx} \tag{7.31}$$

Therefore, if r, the location at which film reformation starts, is known, then C_3 will be obtained and the pressure distribution for the given region can be determined. So the aim is to determine the onset of reformation at point r.

The conjunctional outlet pressure P_b depends on the sense of piston motion, in the same manner as the inlet pressure P_a. However, constant C_3 can only be calculated if the film reformation position r can be determined. For this purpose, the conditions in the cavitation region must be considered.

7.3.3- The Cavitation Region $(c \leq x \leq r)$

In the cavitation region the pressure is assumed to be constant at the lubricant vaporisation pressure, P_c with the density of lubricant being a function of pressure and its bulk modulus (β) as:

$$\beta = \rho \frac{\partial p}{\partial \rho} \tag{7.34}$$

The ratio of density in the cavitated region to that in the full film region of the contact is defined as the film ratio, $\theta = \frac{\rho}{\rho_c}$, where lubricant density and viscosity vary with pressure and temperature.

As the result of constant pressures in the cavitation region, striated flow only proceeds in moderate to highly loaded contacts, mainly due to viscous shear (Couette flow). This means that the Poiseuille (pressure-induced) flow in Reynolds equation may be neglected in this region. Therefore, Reynolds equation can be altered to the form, initially proposed by **Elrod (1981)** in terms of θ as:

$$\frac{\partial}{\partial x}\left(\frac{\rho_c h^3}{6\eta} g\beta \frac{\partial \theta}{\partial x} - U\rho_c \theta h\right) = 2\frac{\partial(\rho_c \theta h)}{\partial t} \tag{7.35}$$

where:

$$p = g\beta \ln \theta + P_c \tag{7.36}$$

and $g\beta = \rho \frac{\partial p}{\partial \rho}$ is defined as switching term:

$$g = \begin{cases} 1 & \text{in the full film region} \\ 0 & \text{in the cavitated region} \end{cases} \tag{7.37}$$

in the cavitation region with viscous shear flow only:

$$\Delta U \frac{\partial(\theta h)}{\partial x} + 2\frac{\partial(\theta h)}{\partial t} = 0 \tag{7.38}$$

De la Cruz *et al* (2012) observed that the value of θ alters in the cavitation region according to the approach or separation of surfaces, as indicated by the second term in equation (7.38), where a negative value indicates approach of the surfaces.

Equation (7.38) is essentially a first order partial differential equation which can be solved using the method of characteristics. **Sawicki and Yu (2000)** show that:

$$(\theta h)_{x=c,t_c} = (\theta h)_{x=r,t_r} \tag{7.39}$$

where, t_c and t_r are the times at which film rupture and reformation occur.

at the film rupture point: $\theta_{x=c} = \theta_c = 1$, which using equation (7.39) leads to:

$$\theta_{x=r} = \theta_r = \frac{h_{c,t_c}}{h_{r,t_r}} \tag{7.40}$$

this, together with equation (7.36) fully describes the cavitation region of the flow. The only remaining unknown is the constant of integration C_3 in equation (7.31), which depends on the position at the onset of film reformation. Using the boundary conditions for the Elrod's equation (7.35), it follows that:

$$\begin{cases} p|_{x=r} = P_r = P_c \\ \left.\frac{\partial p}{\partial x}\right|_{x=r} = \frac{12\eta_r}{h_r^2}\left(\frac{U}{2} - \frac{dr}{dt}\right)(1-\theta_r) \text{ where } \theta_r = \frac{\rho_r}{\rho_c} \end{cases} \tag{7.41}$$

at the start of reformation region, r, this also must equate to the pressure gradient for the reformation region in Section 7.3.2, obtained as:

$$\frac{\partial p}{\partial x} = \frac{6\eta}{\rho h^3}\left(\rho U h + 2\int_r^x \frac{\partial(\rho h)}{\partial t}dx + C_3\right) \tag{7.42}$$

equating (7.41) and (7.42) and replacing for θ_r from (7.40) and after some basic manipulations:

$$C_3 = \rho_r h_r\left[\left(\Delta U - 2\frac{dr}{dt}\right)\left(1 - \frac{h_{c,t_c}}{h_{r,t_r}}\right) - U\right] \tag{7.43}$$

also replacing for C_3 in equation (7.31) enables the evaluation of the rupture point r from the equation below:

$$\left(\Delta U - 2\frac{dr}{dt}\right)\left(1 - \frac{h_{c,t_c}}{h_{r,t_r}}\right) = \Delta U + \frac{(P_b - P_r) - \left[6\Delta U\int_r^b \frac{\eta}{h^2}dx + 12\int_r^b\left(\frac{\eta}{\rho h^3}\int_r^x \frac{\partial(\rho h)}{\partial t}dx\right)dx\right]}{6\rho_r h_r \int_r^b \frac{\eta}{\rho h^3}dx} \tag{7.44}$$

7.4 Lubricant Rheology

The lubricant density (ρ) and viscosity (η) alter with pressure and temperature (T). The density variation with pressure and temperature in the full film region is given by **(Dowson and Higginson, 1959)**:

$$\rho = \rho_0(1 - \gamma\Delta T)\left[1 + \frac{m(p-P_{atm})}{1+n(p-P_{atm})}\right] \quad (7.45)$$

where, γ is the thermal expansion coefficient for the lubricant. It is usually considered to be around $6.4\times10^{-4}\ K^{-1}$ (**Yang et al, 2005, Khan et al, 2009** and **Morris *et al,* 2013**) showed that the rise in lubricant temperature occurs at the inlet to the contact by the contiguous surfaces, convecting into the bulk lubricant entering the contact domain. **Morris *et al* (2013)** also showed that the rise in lubricant temperature due to shear in the contact is only by a few degrees. Therefore, ΔT can be taken as the difference between the liner temperature and the bulk oil temperature measured from the engine sump (i.e. $\Delta T = T - T_0$). The liner temperature and that of the ring are assumed to be the same, although in practice the moving surface has a slightly higher temperature. The constants m and n are 6.0×10^{-10} and 1.7×10^{-9}, respectively. In the cavitation region, the density is obtained from equation 7.40 and the film ratio θ.

Lubricant viscosity alters with temperature more significantly than its density in moderately loaded contacts such as the ring-bore conjunction **Gohar and Rahnejat (2008)**:

$$\eta = \eta_0 e^{\propto^* p} \quad (7.46)$$

where:

$$\alpha^* = \frac{1}{p}(\ln\eta_0 + 9.67)\left[\left(\frac{T-138}{T_0-138}\right)^{-S_0}\left(1 + \frac{p-P_{atm}}{1.98\times10^8}\right)^{Z} - 1\right] \quad (7.47)$$

Z and S_0 are constants, independent of temperature and pressure:

$$z = \frac{\propto_0}{5.1\times10^{-9}[\ln(\eta_0)+9.67]},\ \ S_0 = \frac{x(T_0-138)}{\ln(\eta_0)+9.67},\ \ x = 0.04\ for\ SAE\ 10W40 \quad (7.48)$$

The temperature of the liner is used as already mentioned above.

7.5 Contact Load and Friction

Disregarding any ring elastodynamic behaviour, described by **Baker *et al* (2012)**, the instantaneous contact load is a quasi-static balance between the applied load to the ring and the contact reaction as already described in section 7.1. The applied forces include the ring tension force F_T which strives to return the ring to its unfitted state, as the result adhering it to the liner surface (Figure 7.1). Additionally, the chamber pressure acts behind the inner rim of the compression ring and acts outwards as the gas force F_G, also orthogonal to the contact surface :

$$W = F_e + F_g \tag{7.49}$$

It is assumed that 100% of the chamber pressure acts behind the compression ring, which fully conforms circumferentially to the liner surface with the footprint contact area of $A = 2\pi r_0(b-a)$, r_0 being the radius of an idealised liner of right circular cylindrical shape, and P_G is the chamber pressure. Therefore, as in equation (7.13):

$$F_g = AP_G \tag{7.50}$$

the ring tension force is:

$$F_T = Ap_e \tag{7.51}$$

where, the uniform elastic pressure p_e is (**Mishra et al, 2009, Bin Chick et al, 1966** and **Mishra et al, 2008**):

$$p_e = \frac{e_g EJ}{3\pi(b-a)r_0^4} \tag{7.52}$$

where, e_g is the end-gap of the incomplete circular compression ring in its free state. In the case studied here, $G \approx 8mm$, which reduces to 0.4 mm, when fitted into the cylinder.

The net applied force on the ring, towards the liner surface is balanced by the contact reaction, comprising the hydrodynamic load as the result of generated lubricant pressures and any direct contact of surface asperities, something which is not considered in the simplified solution in section 7.1. The hydrodynamic reaction is:

$$W_h = 2\pi r_0 \int_{x=a}^{b} p dx \tag{7.53}$$

Note that the low pressures in the cavitation and lubricant film reformation regions do not appreciably contribute to lubricant reaction. Therefore, the upper bound of the integral in equation (7.52) can readily be replaced by *c*.

A small area of asperity contact can occur in the compression ring-liner contact, particularly at piston dead centre reversals with low values of ΔU, thus low entrainment flow of lubricant into the conjunction. The area of asperity contact is a tiny fraction of the apparent contact area A, described above. If a Gaussian distribution of asperities is assumed, then the proportion of contact load carried by them may be obtained, using **Greenwood and Tripp (1971)** approach, where the asperity contact area and their share of carried load become:

$$A_a = \pi^2 (\zeta \kappa \sigma)^2 A F_2(\lambda) \tag{7.54}$$

$$W_a = \frac{16\sqrt{2}}{15} \pi (\zeta \kappa \sigma)^2 \sqrt{\frac{\sigma}{\kappa}} E' A F_{5/2}(\lambda) \tag{7.55}$$

The statistical functions $F_2(\lambda)$ and $F_{\frac{5}{2}}(\lambda)$ relate to the Gaussian distribution of asperities and are functions of the Stribeck oil film parameter, in this case: $= \frac{h_0}{\sigma}$, where σ is the root mean square roughness of the counterface surfaces. These functions can be represented by the fitted polynomial functions of λ and diminish as $\lambda \to 3$ (purely hydrodynamic condition) (**Teodorescu et al, 2005**):

$$F_2(\lambda) = -0.0018\lambda^5 + 0.0281\lambda^4 - 0.1728\lambda^3 + 0.5258\lambda^2 - 0.8043\lambda + 0.5003 \tag{7.56}$$

$$F_{5/2}(\lambda) = -0.1922\lambda^3 + 0.721\lambda^2 - 1.0649\lambda + 0.616 \tag{7.57}$$

The total contact reaction is, therefore:

$$W = W_h + W_a \tag{7.58}$$

As already mentioned, there are two contributing sources to conjunctional friction. Firstly, the reported literature shows that for most of the engine cycle, the dominant mechanism of friction is viscous shear of the lubricant. Secondly, in the regions of piston motion with low sliding velocity (at or in the vicinity of motion reversals), there is a lack of sufficient lubricant entrainment into the contact conjunction (low value of *U*). In these locations two other sources of friction play an important role. One is with an insufficient lubricant film thickness, leading to direct contact of counterface surface asperities (boundary lubrication). The combination of boundary and viscous friction leads to a mixed regime of lubrication. The other mechanism is pressure-induced viscous shear (Poiseuille shear), which occurs with a rise in pressure gradient across the conjunction ($\frac{dp}{dx}$). This can occur at piston reversals, particularly at the top dead centre and in transition from the compression stroke to the power stroke. All these sources of friction should be taken into account. For lubricant contributions:

$$f_v = \tau_v(A - A_a) \tag{7.59}$$

where:

$$\tau_v = \int_a^b \left(\frac{h(x,t)}{2}\frac{dp}{dx} \pm \frac{U\eta(x)}{h(x,t)}\right) dx \tag{7.60}$$

Note that the contributions to shear from cavitation and lubricant film reformation regions are negligible. Thus, the upper limit of the integral can readily be replaced by *c*.

The contribution due to asperity interactions occur over the area of asperity peaks A_a. There are two contributions in this case. One is due to adhesive friction of cold welded asperities under localised pressure (the second term on the right hand side of equation (7.61)). Here, the coefficient of asperity shear strength, ς is analogous to the coefficient of friction at the asperity-level contact (**Greenwood et al (1971)**) and

is usually measured through use of atomic force microscopy (AFM) in contact mode. The first term in equation (7.61) is based on the assumption that an ultra-thin film of lubricant is adsorbed to the asperity tips and undergoes non-Newtonian shear (**Greenwood et al (1971)**) at its limiting Eyring shear stress, τ_0 (**Eyring (1936)**).

$$f_b = \tau_0 A_a + \varsigma W_a \tag{7.61}$$

The asperity contacts can also cause elasto-plastic deformation, which affect boundary friction. These are not taken into account in the **Greenwood and Tripp (1971)** model, but are indirectly accounted for by direct measurement of ς . More comprehensive models for asperity level friction have recently been developed by **Kogut (2003)** and **Chong (2013)**.

The total friction is:

$$f = f_v + f_b \tag{7.62}$$

Therefore, the predicted friction (in this chapter) and that measured in chapter 6 can be compared.

7.5 Solution Method

The following solution procedure is followed:

Step 1:

At the initial crank angle (time), an initial value for the hydrodynamic pressure distribution enables calculation of the corresponding rheological parameters from Section 4. In addition, an initial value for the minimum film thickness, h_0 and squeeze film velocity, $\frac{dh}{dt}$ is assumed. These values are subsequently altered during the iteration process.

Step 2:

The pressure distribution is calculated.

Step 3:

The rheological properties of lubricant are updated based on the pressure distribution from Step 2. This step is repeated until the following convergence criterion is met:

$$\frac{\sum_{i=0}^{N}\left|p_i^{new}-p_i^{old}\right|}{\sum_{i=0}^{N}(p_i^{new})} < 10^{-4} \tag{7.63}$$

Step 4:

The final hydrodynamic pressure distribution is integrated over the entire contact area. The asperity load support is also calculated.

Step 5:

The net applied load is obtained from equation (7.49).

Step 6:

Instantaneous quasi-static equilibrium (at a given crank angle) demands that the following convergence criterion is satisfied:

$$\frac{|W-F|}{F} < 10^{-3} \tag{7.64}$$

otherwise, a new minimum film thickness value is calculated form:

$$h_0^{new} = h_0^{old}\left(1 + 0.075\frac{W-F}{F}\right) \tag{7.65}$$

Then Steps 2 to 6 are repeated unless:

$$\frac{|h_0^{new}-h_0^{old}|}{h_0^{new}} < 10^{-3} \tag{7.66}$$

If satisfied the calculations proceed to the next crank angle.

The calculation process continues until a periodic minimum film thickness variation is achieved for whole engine cycle.

7.6 Comparison of Predictions with Slider Rig Tests

The first step is to compare the results of predictions with the slider rig tests. The main aim is to understand the effect of coating, particularly the Ni-SiC coating, often used for the cylinder liners in motorsport applications, and also used in this thesis engine tests. The advantage of using the slider rig is to eliminate many "noise" factors, effects of which are difficult to include in any analytical predictions. These include thermal loading, vibrations, ring dynamics, to name but a few. Therefore, the analytical approach in modelling of slider rig need not be as complex as that highlighted in the preceding sections. The simpler long line contact method in section 2 is used here. The ring face-width profile is made to as close to a parabolic shape as possible. Therefore (see figure 7.1):

$$h_s = \frac{1}{2R}x^2 \tag{7.67}$$

where, the crown height of the ring is: $h_{rc} = h_s\left(x = \frac{b}{2}\right) = \frac{b^2}{8R}$. Therefore, the radius of curvature of the ring face-width can easily be determined for a given face-width and crown height.

The hydrodynamic load carrying capacity is obtained from equation (7.11). Viscous friction is obtained as:

$$f_v = \tau_v A = \left(\frac{\eta U}{h_0}\right) bl \tag{7.68}$$

therefore, the coefficient of friction due to viscous shear of the lubricant can be obtained as:

$$\mu_v = \frac{f_v}{W_h} = 2.45\left(\frac{R}{b}\right) \tag{7.69}$$

Note that a rectangular apparent contact area: $A = bl$ is assumed. In practice, the contact area is not exactly rectangular. However, the ring face has a parabolic shape and the asperities away from the centre of contact may never come into contact to each other from the opposing surfaces.

Therefore, it is important to calculate the area of the ring face from which the film ratio falls below the critical film ratio, λ_c. Considering the critical film ratio, the critical distance between ring and plate to be:

$$h_c = \lambda_c \sigma \tag{7.70}$$

If the portion of the height of the ring face-width from the floating plate falls below the critical distance is called, h_c, then one can state (see figure 7.2):

$$h_c - h_0 = \frac{1}{2R}\left(\frac{l_c}{2}\right)^2 \tag{7.71}$$

rearranging for l_c:

$$l_c = 2\sqrt{2R(h_c - h_0)} \tag{7.72}$$

therefore, the contact area at which there would be the possibility of asperity interaction from opposite surfaces at some positions would be:

$$A = l_c L \text{ and } f_v = \tau_v A = \left(\frac{\eta U}{h_0}\right) L l_c \tag{7.73}$$

it is apparent that if $h_c < h_0$ then, $W_a = 0$.

With such slider rigs' relatively low speed of lubricant entrainment, particularly in reciprocating motion, it is intended to simulate mixed or boundary regimes of lubrication, even if a significant layer of lubricant is provided on the surface of the floating plate ahead of the reciprocating contact. However, to ensure mixed or boundary lubrication, as well as repeatability for various test conditions, only a measured droplet of lubricant is supplied to the contact. Several strokes of the reciprocating head with the straight ring piece (strip) are undertaken for the droplet to be spread and form a thin surface film. Then, a fully flooded inlet condition ahead of the contact is assumed, which justifies the use of the above analysis.

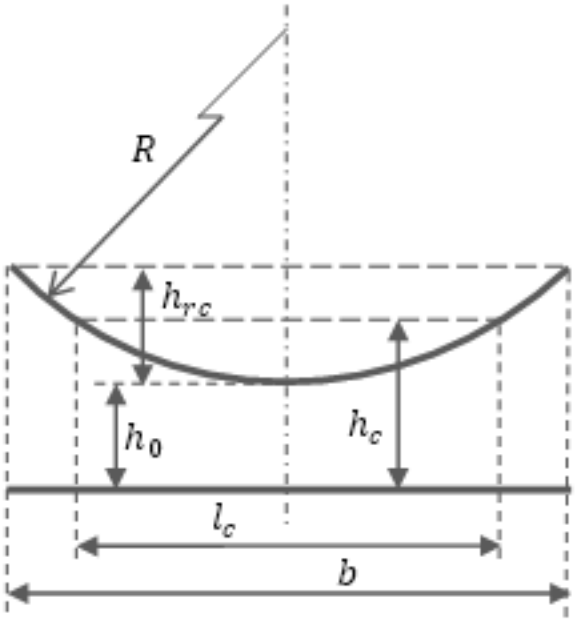

Figure 7.2: Determining the real contact width, l_c

The dominance of mixed regime of lubrication under these conditions means that boundary friction contribution must also be evaluated.

Load carried by the asperities is obtained, using equation (7.55) and the area of asperities involved by equation (7.54). However, the statistical function $F_{5/2}(\lambda)$ is based on the minimum gap, h_0. Therefore, not all the asperities within the contact area interact. Consequently, the contact area should be corrected to take this into account. The correction, however, must follow the variations of $F_{5/2}(\lambda)$ with λ. Variations of $F_{5/2}(\lambda)$ with λ is shown in Figure 7.3. $F_{5/2}(\lambda)$ is a statistical function for an assumed Gaussian surface (**Greenwood and Tripp, 1971**).

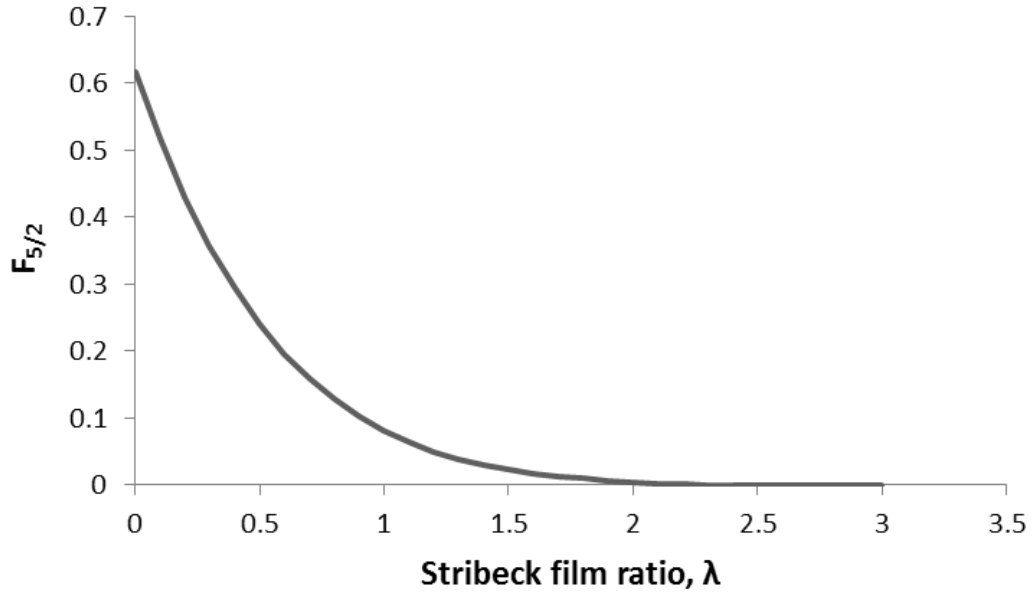

Figure 7.3: Variations of statistical function $F_{5/2}$ with Stribeck film ratio, λ

The load carried by the asperities is then more accurately given by equation (7.74) instead of equation (7.55):

$$W_a = \frac{16\sqrt{2}}{15}\pi(\xi\kappa\sigma)^2\sqrt{\frac{\sigma}{\kappa}}E^* \int F_{5/2}(\lambda)dA \tag{7.74}$$

where: $h_0 \leq h \leq h_c$ and: $dA = 2Ldx$, where as it can be seen in figure 7.2: $0 \leq x \leq \frac{l_c}{2}$, instead of the usual $0 \leq x \leq \frac{b}{2}$ for the entire parabolic face-width profile. Hence for: $h = \frac{1}{2R}x^2 : dh = \frac{x}{R}dx = \frac{\sqrt{2Rh}}{R}dx = \sqrt{\frac{2h}{R}}dx$ and thus: $dA = L\sqrt{\frac{2R}{h}}dh$, which can be substituted into equation (7.74), yielding:

$$\int F_{5/2}(\lambda)dA = L\sqrt{2R}\int_{h_0}^{h_c} F_{5/2}\left(\frac{h}{\sigma}\right)h^{-1/2}dh \tag{7.75}$$

or in terms of Stribeck's oil film ratio:

$$\int F_{5/2}(\lambda)dA = L\sqrt{2\sigma R}\int_{\lambda_0}^{\lambda_c} F_{5/2}(\lambda)\lambda^{-1/2}d\lambda \tag{7.76}$$

where, the limits of the integral are:

$$\lambda_0 = \frac{h_0}{\sigma} \quad \text{and} \quad \lambda_c = \frac{h_c}{\sigma} = 2.2239 \tag{7.77}$$

the integration yields:

$$\int F_{5/2}(\lambda)\lambda^{-1/2}d\lambda = \frac{2\sqrt{\lambda}}{3465}\{\lambda[\lambda(315(-0.0046)\lambda^3 + 385(0.0574)\lambda^2 + 495(-0.2958)\lambda + 693(0.7844)) + 1155(-1.0776)] + 3465(0.6167)\}$$

or:

$$\int_{\lambda_0}^{\lambda_c} F_{5/2}(\lambda)\lambda^{-1/2}d\lambda = \left\{\frac{2\sqrt{\lambda}}{3465}[\lambda(\lambda M - 1244.628) + 2136.8655]\right\}_{\lambda_0}^{\lambda_c}$$

where:

$$M = -1.449\lambda^3 + 22.099\lambda^2 - 146.421\lambda + 543.5892$$

therefore, the load carried by asperities can be recast as follows:

$$W_a = \frac{16\sqrt{2}}{15}\pi(\xi\kappa\sigma)^2\sqrt{\frac{\sigma}{\kappa}}E^*L\sqrt{2\sigma R}\left\{\frac{2\sqrt{\lambda}}{3465}[\lambda(\lambda M - 1244.628) + 2136.8655]\right\}_{\lambda_0}^{\lambda_c} \tag{7.78}$$

now, the same quasi-static load balance condition as previously is imposed:

$$W = W_h + W_a = F \tag{7.79}$$

where *F* is the applied contact load through the loading device head of the slider rig, described in chapter 5 (i.e. a known quantity). If the quasi-static load balance is not achieved, then the iterative procedure highlighted by equations (7.64) and (7.65) is followed.

With the load balance criterion satisfied, viscous and boundary friction contributions are determined. The former includes lubricant shear in the entire conjunction: $-\frac{b}{2} \leq x \leq \frac{b}{2}$.

thus:

$$f_v = \tau_v A = \frac{\eta U}{h_0} bL = L \int_0^b \frac{\eta U}{h(x)} dx = \eta UL \int_{-b/2}^{b/2} \frac{1}{h(x)} dx \tag{7.80}$$

replacing for the film shape $h(x)$ from equation (7.15) yields:

$$f_v = 2\eta UL \int_0^{b/2} \frac{1}{h(x)} dx = 2\eta UL \sqrt{\frac{2R}{h_0}} \tan^{-1}\left(\frac{b}{2\sqrt{2Rh_0}}\right) \tag{7.81}$$

Boundary friction is obtained through use of equation (7.61), where the total area of asperity summit contacts is given by equation (7.54). In equation (7.54), the statistical function $F_2(\lambda)$ is approximated by a 5th order polynomial as:

$$F_2(\lambda) = \begin{cases} -0.0018\lambda^5 + 0.0281\lambda^4 - 0.1728\lambda^3 + 0.5258\lambda^2 - 0.8043\lambda + 0.5003 & ; \text{for } \lambda \leq \lambda_c = 2.2945 \\ 0 & ; \text{for } \lambda > \lambda_c = 2.2945 \end{cases} \tag{7.82}$$

The variation of this function is shown in figure 7.4.

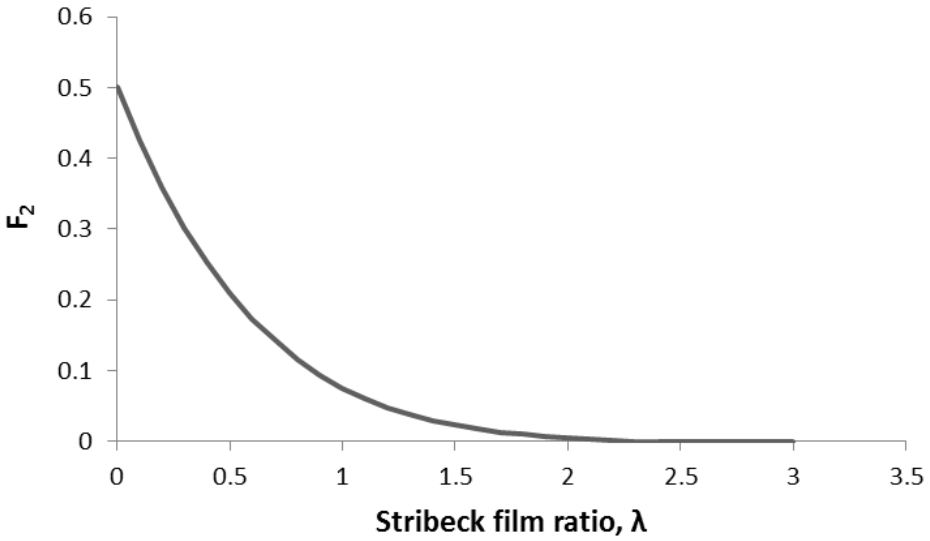

Figure 7.4: Variations of statistical function F_2 with Stribeck film ratio, λ

In the same manner as the load carried by the asperities, it is important to replace equation (7.54) with an accurate version which is based on the exact contact area and the critical gap h_c, thus:

$$A_a = \pi^2(\xi\kappa\sigma)^2 \int F_2(\lambda) dA \tag{7.83}$$

where: $h_0 \leq h \leq h_c$, $dA = 2Ldx$ and $0 \leq x \leq \frac{l_c}{2}$.

again note that: $h = \frac{1}{2R}x^2$, differentiating: $dh = \frac{x}{R}dx = \frac{\sqrt{2Rh}}{R}dx = \sqrt{\frac{2h}{R}}dx$, thus: $dA = L\sqrt{\frac{2R}{h}}dh$. Now replacing into equation (7.83) yields:

$$\int F_2(\lambda) dA = L\sqrt{2R}\int_{h_0}^{h_c} F_2\left(\frac{h}{\sigma}\right) h^{-1/2} dh = L\sqrt{2\sigma R}\int_{\lambda_0}^{\lambda_c} F_2(\lambda)\lambda^{-1/2} d\lambda \tag{7.84}$$

where the limits of this integral are the same as those for the statistical function $F_{\frac{5}{2}}(\lambda)$, previously stated.

the integration yields:

$$\int F_2(\lambda)\lambda^{-1/2}d\lambda = \frac{2\sqrt{\lambda}}{3465}\{\lambda[\lambda(315(-0.0018)\lambda^3 + 385(0.0281)\lambda^2 + 495(-0.1728)\lambda + 693(0.5258)) + 1155(-0.8043)] + 3465(0.5003)\}$$

or:

$$\int_{\lambda_0}^{\lambda_c} F_2(\lambda)\lambda^{-1/2}d\lambda = \left\{\frac{2\sqrt{\lambda}}{3465}[\lambda(\lambda N - 928.9665) + 1733.5395]\right\}_{\lambda_0}^{\lambda_c}$$

where:

$$N = -0.567\lambda^3 + 10.8185\lambda^2 - 85.536\lambda + 364.3794$$

therefore, the asperity contact area can be recast as follows:

$$A_a = \pi^2(\xi\kappa\sigma)^2 L\sqrt{2\sigma R}\left\{\frac{2\sqrt{\lambda}}{3465}[\lambda(\lambda N - 928.9665) + 1733.5395]\right\}_{\lambda_0}^{\lambda_c} \quad (7.85)$$

consequently, boundary friction contribution becomes:

$$f_b = \tau_0\pi^2(\xi\kappa\sigma)^2 L\sqrt{2\sigma R}\left\{\frac{2\sqrt{\lambda}}{3465}[\lambda(\lambda N - 928.9665) + 1733.5395]\right\}_{\lambda_0}^{\lambda_c} + \varsigma\frac{16\sqrt{2}}{15}\pi(\xi\kappa\sigma)^2\sqrt{\frac{\sigma}{\kappa}}E^* L\sqrt{2\sigma R}\left\{\frac{2\sqrt{\lambda}}{3465}[\lambda(\lambda M - 1244.628) + 2136.8655]\right\}_{\lambda_0}^{\lambda_c} \quad (7.86)$$

the total friction is obtained, using equation (7.62), thus:

$$f = 2\eta UL\sqrt{\frac{2R}{h_0}}\tan^{-1}\left(\frac{b}{2\sqrt{2Rh_0}}\right) + \tau_0\pi^2(\xi\kappa\sigma)^2 L\sqrt{2\sigma R}\left\{\frac{2\sqrt{\lambda}}{3465}[\lambda(\lambda N - 928.9665) + 1733.5395]\right\}_{\lambda_0}^{\lambda_c} + \varsigma\frac{16\sqrt{2}}{15}\pi(\xi\kappa\sigma)^2\sqrt{\frac{\sigma}{\kappa}}E^* L\sqrt{2\sigma R}\left\{\frac{2\sqrt{\lambda}}{3465}[\lambda(\lambda M - 1244.628) + 2136.8655]\right\}_{\lambda_0}^{\lambda_c} \quad (7.87)$$

the functions *M* and *N* are given above

Equation (7.87) requires the sliding speed of the straight ring relative to the floating plate, *U* (which is obtained by the encoder incorporated into the slider ring design), the geometry of the ring, physical mechanical properties of the contacting surfaces and their topography, as well as the boundary shear strength of the surfaces ς.

For the slider rig floating plate two specimens were prepared. One was uncoated steel, whilst the other was coated with approximately 20 µm of Ni-SiC. Both test pieces were ground on a centreless grinder. Note that a rougher surface results by centre-less grinding of the Ni-SiC coated surface. This is because Ni-SiC is a hard, wear-resistant coating compared with the uncoated steel specimen, which is more ductile and the surface material is more malleable.

Table 7.1 lists the data used in the analysis for both the floating plate and the SAE 10W-40 lubricant used.

Parameter	**Case I (Steel plate)**	**Case II (Nikasil coated plate)**	**Unit**
Ring material	Stainless steel 440C	Stainless steel 440C	-
Plate material	Steel	Steel with Nikasil	-
Ring material modulus of elasticity	200	200	GPa
Plate (coating) material modulus of elasticity	203	160	GPa
Ring material Poisson ratio	0.3	0.3	-
Plate (coating) material	0.3	0.23	-

Poisson ratio			
Ring face width	1.0	1.0	mm
Ring lateral length	30	30	mm
Ring face curvature radius	31	31	mm
Composite RMS surface roughness	0.126	0.346	μm
Roughness parameter $\xi\kappa\sigma$	0.659	1.56	-
Roughness parameter σ/κ	3.05e-5	1.20e-4	-
Pressure coefficient of boundary shear strength for plate material	0.22	0.26	-
Eyring shear stress	2.0	2.0	MPa
Lubricant density @15°C	833.0	833.0	Kg/m^3
Lubricant viscosity @20°C	0.17	0.17	Pa.s
Applied normal load on the ring	11.0	11.0	N

Table 7.1: Input data for the two studied cases

The pressure coefficient of boundary shear (**Teodorescu et al, (2004)** is obtained through use of an atomic force microscope, where a silicon tip is brought into contact with the specimen of the two plate type materials, treated to have the same topography as those used in the slider rig experiments. The tip was made to slide along the surface of the specimen at a constant speed and at various applied loads. Friction is obtained through calibrated readings of the trace. This was plotted against various contact force values. The slope of the graph provides the value of ς, since for dry contact sliding condition: $\varsigma = \frac{f}{W_a}$ (see equation (7.61)). The procedure for calibration of the AFM tip and measurements using lateral force microscopy (LFM) is detailed in **Styles et al (2014)**.

The speed of sliding is kept quite low in order to encourage mixed or boundary regimes of lubrication. The speed of the rotation of the reciprocating head's lead-screw was monitored by an encoder and converted to the sliding speed through pitch of the lead-screw. This is shown in figure 7.7.

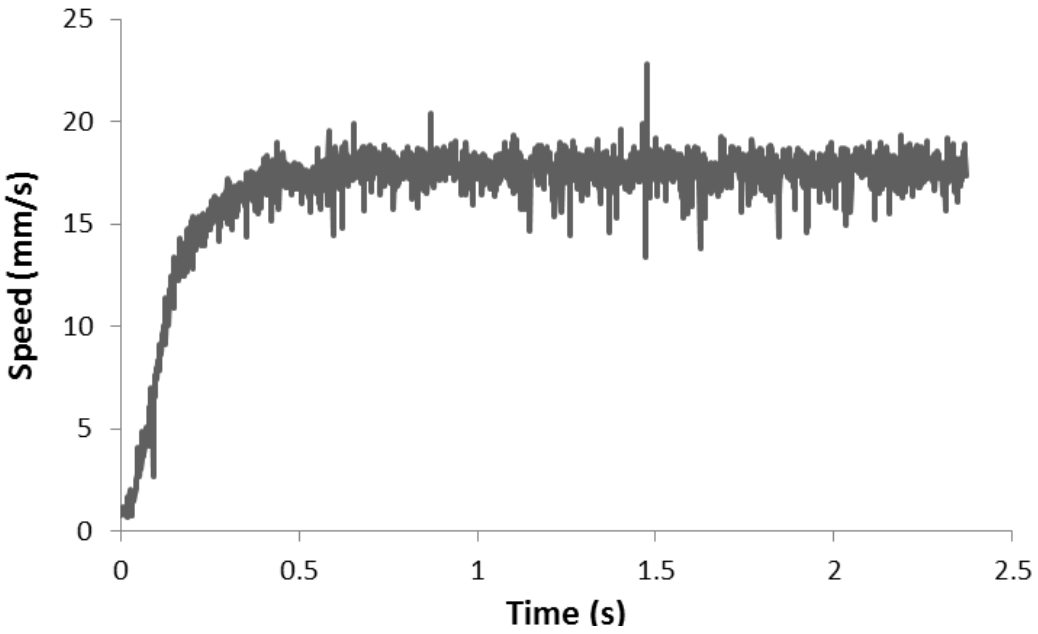

Figure 7.5: The measured sliding speed of the slider

After an initial accelerative phase, the speed of sliding was kept constant as far as possible. The "noise" resident on the measured signal is as the result of a combination of causes. One is the vibration of the driving motor, the other is the stick-slipping of the toothed belt drive system and finally there is some degree of backlash oscillations in the lead-screw at low speed operation. These were kept to a minimum through belt tension control and use of high precision lead-screw. There is also stick-slip in the contact zone due to intermittent asperity interactions (direct contact of surfaces).

The friction is measured by piezo-electric load cells place at either ends of the plate specimen, which is dragged by friction generated in the contact of the sliding strip with the plate. The plate rests freely upon a pair of bearings mounted in turn on the

machine bed. The drag of the plate is represented by its inertial force, which is equivalent to the applied force and bearing friction, being the contact friction, thus:

$$\sum F = -f = ma \tag{7.88}$$

Figure 7.6 shows the friction trace corresponding to the sliding motion of figure 7.7.

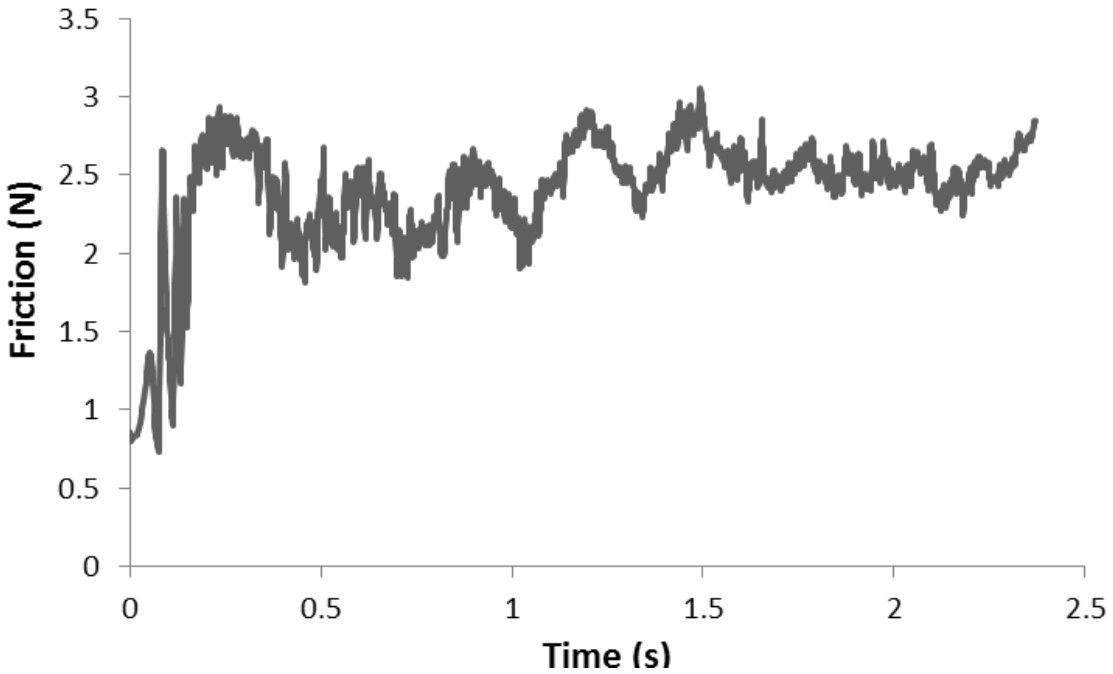

Figure 7.6: Measured friction of the slider rig contact for the Ni-SiC coated plate

Taking into account the applied contact load of 11N, the variation of coefficient of friction during the sliding motion is shown in figure 7.7. This shows an average value for coefficient of friction of μ=0.225, indicating that a mixed to boundary regime of lubrication. Note that for fluid film regime of lubrication, one would expect a value in the range 0.005-0.05.

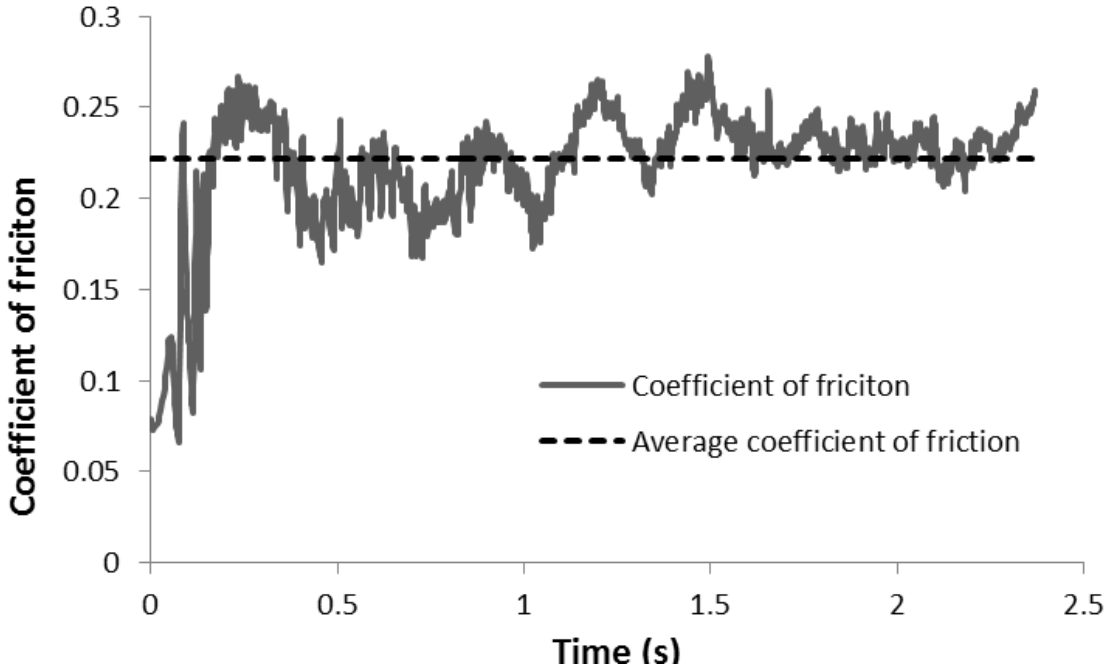

Figure 7.7: Measured coefficient of friction for the steel ring strip sliding against the floating plate coated with Ni-SiC

Before the analytical approach, highlighted above, can be safely used, it is necessary to establish that no contact deformation has occurred between the parabolic ring face-width profile and the flat plate. The dimensions of the contact are small compared with the principal radii of curvature of solids in contact (i.e. *R* of the ring profile and the nominally flat infinite radius of the plate). Thus, both the contacting surfaces may be considered as semi-infinite elastic half-spaces, justifying the use of Hertzian elastic line contact. The deflection is obtained as **Gohar and Rahnejat (2008)**:

$$\delta = \frac{F/L}{\pi E^*}\left\{1 + \ln\left[\frac{\pi E^* L^2}{2R(F/L)}\right]\right\} \tag{7.89}$$

where, the effective (or equivalent) modulus of elasticity of the counterfaces is:

$$\frac{1}{E^*} = \frac{1-\upsilon_1^2}{E_1} + \frac{1-\upsilon_2^2}{E_2} \tag{7.90}$$

This assumes that the coating thickness on any of the contacting surfaces is sufficiently thick that it can be considered as a semi-infinite solid. This is the case for the NiSiC coating which is 20-50µm thick.

Using the physical data provided in table 7.1, the localised elastic deflection becomes:

$\delta_S \cong 8.58\,\mathrm{nm}$ for the steel-on-steel contact and $\delta_N \cong 9.87\,\mathrm{nm}$ for steel-on-Ni-SiC surface. It is clear that no appreciable deformation takes place for the applied load. These deflections are far lower than the average film thickness of 0.7µm. Therefore, they are ignored as no EHL conditions exist.

Now equation (7.11) can be used with the input sliding speed variation from figure 7.5 to obtain the minimum film thickness variation for the two cases of coated and uncoated plates. This is shown in figure 7.8. It can be seen that a very thin film is predicted in both cases. Aside from the initial accelerative phase, a fairly flat film is predicted with slightly higher thickness in the case of Ni-SiC coated substrate. The regime of lubrication can be ascertained by plotting the predictions in the form of Stribeck oil film parameter. This is shown in figure 7.9.

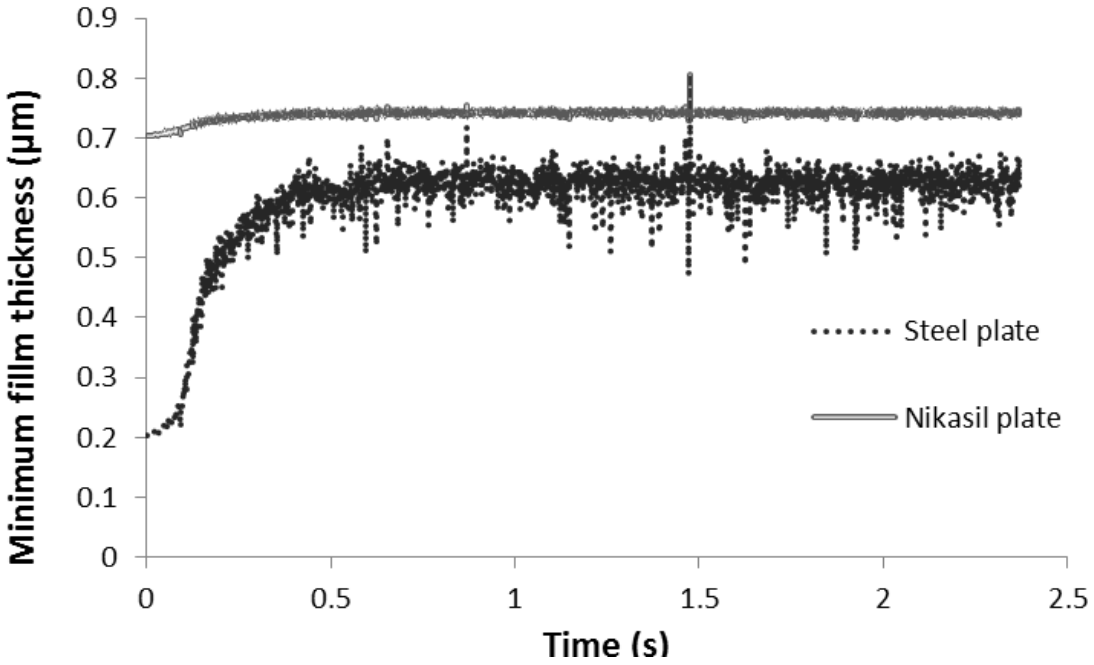

Figure 7.8: Minimum film thickness variation for uncoated and coated ring strip-plate contact during the prescribed sliding motion

Note that the critical value of the Stribeck's oil film parameter; $\lambda_c = 2.3$, below which value mixed or boundary regime of lubrication is indicated. This critical value is shown in figure 7.9. Since the uncoated steel plate has a superior honed surface post centre-less grinding, it is clear that the Stribeck oil film parameter remains above its indicated critical value. This means that a hydrodynamic regime of lubrication should be prevalent. For the case of Nikasil (Ni-SiC coating), the Stribeck parameter remains close to its critical value, thus a mixed regime of lubrication is expected.

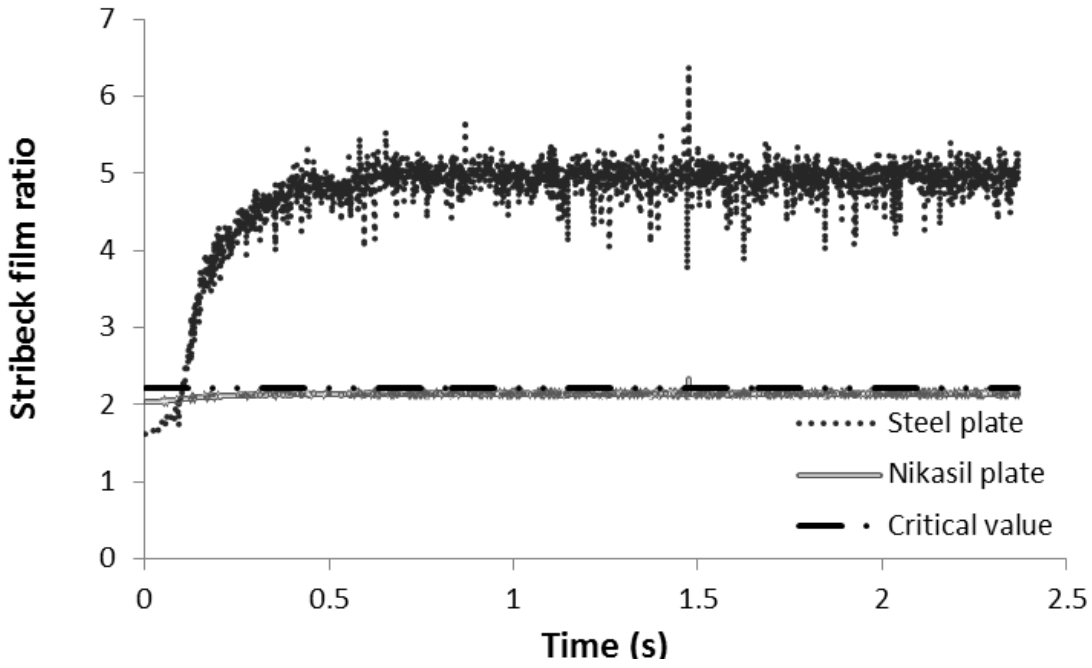

Figure 7.9 : Calculated regime of lubrication for the cases studied with the slider rig

The predicted load carrying capacity equates the applied load. If the predictions in figure 7.9 were to be upheld, then the contributions to the load carrying capacity from boundary and viscous friction should show that in the case of steel plate the contribution is entirely due to hydrodynamic pressures. In the case of Ni-SiC coating there must be a significant portion of predicted load carried by the asperities. Figures 7.10 and 7.11 confirm this supposition.

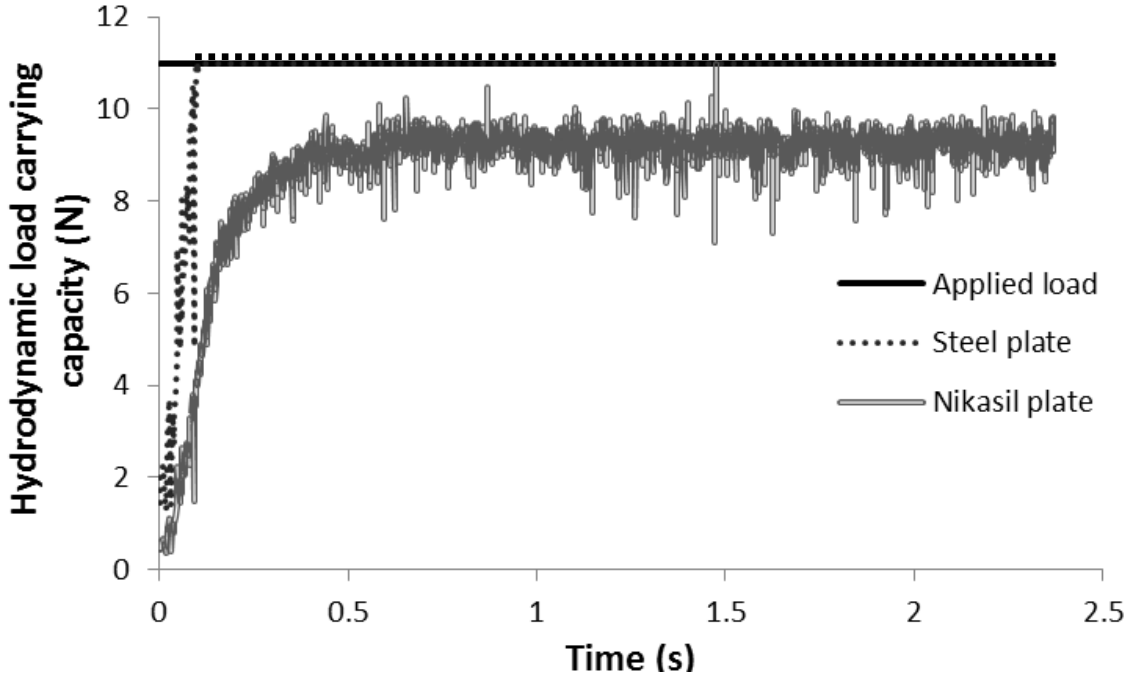

Figure 7.10: Predicted hydrodynamic reaction

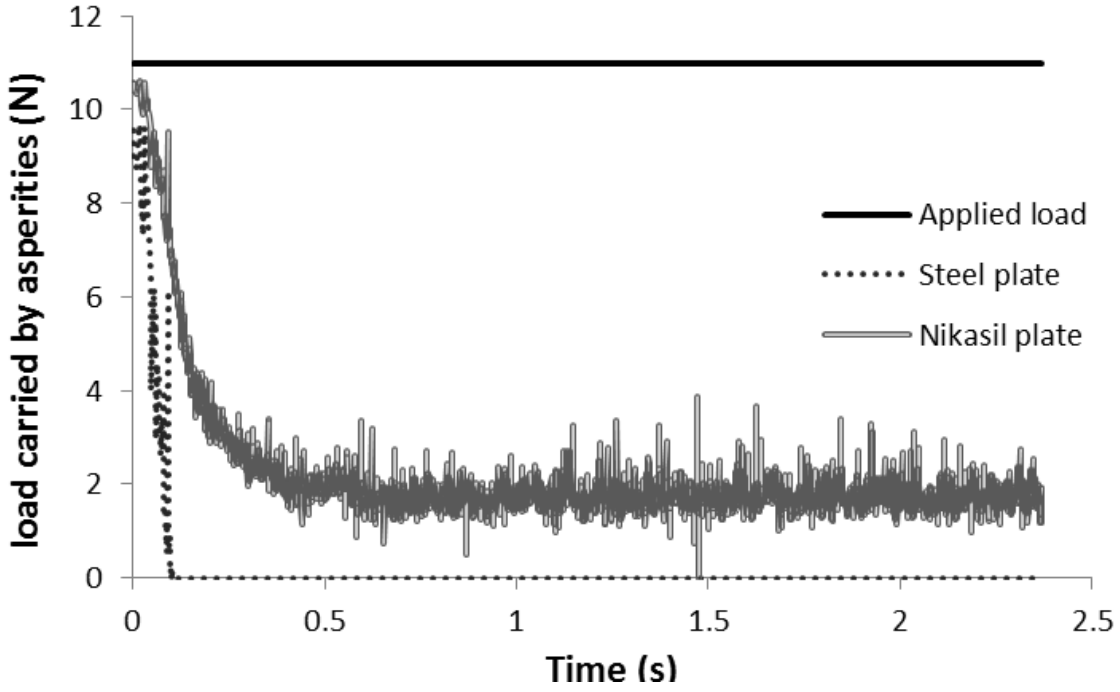

Figure 7.11: Predicted load share of asperities (boundary interaction)

In the case of the steel plate the entire load is supported by the hydrodynamic reaction whereas in the case of the Nikasil plate a combination of hydrodynamic and boundary reaction supports the load, hence a mixed regime of lubrication exists (see load shapes in figure 7.10 and 7.11). This is partly because of the rougher Nikasil surface, owing to the grinding process and the hard brittle nature of Nikasil when compared with steel and partly because of the higher shear strength of the Nikasil. The repercussion is that even if nominally identical topography could be achieved under boundary regime of lubrication there would be higher adhesive friction with Nikasil than steel. However, the wear resistance of the former would be superior.

There are a number of implications of these findings. Firstly, more defined topography with valleys and plateaus may be achieved with Nikasil than the more ductile steel. Surface modifications are usually carried out by cylindrical grinding/honing which is more suitable to hard and brittle material. With ductile material, sharp features are difficult to produce and in many cases require further finishing operations in order to remove any excess protruding features. This means that for cross-hatch honed cylinder liners, Nikasil coating would be an advantage, which has been shown by **Howell-Smith (2010)**. Secondly, with smoother surfaces, when boundary interactions occur, there would be larger number of lower “amplitude” asperities and as the boundary friction equation shows, this can be quite detrimental in terms of boundary friction. Thirdly, wear and friction do not always act in concert. Hard wear resistant coatings reduce the chance of wear, but may exhibit larger friction. Finally, there may be a possibility that coatings such as Nikasil act in an oleophobic manner, although this is not investigated here.

Friction is not significantly increased with use of Nikasil of even rougher topography than the parent steel substrate as figure 7.12 demonstrates.

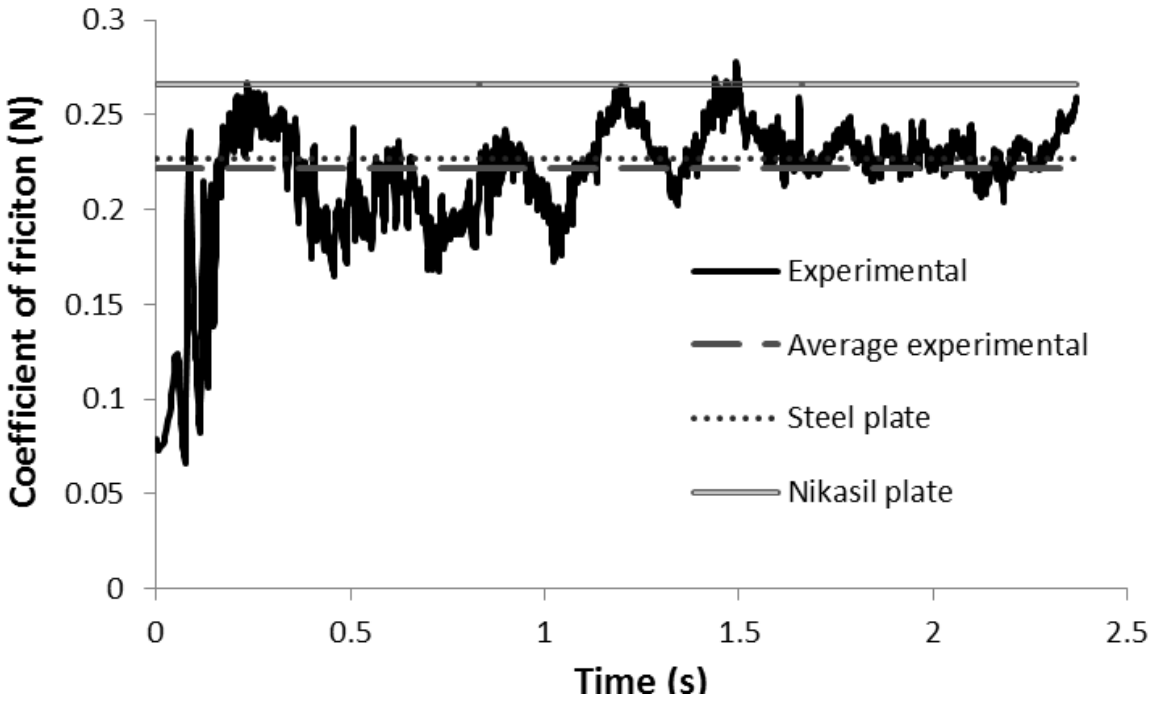

Figure 7.12: Coefficient of friction variation (experimental Vs numerical)

The relatively high coefficient of friction for the steel plate may indicate non-Newtonian shear of quite a thin film.

An important aspect of this analysis is the validity of rather simple analytical method as opposed to the usual detailed and time consuming numerical analysis.

7.7 Comparison with Engine Test Results Using the Floating Liner

The results of various engine testing, employing the floating liner are provided in chapter 6. Here the analytical model described in sections 7.3-7.6 is used to make friction predictions under the same conditions as a sample of experimental measurements. This serves two purposes. Firstly, the combined experimental measurements and numerical predictions enable determination of regime of lubrication and friction generation with a greater degree of confidence, which is a prelude to any practical conclusions with regard to system development. Secondly,

the combined study would point to the validity of the assumptions made in both numerical analysis and processing of measurement data.

The studied case is at the speed of 3000 rpm under motored condition. This is chosen to avoid repeating the set of results of experimental measurements already presented in chapter 6. Furthermore, no significant differences are noted between running conditions (motored) between 2000-4000 rpm as the input loading and contact kinematics largely result in similar regimes of lubrication. Motored, as opposed to fired engine conditions, are used here because contributions of ring-pack and piston skirt to the overall piston-cylinder system can be ascertained by using an slightly *over-sized* piston (thus a lower nominal piston-liner clearance) than that used in practice (i.e. a skirt clearance of 50µm). This enables removal of the compression ring (note that Honda CRF 450R has a compression ring and an oil control ring only). Furthermore, as already shown in chapter 6 the compression ring acts more effectively under fired conditions at TDC reversal, although with chamber pressure it also acts under motored condition well, but to a lesser extent (pressure in the order of 20bar exists under motored conditions). Therefore, motored conditions are preferred for this combined experimental-numerical approach. Without the compression ring, the skirt and oil control ring conjunctions are likely to be subjected to a flooded inlet. This is fortuitous since the analytical approach is based on such an assumption as well.

The important input parameters for the hydrodynamic analysis are contact kinematics, contact load and lubricant rheology, as already described in section 7.3. Figure 7.13 shows the measured cylinder pressure for the motored engine speed of 3000 rpm. Fortunately, with the Honda CRF 450R, the chamber pressure reaches a maximum value of 20bar at the top dead centre without cylinder firing (Figure 7.13). This is quite representative of chamber pressure for fired condition at 30% throttle at the same engine speed of 3000 rpm, and has the added advantage of eliminating other phenomena under fired conditions, such as piston and liner thermo-elastic distortion. Under motorised conditions the maximum chamber pressure occurs at the

TDC reversal, as opposed to the fired condition where spark ignition takes place within the power stroke after the TDC. A difference can be noted between the chamber pressure with and without the compression ring because of its sealing effect at the TDC.

Additionally, surface topography of the counterfaces and boundary parameters are also measured and listed in table 7.2.

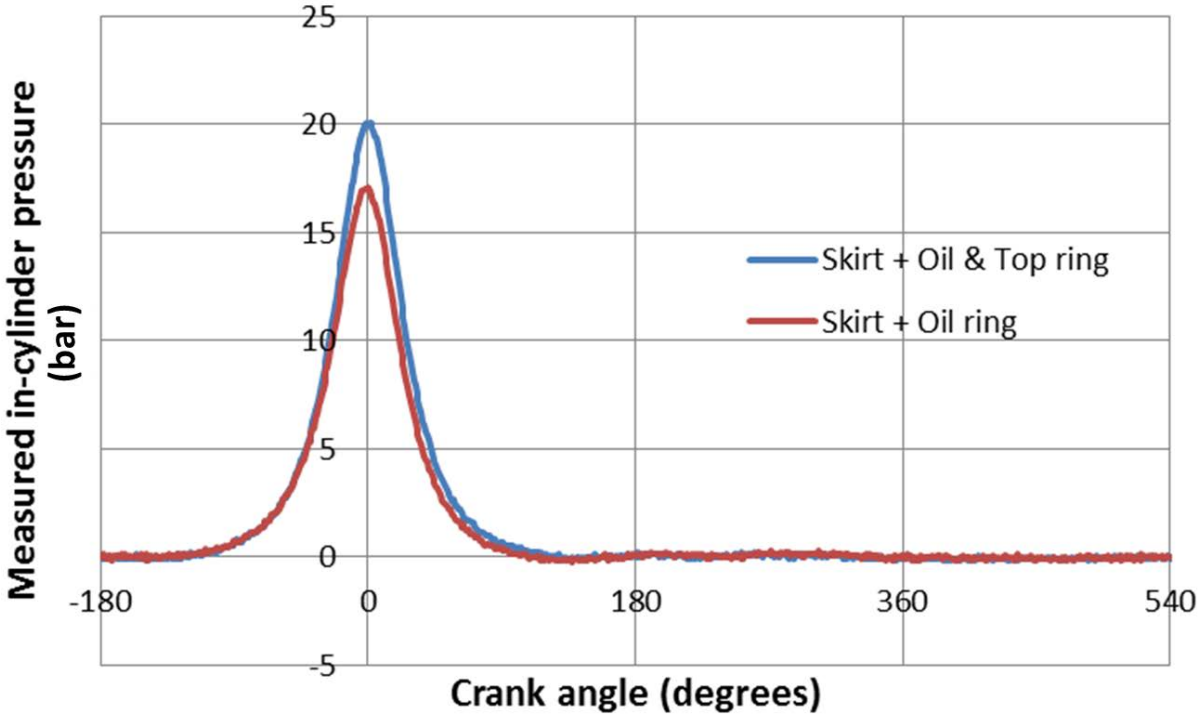

Figure 7.13: Cylinder chamber pressure for motored engine at 3000 rpm

Parameter	Value	Unit
Engine speed	3000	rpm
Connection rod length	107	mm
Engine stroke	62.1	mm
Liner material	Steel	-
Bore nominal radius	48	mm
Top ring	Steel	-
Liner Elasticity Modulus	203	GPa
Liner Poisson ratio	0.3	-
Ring Elasticity Modulus	203	GPa
Ring Poisson ratio	0.3	-
Ring end gap	7.92	mm
Ring face width	0.72	mm
Pressure coefficient boundary shear strength	0.22	-
Rq for liner surface	0.515	μm
Rq for Ring surface	0.201	μm
Combined roughness parameter (ηβσ)	0.0771	-
Combined roughness parameter (σ/β)	0.211	-
Operating temperature	25	°C
Oil density	833.8 (@15°C)	kg/m^3
Oil viscosity	50 (@40°C)	mPa.s
Pressure-viscosity coefficient	1×10^{-8}	-
Temperature-viscosity coefficient	0.04	-

Table 7.2: List of engine specification and analysis data

Figure 7.14(a) shows the measured friction using the floating liner. The changes of sign in friction represent piston reversals. The gap between the two traces constitutes the frictional contribution of the compression ring. The results show that the main contribution to friction in the case of this engine set up and running

conditions is due to the piston skirt. It should be noted that at higher temperatures thermo-elastic distortion of the piston skirt would result in a larger clearance and reduces the skirt's proportion of frictional contribution (i.e. an increased proportion due to the compression ring). For the test conditions reported here (Table 7.2), the compression ring friction contribution is approximately 10-15% of the total. Since the conditions with or without the compression ring in place are not identical and there is a certain amount of *noise* resident on the friction traces, the signals cannot reliably be subtracted.

Figure 7.14(b) shows the predicted friction during an engine cycle under the same conditions as those in Figure 7.14(a). The variations in the sliding velocity are also shown in the figure. The first thing to note is that friction variation is directly proportional to the sliding velocity (i.e. $f \propto U$), indicating that Couette shear of the lubricant film is the dominant responsible mechanism for friction (see second term on the right-hand side of equation (7.60)). This proportionality is lost in the region of rising chamber pressures prior to the TDC and proceeds further into the initial stages of intake (corresponding to the power stroke in a fired engine). In this region Poiseuille shear of the lubricant is more dominant (first term on the right-hand side of equation (7.60)). Only in a very small part of the aforementioned compression-to-intake region some asperity interactions occur.

Figures 7.14(c) and 7.14(d) show compression ring-liner friction contributions in two regions. One region is in the compression part of the cycle, prior to the TDC reversal at crank angle of 0° and the other is in the early stages of the intake stroke post the same TDC reversal. An average friction value for each highlighted crank angle region is calculated from measurements and predictions.. These are shown in Figures 7.14(c) and 7.14(d). Reasonably goods agreement is found. The differences can be as the result of many parameters. These may include some of the assumptions of the analytical method used, such as ring-liner circumferential conformity, a right circular cylindrical bore, assumed isothermal conditions and a fully flooded conjunctional inlet. On the experimental side the presented results are

average of many cycles, where there are small variations (1-2%) in chamber pressure. Nevertheless, there is good agreement.

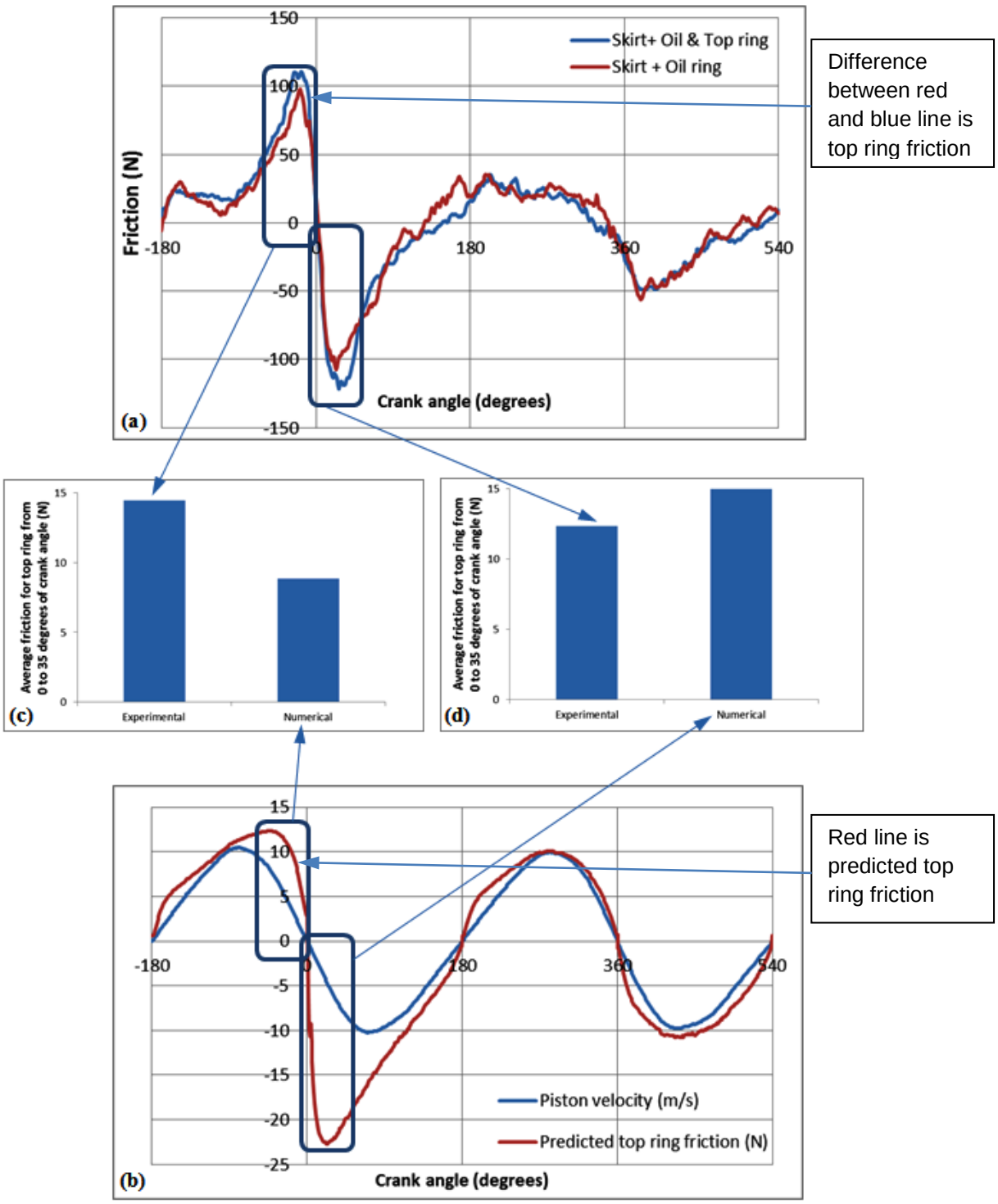

Figure 7.14: Comparison of measured and predicted ring-liner friction

7.8 Closure

Direct *in situ* measurement of in-cylinder friction, using a devised floating liner and analytical predictions have been combined to provide explanations for the transient regime of lubrication as well as the prevalent mechanisms for generation of friction throughout an engine cycle. It is shown that with a slightly over-sized piston, it is possible to remove the compression ring in the single cylinder motocross motor-cycle engine. The difference in cyclic frictional traces with and without the presence of the compression ring provides an assessment of in-cycle friction contributed by the compression ring. An analytical predictive method, based on Elrod's modification to Reynolds equation, taking into account the effect of cavitation is presented. Predicted viscous friction using this approach, supplemented by boundary friction as the result of asperity interactions show good agreement with measurements. Both predictions and measurements show that the contribution of the compression ring is most significant in the high pressure part of the engine cycle and at top centre reversal. This indicates that the compression ring complies with its primary sealing function. Viscous friction of the lubricant dominates under the tested and simulated isothermal motored conditions. These are in fact representative of idle to low speed cycling in creeping traffic with a *cold* engine (conditions which typically form a part of steady state New European Drive Cycle; NEDC for emission testing). Under these conditions, as shown here, the effectiveness of compression ring sealing is somewhat reduced on account of reduced chamber pressures, thus a greater level of emission is surmised.

Chapter 8

Conclusion and Suggested Further Work

8.1 Overall Conclusions

The overall conclusions of the research are:

- A significant portion of the in-cylinder friction takes place at the top-dead-centre reversal in the transition from the compression to power stroke.
- Under motored conditions, because of lower in-cylinder pressure the frictional characteristics at the top-dead-centre appear to follow Poiseuille friction. This is due to significant pressure gradient change at the top of the compression stroke.
- Under fired engine conditions a greater pressure acts behind the compression ring in the same top-dead-centre reversal. This is as the result of the effective sealing action of the compression ring. A sharper change in friction is therefore noted than in the case of motored conditions during this reversal which with combined numerical analysis indicates the presence of mixed and/or boundary regime of lubrication.
- Elsewhere under both fired and motored conditions the frictional characteristics follow in direct proportion to the piston sliding velocity. Therefore, the dominance of viscous friction is ascertained.
- The significant proportion of friction at the top-dead-centre in transition between compression to power strokes indicate that any palliative action to mitigate friction is best directed to this locality (see figures 6.4, 6.5, 6.6 and 7.14). This palliation can take the form of surface modification, particularly using laser surface texturing or through surface indentations. These form

dimples, chevrons or similar cavities which may be introduced onto the surface of the cylinder liner (**Rahnejat (2006)**) or alternatively on the flat land of the compression ring (**Etsion et al (2005)**).

- One repercussion of the findings of the thesis is that there would be no need to introduce surface modification elsewhere on the surface of the cylinder liner as both experimental and numerical predictions show the dominance of lubricant viscous shear. This means that introduction of surface modification on the cylinder liner would be preferable to the ring, particularly that an increased retained volume of lubricant in areas with cross hatch honing can lead to blow-by, oil loss and lubricant degradation (due to loss of compression ring sealing function).
- Good comparison is noted between measurements and analytical one-dimensional predictions. However, a comparative numerical-experimental study was not the primary aim of the thesis. On the contrary, the primary aim was the fundamental understanding of mechanisms of friction generation through a combined numerical-experimental investigation.
- At the basic science level the comparison of the slider bearing rig measurements with the same numerical method show that a lubricant film of insufficient thickness is formed and that for such conditions (not atypical of ring reversals) the dominant regime of lubrication is boundary interactions. This means that hard wear-resistant, low friction coatings may also be suitable candidates for the reduction of friction.

The combined experimental measurements and the analytical predictions have resulted in many findings including those listed above.

8.2 Achievement of Specific Objectives

The research aims and objectives, set out in chapter 1, were achieved as described below:

- Develop means of accurate measurement of in-cylinder friction via development of a fully instrumented floating liner:

  A floating liner was developed to directly measure the in situ in-cylinder friction under various test conditions, ranging from open cylinder head configuration to engine motored and fired conditions. The floating liner was based on an initial design by **Howell-Smith (2010)**. This was modified as reported in chapter 5, manufactured and calibrated, before use in engine testing.

- Develop an appropriate engine test-bed for testing of high performance motocross engines

  An industry-standard engine test bed, based on a single cylinder Honda CRF 450R motocross motorbike engine was existing as the part of previous research by **Howell-Smith (2010)**. However, a large amount of modifications to the test bed was required. This was necessary, because the current thesis was a part of a large EPSRC Program Grant, under which surface modification work was to be developed to ideally reduce frictional losses from the piston-cylinder interactions. As any reduction in friction was expected to be of the order of few percent, repeatable test conditions were critical to the research undertakings. Therefore, repeatable test conditions required significant alteration to instrumentation, both within the engine and in the test cell environment. Measurement of many parameters were required as well as suitable methods of data acquisition and processing, in addition to repeatable and representative test procedures. These were all achieved and reported in this thesis.

- Recording all operating parameters such as engine speed with sufficient resolutions necessary to demonstrate exact in-cycle conditions

  These points are all addressed in chapter 5, including a considerable amount of data regarding surface topographical measurements and assessment of suitable parameters.
- Create an analytical/numerical model to predict film thickness variation and friction in the ring-bore conjunction

  Simply measuring in situ cylinder friction does not lead to the determination of the regime of lubrication and fundamental understanding of mechanisms of friction generation. Ideally, a combined analytical-experimental approach is required. The coincidence of the findings of analytical predictions with independent experimental work is the basis of a scientific approach to research undertakings. This is the approach adopted in this thesis. Hence, an analytical model is developed within the thesis. The model is analytical, thus computationally efficient. Whilst, it is rather simple compared with more complex numerical routines, it takes into account many salient practical features for the intended purpose and has shown very good conformance to the experimental findings.

- Integrate the above combined experimental-numerical study to determine the transient nature of the compression ring-bore conjunction

  The analytical predictions and experimental measurements have been carried out both at the basic science investigation with a specially designed and manufactured precision slider bearing rig and with the engine test bed. The combined studies have highlighted the transient nature of friction mechanisms and pointed to methods of palliation for future work. Additionally, good agreement has been found between predictions and measurements in all cases.

8.3 Contributions to Knowledge

There are a number of elements, constituting contributions to knowledge in this thesis. These are:

- Direct measurement of in-situ in-cylinder friction has resulted in fundamental understanding of the transient nature of the regime of lubrication and attribution of the measured friction to these regimes under various engine running conditions. Although floating liners have been developed and used by a number of authors, cited in the review of literature, most of these investigations have been rather empirical in nature. They have not attributed, in a fundamental manner, the observed frictional characteristics to the prevailing regime of lubrication. The combined analytical-experimental approach in this thesis deals with this important issue in a fundamental manner.

- The development of the floating liner itself has been carried out without the use of spring-damper elements at the top of the liner as has been usual in order to guard against liner vibration under any form of impulsive loading. A labyrinth seal is employed instead in a design, described in chapter 5, which enables minimum pressure leakage and support structure which inhibits the effect of vibration and shock loading. Modal characteristics of the liner, whilst *in situ* and material composition have been carefully selected to avoid structural instabilities. Altogether, a fundamental scientific rigour is applied in the design and development of the floating liner, which is not evident in literature reporting similar objectives.

- The operational integrity of the floating liner is fundamentally ascertained through a series of various configuration testing, including open cylinder head and use of Newtonian-Eulerian dynamics. Then, a systematic move to motored and pressurised configuration is undertaken and onto realistic fired engine conditions. This systematic stepwise approach imparts a degree of confidence in the acquired results, which is not noted of other reported studies.

- Friction measurements have been carried out up to engine speed of 4000 rpm in a short stroke high performance engine, under fired condition with wide open throttle, rendering contact forces of the order of 5kN with maximum piston speed of 20m/s. Direct friction measurement under such conditions have not hitherto been reported in literature.

- An analytical 1D solution including the effect of lubricant film rupture, cavitation and film reformation has been developed with realistic inlet and outlet boundary conditions. It also includes the effect of asperity interactions with appropriate surface topographical parameters for plateau honed surfaces, ascertained through determination of liner wear characteristics. Although, the analytical model is one dimensional and thus ignores the effects of bore out-of-roundness and thermo-elastic deformation of the piston and skirt lubrication, as well as compression ring's modal behaviour, it provides a very comprehensive and practical approach to conditions experienced in practice with a floating liner rig. It includes the inclusion of surface parameters which are often surmised, not measured accurately in the reported literature. The good agreement of the prediction with experimental data is a good indication of the scientific basis of the analytical method. The model is also very computational efficient, both in terms of execution time and storage requirements.

- Ni-SiC hard wear-resistant coatings are often used for aluminium-based high performance engine cylinders, such as in the motorsport or niche OEM. The performance of such coatings is essential under mixed or boundary regimes of lubrication, both in terms of friction and wear. A precision slider bearing rig is designed and built as an integral part of this thesis and for use for other sister research projects under the EPSRC Encyclopaedic Programme Grant. Using this rig, combined with the analytical tool the regime of lubrication and coating performance of Ni-SiC (commonly referred to as Nikasil) has been ascertained.

Finally, the thesis highlights a robust infrastructure developed for use in many future research projects from fundamentals of friction to engine applications.

8.4 Suggested Further Work

The developed infrastructure provides a number of opportunities for further research at Loughborough University. There are also other general opportunities to build upon the findings reported in this thesis. At the specific level, concerning the developed infrastructure, the following further work is suggested:

- At the basic science level the thesis has developed a slider bearing rig, this slider bearing rig can be used with a combination of coatings as shown but can be used for more representative cross hatch honed plates and testing of different laser textured patterns. This action has already been undertaken by Nicholas Morris at Loughborough University.
- Various coatings can be used for the same plates with boundary friction coefficients measured by AFM, using the same model outlined in chapter 6.
- One of the shortcomings of the test engine is the lack of temperature distribution measurements along the liner and piston skirt. A dry tall sump engine has designed by the author and is being manufactured for use in another PhD thesis which allows direct access data acquisition. Therefore, pressure traces obtained from the model can be built upon with the use of these temperature distributions.
- The floating liner surface can be coated with different coatings, similar to those reported in the usual liner configuration by **Howell-Smith (2010)** or laser etched at the TDC reversal in order to obtain the effects of coating and/or laser etched patters and geometry more directly than that reported by **Howell-Smith (2010)**.
- The emphasis of this PhD thesis has been on a combined numerical-experimental study. However, the model can be extended into 2D, allowing bore out of roundness to be added as in **Rahmani (2012)**.
- The procedure outlined for assessment of wear and its relationship to appropriate surface topographical parameters for different surfaces can be used to select the right parameter for predictive analysis. For instance, during the running-in wear, it is necessary to use the parameter R_{pk} to represent the

peakiness of surfaces, whilst for a run-in plateau-formed liner, it would be more appropriate to use the plateau roughness, R_k. These are salient points which are often ignored in numerical analysis.

References

Akalin, O., Newaz, G.M,. (1998) “A new experimental technique for friction simulation in automotive piston ring and cylinder liners” SAE Paper 981407.

Akalin O and Newaz G M (2001), Piston Ring-Cylinder Bore Friction Modelling in Mixed Lubrication Regime: Part 1 – Analytical Results, Journal of Tribology, Vol. 123 211-218

Balakrishnan, S., (2002): Transient elastohydrodynamic analysis of piston skirt lubricated contact under combined axial, lateral and tilting motion PhD Thesis Loughborough University, Loughborough, UK

Baker, C.E., Theodossiades, S., Rahnejat, H. and Fitzsimons, B., (2012) “Influence of In-Plane Dynamics of Thin Compression Rings on Friction in Internal Combustion Engines”, trans. ASME, J. Engng. for Gas Turbines & Power, 134, 2012, 092801-1

Bai, D. (2102): Modelling Piston Skirt Lubrication in internal Combustion Engines. PhD Thesis MIT 2012

Barrow, J.D. (2002). “The Book of Nothing: Vacuums, Voids, and the Latest Ideas about the Origins of the Universe”. Vintage Series. Vintage. p. 70. ISBN 9780375726095. LCCN 00058894.

Barus (1893) “Isothermal, Isopiestics and Isometrics relative to Viscosity”. American Journal of Science, Volume 45, pp. 87.

Bard Kathryn A. “Encyclopedia of the Archaeology of Ancient Egypt” 1999, ISBN 0-203-98283-5

Bin Chik, A. and Fessler, H., “Radial pressure exerted by piston rings”, J. Strain Anal., I (2), 1966, pp. 165-171

Bolander, N.W., B.D. Steenwyk, F. Sadeghi and G.R Gerber (2005) “Lubrication regime transitions at the piston ring-cylinder liner interface”, J of Engineering Tribology, Proc. ImechE., 219:19-31.

Bromley, A. G. (1990). "The Antikythera Mechanism". Horological Journal 132: 412–415.

Cameron, A.,(1952) “Hydrodynamic lubrication of rotating discs in pure sliding. A new type of film formation”. J. Inst. Petrol. 37, p. 332, 1951: AMR 5.

Cameron, A. (1970): “Basic Lubrication Theory”. Longmans Group Ltd., London, ISBN 0-582-44479-9.

Chong, W.W.F., Teodorescu, M. and Rahnejat, H., “Nanoscale elastoplastic adhesion of wet asperities”, Proc. IMechE, Part J: J. Engng. Trib., 2013, doi: 10.1177/1350650112472142

Codex Atlanticus, (1478-1519) by Leonardo da Vinci, currently stored at Biblioteca Ambrosiana, Milan.

D’Agostino L., della Valle S., Ruggiero A. and Senatore A. (2002) “A study on the piston top ring lubrication using open-end boundary condition” Proc. 3rd AIMETA International Tribology Conference, Salerno, Italy 18-20 Septemner 2002.

Da Vinci, L. (1495) Codex Atlanticus, (1478-1519) currently stored at Biblioteca Ambrosiana, Milan.

De la Cruz, M., Chong, W.W.F., Teodorescu, M., Theodossiades, S. and Rahnejat, H., (2012) “Transient mixed thermo-elastohydrodynamic lubrication in multi-speed transmissions”, Trib. Int., 49, 2012, pp. 17-29

Dowson, D. and Higginson, G.R. (1959): “A numerical solution to the elastohydrodynamic problem”. Journal of Mechanical Eng. Science, Part 1, Volume 6. pp. 6–15

Elrod, H. G. (1981) “A cavitation algorithm”, Trans. ASME, J. Lubn Tech., 103, 1981, pp. 350–354

Ertel, A.M. and Grubin, A.N. (1949): “Investigation of Scientific and industrial research”. Book 30, Central Scientific Research Institute for Technology and Mechanical Engineering, Moscow.

Erdemir, A. (2002) Review of engineered tribological interfaces for improved boundary lubrication (2002). Tribology International, 38(3), 2005. Pp249-256

Etsion, I (2005) “State of the art in laser surface texturing”. J. Tribology. Trans. ASME 127, 248-253.

Etsion I. and Sher E., (2009) “Improving fuel efficiency with laser surface textured piston rings”. Tribology International 42:542-547.

Evans H.P., Snidle R.W., (1982) “The elastohydrodynamic lubrication of point contact at heavy loads” Proc. R. Soc. Lond. A.

Eyring, H., “Viscosity, plasticity and diffusion as examples of absolute reaction rates”, J. Chem. Phys., 4, 1936, pp. 283-289

Forbes, J. E. and Taylor, E. S. (March 1943) “A method for studying piston friction”, NACA Wartime report.

Furuhama S., Takiguchi M., (1980) “Measurement of piston friction force in actual operating diesel engine”. Society of automotive engineers No. 790855.

Furuhama, S., Asahi, C. and Hiruma, M. (1982) “Measurement of piston ing oil film thickness in an operating engine”. Trans ASLE 26 pp 325 – 332.

Furuhama S., Sasaki S., (1983) “New device for the measurement of piston frictional forces in small engines”. Society of automotive engineers No. 831284.

Furuhama *et al***,** (1984) Some studies on two-ring pistons in Automobile Turbocharged gasoline engine, SAE technical paper 8401183

Gatcombe E.K., (1945) “Lubrication characteristics of involute spur gears-a theoretical investigation” Trans. ASME 67 (1945), pp 177-188.

Gohar and Rahnejat (2008) “Fundamentals of Tribology”, Imperial College Press ISBN 13 978-1-84816-184-9.

Gore, M., Perera, M., Styles, G., King, P.D., Rahnejat, H., (2011) Wear Characteristics of Advanced Honed and Cross-hatched Coated Cylinder Liners. 2011 STLE Annual Meeting and Exhibition, Engine and Drivetrain II, Atlanta Georgia.

Gore, M., Howell-Smith, S., King, P.D. and Rahnejat, H. (2012) “Measurement of in-cylinder friction using the floating liner principle”, *Proc. ASME 2012 Int. Combustion Engine Division Spring Tech. Conf., ICES2012-81028.*

Greenwood J.A and Tripp J.H (1971), The Contact of Two Nominally Flat Rough Surfaces, Proc. Instn Mech Engrs, Vol. 185, 625-633

Grubin, A.N. and Vinogradova, I.E (1949): "Investigation of scientific and industrial Research". Book 30, Central Scientific Research Institute for Technology and Mechanical Engineering, Moscow.

Hertz (1896), Miscellaneous papers by H. Hertz. translated Jones and Schott, Macmillan, London pp146-162

Haddad S., Tjan K.T, (1995) "An analytical study of offset piston and crankshaft designs and the effect of the oil film on piston slap excitation in a diesel", Mech. Mach. Theory, Vol 30, No. 2, pp. 271-284.

Heywood, John B, (1989) "Internal combustion engine fundamentals". McGraw-Hill Higher Education; New edition (1 July 1989), ISBN-10: 0071004998.

Heisler Heinz, (1999). "Vehicle and engine technology", second edition A Butterworth-Heinemann Title; 2 edition (30 Oct 1998), ISBN-10: 0340691867.

Howell-Smith, (2010) Tribological Optimisation of Internal Combustion Engine Piston-Bore conjunction through Surface Modification. PhD, Loughborough University

Honda Motor Company (2002): Owner's Manual, CRF450R, Part number 69MEB510 00X69-MEB-6101

Howautowork.com/list_of_contents/part_1/ch_1/Engine_piston_26.html accessed 25.3.2012

Hu, Y., Cheng, H.S., Arai, T., Kobayashi, Y., and Ayoma, S. Numerical simulation of piston ring in mixed lubrication: a non-axi-symmetrical analysis. Trans. ASME, J. Tribology, 1994, 116, 470-478.

Inventors (2002), http://inventors.about.com/library/inventors/blcar.htm. Accessed 5.6.2012

Jost Report, (1966) Lubrication (tribology) education and research. Department of Education and Science, HMSO.

Khan, H., Sinha, P. and Saxena, A., "A simple algorithm for thermo-elastohydrodynamic lubrication problems", Int. J. Res. & Revs. in Appl. Sci.,1, 2009; pp. 265-279

King (2007), King Review of low-carbon cars Part I: the potential for CO2 reduction October 2007. www.hm-treasury.gov.uk/king accessed 5.6.2012

King (2008), King Review of low carbon cars part II: recommendations for actions March 2008. www.hm-treasury.gov.uk/king accessed 5.6.2012

Kogut L. and Etsion I., "Adhesion in elastic-plastic microcontact", J. Colloid and Inteface Sci., 261, 2003, pp. 372–378

Leary, W. A. and Jovellanos, J. U., (1944) "A study of piston and ring friction" NACA Wartime report, Nov.

Livengood, J. C. and Wallour, C., (1947) "A study of piston-ring friction" NACA Technical Note No. 1249.

Ma, M.-T., Sherrington, I. and Smith, E.H. (1997) 'Analysis of lubrication and friction for a complete piston-ring pack with an improved oil availability model – Part 1:

circumferentially uniform film', Proc. IMechE, Part J: J. Engng. Trib., 211, pp. 1-15

Ma, M. T., Smith, E. H., and Sherrington, I. (1997) Analysis of lubrication and friction for a complete piston-ring pack with an improved oil availability model. Part 2: circumferentially variable film. Proc. Instn Mech. Engrs, Part J: J. Engineering Tribology, 1997, 211, 17–27. DOI: 10.1243/1350650971542282.

McGeehan, J. A., (1978) "A literature review of the effects of piston and ring friction and lubricating oil viscosity on fuel economy", SAE paper No. 780673.

McClure, F., (2007): Numerical modelling of piston secondary motion and skirt lubrication in Internal Combustion Engines, PhD Thesis, Massachusetts Institute of Technology, USA

Meldahl A. (1941) Contribution to the theory of the lubrication of gears and of the stressing of the lubricated flanks of gear teeth. Brown Boveri Rev. 28 11, p. 374.

Michail, S.K., Barber, G.C., (1995) The effects of roughness on piston ring lubrication – part II, The relationship between cylinder wall surface topography and oil film thickness. Tribology Transactions 38(1), 1995. Pp173-177

Mishra, P.C., Rahnejat H., King P.D., (2008) "Tribology of compression ring to cylinder contact reversal". Proceedings of the Institution of Mechanical Engineers, Part J: Journal of Engineering Tribology, 222 (7), pp. 815-826.

Mishra P.C., Rahnejat H. , King P.D., (2009) "Tribology of the ring bore conjunction subject to a mixed regime of lubrication". Proceedings of the Institution of Mechanical Engineers, Part C: Journal of Mechanical Engineering Science, 223(4), pp. 987-998.

Moorey Peter Roger Stuart, “Ancient Mesopotamian Materials and Industries: the archaeological evidence” (1994), p. 146

Morris, N., Rahmani, R., Rahnejat, H., King, P.D. and Fitzsimons, B., “The influence of piston ring geometry and topography on friction”, Proc. IMechE, Part J: J. Engng. Trib., 227(2), 2013, pp. 141-153

Morris, N., Rahmani, R., Rahnejat, H., King, P.D. and Fitzsimons, B., “Tribology of piston compression ring conjunction under transient thermal mixed regime of lubrication”, Trib. Int., 59, 2013, pp. 248-258

Newton, I. Philosophiae Naturalis Principia Mathematica, 1697 (Royal Society, London

O’Rourke B., Radford D., Stanglmaier R., “Tri-Axial Force Measurements on the Cylinder of a Motored SI Engine Operated on Lubricants of Differing Viscosity” Journal of engineering for gas turbines and power ISSN 0742-4795 CODEN JETPEZ (2010)

Peppler W., (1936) Untersuchungen uberdie Druckubertragung bei belasteten und geschmierten umlaufenden achsparallelen Zylindem. In: Maschinenelemente-TatungAachen Vol. 42, VDI, Berlin (1935), p. 1936.

Peppler W., (1938) Druckubertragung angeschmierten zylindrischen Gleitund Walzfachen. In: , VDI.-Forschungsheft, p. 391.

Perera M.S.M., Theodossiades, S., Rahnejat, H., (2007) “A multi-physics multi-scale approach in engine design analysis”, Proceedings of the Institution of Mechanical Engineers, Part K: Journal of Multi-body Dynamics, 221(3), pp. 335-348.

Perera, M.S.M., Theodossiades, S. and Rahnejat, H., “Elasto-multi-body dynamics of internal combustion engines with tribological conjunctions”, Proc. IMechE, Part K: J. Multi-body Dyn., 224(3), 2010, pp. 261-277

Petrusevich A.I (1951) “Fundamental conclusions from the contacthydrodynamic theory of lubrication”. Izo. Akad. Nauk SSSR OTN 2, p. 209.

Rahmani, R., Theodossiades, S., Rahnejat, H. and Fitzsimons, B. (2012) “Transient elastohydrodynamic lubrication of rough new or worn piston compression ring conjunction with an out-of-round cylinder bore”, Proc. IMechE, J. Eng. Trib., DOI: 10.1177/1350650111431028.

Rahnejat, H. (1984): “Influence of Vibration on Oil Film in Concentrated Contacts”. PhD.Thesis, Imperial College of Science and Technology, University of London.

Rahnejat H., Gohar R., (1985) “The vibrations of radial ball bearings” Proceedings of the Institution of Mechanical Engineers, Part C: Mechanical Engineering Science 1983-1988 (vols 197-202), 199 (C3), pp. 181-193.

Rahnejat, H., Multi-body Dynamics: Vehicles, Machines and Mechanisms, Professional Engineering Publishing, Bury St Edmunds, (1998)

Rahnejat, H., Teodorescu, M., Balakrishnan, S. (2006) “Physics of ultra-thin surface films on molecularly smooth surfaces” Proceedings of the Institution of Mechanical Engineers, Part N: Journal of Nanoengineering and Nanosystems, 220 (1), pp. 7-19.

Reynolds, O. (1886): “On the theory of lubrication and its application to Mr. Beauchamp Tower's experiments, including and experimental determination of the viscosity of olive oil”. Phil. Transaction of Royal Society, London, Volume 177, pp. 157-234.

Richardson, D.E., “Review of Power Cylinder Friction for Diesel Engines”, Trans. ASME, J. Engng. for Gas Turbines & Power, 122, 2000, pp.506-519

Ruddy, B. L., Dowson, D. and Economou, P. N. (1981), “A theoretical analysis of the twin-land type of oil-control piston ring”. J. Mech. Engng Sci., 23, 51-62.

SAE J1349 (2005) "Certified Power - SAE J1349 Certified Power SAE International". Sae.org. Retrieved 2011-07-18.

Sasaki T., Mori H., Okino, N. (1962) “Fluid lubrication theory of roller bearings” Trans. ASME. J. Basic Engineering.

Sawicki, J.T. and Yu, B., “Analytical solution of piston ring lubrication using mass conserving cavitation algorithm”, Trib. Trans., 43(4), 2000, pp587-594.

Spencer, A., Almqvist, A., Larrson, R., (2011) A semi-deterministic texture/roughness model of the piston ring/cylinder liner contact. Proc. ImechE Part J; Journal of engineering tribology, 225, pp325-333.

Sommerfeld, A. (1904). “Simplified Deduction of the Field and the Forces of An Electron Moving in Any Given Way”. Akad. van Wetensch. te Amsterdam 13. (English translation 7, 346 (1905)).

Stribeck, R. (1901) “Kugellager fur beliebige belastungen”. Z. Ver. Deutsche Ing., Volume 45, pp. 73-125.

Styles, G. et al, 2014. “In-cycle and life-time friction transience in piston ring–liner conjunction under mixed regime of lubrication”. International Journal of Engine Research, [published online before print February 4, 2014, DOI:10.1177/1468087413519783], 15pp

Teodorescu, M., Balakrishnan, S. and Rahnejat, H., “Integrated tribological analysis within a multi-physics approach to system dynamics”, Tribology & Interface Engineering Series (Elsevier), 48, 2005, pp. 725-737

Teodorescu M and Taraza D. “Combined multi-body dynamics and experimental investigation for determination of the cam-flat tappet contact condition.” Proceedings of the Institution of Mechanical Engineers, Part K: Journal of Multi-body Dynamics, September 1, 2004; vol. 218, 3: pp. 133-142

Tian, T., “Dynamic Behaviour of Piston Rings and their Practical Impact Part 2: Oil Transport, Friction and Wear of Ring/Liner Interface and the Effects of Piston and Ring Dynamics”, Proc. Instn. Mech. Engrs., Part J: . Engng. Trib., 216, pp 229-247, 2002.

The Eddington Transport Study (2006), Department for transport www.dft.gov.uk.

The European Federation for Transport and Environment, (2006) http://www.transportenvironment.org/sites/default/files//docs/Publications/2007/2007-09_progress_voluntary_commitment_2006.pdf

Truhan, J.J., Qu, J., Blau, P. J.,(2005) “A rig test to measure friction and wear of heavy duty diesel engine piston rings and cylinder liners using realistic lubricants” Tribology International 38 (2005) 211-218, 2005.

Uras. H.Mehmet and Donald J. Patterson, (1983) “Measurement of piston ring assembly friction instantaneous IMEP method” University of Michigan Society of automotive engineers 0148-7191/83/0228-0416.

Usher, Abbott, Payson, “A History of Mechanical Inventions”, Harvard University Press, 1970. p135

Weiss Alex (2008). “Bearings”. Special Interest Model Books ISBN-10: 1854862502

Wikander, Örjan (2000). "The Water-Mill". Handbook of Ancient Water Technology. Technology and Change in History 2. Leiden: Brill. pp. 371–400 (396f.). ISBN 90-04-11123-9.

Winterbone, D.E. And Tennant, D.W.H., (1981) “The variation of friction and combustion rates during diesel engine transients”, SAE paper No. 810339

Yoshida H., Kusama K,. Sagawa J., (1990) “Effects of surface treatments on piston ring friction force and wear”. SAE paper No. 90058.

Yang P., Cui, J., Jin, Z.M. and Dowson, D. “Transient elastohydrodynamic analysis of elliptical contacts. Part 2: thermal and Newtonian lubricant solution”, Proc. IMechE, Part J: J. Engng. Trib.; 219, 2005, pp. 187-200